Title

Extracellular Vesicle Secretion is Coupled to Plasma Membrane Repair

ISBN

9798288861697

Author

Williams, Justin

Publication Date

2025-05-15

Peer reviewed|Thesis/dissertation

Extracellular Vesicle Secretion is Coupled to Plasma Membrane Repair

By

Justin Williams

A dissertation submitted in partial satisfaction of the

requirements for the degree of

Doctor of Philosophy

in

Molecular and Cell Biology

in the

Graduate Division

of the

University of California, Berkeley

Committee in charge:

Professor Randy Schekman, Chair
Professor Kathleen Collins
Professor Roberto Zoncu
Professor Alanna Schepartz

Spring 2025

Abstract

Extracellular Vesicle Secretion is Coupled to Plasma Membrane Repair

by

Justin Williams

Doctor of Philosophy in Molecular and Cell Biology

University of California, Berkeley

Professor Randy Schekman, Chair

Extracellular Vesicles (EVs) are membrane enclosed particles secreted by all domains of life. In humans, extracellular vesicles are implicated in cell-to-cell signaling and may have utility as delivery vectors or biomarkers for early disease detection. Whether EVs are always constitutively secreted or if physiological stimuli exist that promote secretion is not known. Here, we show that EV secretion is stimulated by plasma membrane damage. Damaging the plasma membrane using pore forming toxins, shear stress, or laser ablation robustly promotes secretion of both plasma membrane-derived vesicles, microvesicles, and endosome-derived vesicles, exosomes. Our data indicates that Ca^{2+}-dependent membrane binding proteins, called annexins, are required for these processes. Annexin A6 is required for exosome secretion, while other annexins promote microvesicle secretion after cleavage by Ca^{2+}-dependent proteases, called calpains. Our data also provides evidence for new models of plasma membrane repair. For example, we find that a Ca^{2+} channel on the inner membrane mitochondrial prevents cytosolic Ca^{2+} overload during membrane repair. We anticipate that cells experiencing plasma membrane damage, including muscle and metastatic cancer cells, secrete EVs at elevated levels.

Table of Contents

Acknowledgements

Thank you to my parents, Nidhi and Loren, for always believing in me.

Thank you to Cabo, for showing me what is important in life.

Thank you to the Schekman lab for teaching me how to be a biologist. Especially to Jordan Ngo and Jasleen Singh who worked with me on many projects and Morayma Temoche-Diaz and Criss Hartzell who taught me so many techniques. I am lucky to have worked with so many fun, kind colleagues and friends.

Thank you to my committee, especially Kathy Collins and Roberto Zoncu, for all your helpful suggestions.

Thank you, Randy Schekman, for teaching me to be a skeptical scientist. I now read every CNS paper with the intent to dismantle it.

Thank you to all the friends and my graduate cohort who got me through the ups and downs of graduate school. Especially, Joyner Cruz, thank you for teaching me about morality, sentience, and aliens. Nick Fahrenkrog, thank you for showing me how to have a balanced life.

Shaina Carroll, thank you for keeping me grounded and loved.

Introduction

Attribution Statement: Portions of the introduction and conclusion are adapted from previously published work: Ngo and Williams et al. *Annu. Rev. Biochem.* 2025. Jordan Matthew Ngo contributed equally to this publication. The author of this document wrote portions of the initial draft, helped edit and organize the manuscript, and helped write the initial draft of the response to reviewers.

Extracellular Vesicles (EVs) are secreted, membrane-enclosed compartments produced by cells from all three major branches of life. EVs are divided into two subtypes: Microvesicles that bud directly off the cell surface, and exosomes that form in the intracellularly. EVs have utility as biomarkers, as they contain protein and RNA specific to their origin cell. EVs may also play in cell-to-cell communication; reportedly, EVs stimulate membrane receptors on the cell surface or deliver intracellular cargo (miRNA, mRNA, protein, etc.) by fusing with the limiting membrane of a target cell. In this model, EVs are loaded with cargo that alters behavior of other cells. However, many other models of EV function exist. EVs may be produced as a quality control mechanism to clear unwanted material and maintain cellular homeostasis. The mechanisms and physiological circumstances driving EV secretion are poorly understood.

The plasma membrane is the outer barrier of the cell. Plasma membrane integrity is required for homeostasis, and failure to repair plasma membrane disruptions leads to cell death and disease in humans. The membrane repair process is initiated by influx of extracellular calcium. Calcium influx triggers membrane rearrangements at the lesions site and exocytosis of an internal organelle called the lysosome. Annexins are a class of proteins that have roles in plasma membrane repair. In the presence of micromolar calcium, annexins bind to membranes and may plug lesion sites by tethering membranes. Knockdowns of several individual annexins cause defects in membrane resealing in cultured cells. Muscle cells experience high rates of membrane damage in vivo due to repeated contractions and are dependent on the membrane repair machinery for survival. For example, 20% of muscle fibers in rat triceps are disrupted after eccentric exercise. Consistent with annexins playing a role in muscle repair, annexin mutations cause muscular dystrophy in mice. Exactly how membrane lesions are resolved by annexins is not understood.

Chapter 1: Annexin A6 mediates calcium-dependent exosome secretion during plasma membrane repair

Attribution Statement: Portions of this chapter are adapted from previously published work: Williams and Ngo et al. *eLife* 2023. Jordan Matthew Ngo contributed equally to this publication. The author of this document performed experiments, wrote portions of the initial draft, helped edit and organize the manuscript, and helped write the initial draft of the response to reviewers.

Introduction: Exosomes are formed by inward budding of the endosomal limiting membrane, producing multivesicular bodies (MVBs) that contain intraluminal vesicles (ILVs). When the MVB fuses with the plasma membrane, ILVs are released outside the cell as exosomes. Cellular calcium influx, mediated by ionophores, stimulated exosome secretion. Exosome secretion in both ionophore-stimulated and unstimulated cells depends on Rab27 proteins.

During membrane repair, lysosomes fuse with the plasma membrane in a Ca^{2+}-dependent manner. This process may resolve plasma membrane lesions by relieving membrane tension. The lysosome and MVB have similar protein and lipid composition, including the same Rab GTPases marking their exterior. Given the similarities between lysosomes and MVBs and that calcium influx stimulates exosome secretion, we hypothesized that MVBs may also fuse with the plasma membrane upon plasma membrane damage. These results raise the possibility that exosomes may be secreted as a byproduct of the Ca^{2+}-dependent plasma membrane repair process that occurs after membrane disruption. Highlighting a possible connection between PM repair and exosome secretion, loss of Rab27a or Rab27b impairs membrane repair in cultured cells. In mice, loss of the key muscle membrane repair protein, dysferlin, results in limb girdle muscular dystrophy 2B. Remarkably, Rab27a is significantly upregulated in the muscle cells of dysferlin-deficient mice. Upregulated Rab27a-mediated exocytosis is thought to partially compensate for loss of dysferlin.

To determine if exosomes are secreted during Ca^{2+}-dependent plasma membrane repair, we developed an improved nanoluciferase (Nluc) reporter system to quantify exosome secretion that is sensitive, linear, and amenable to high throughput. Using this assay, we established that a Ca^{2+} ionophore, a pore-forming cytolysin, and physiological mechanical stress all stimulated exosome secretion in an extracellular Ca^{2+}-dependent manner. We showed that annexin A6 (ANXA6), a plasma membrane repair protein, is recruited to MVBs in the presence of Ca^{2+} and demonstrated that ANXA6 is required for Ca^{2+}-dependent exosome secretion. We then observed that depletion of ANXA6 stalls MVBs at the periphery of cells treated with a Ca^{2+} ionophore. Next, we developed a streptolysin O (SLO)-permeabilized cell reaction that recapitulates Ca^{2+}- and ANXA6-dependent exosome

secretion. Finally, we demonstrated that the two annexin domains of ANXA6 become enriched at different membranes upon elevation of cytosolic Ca^{2+}. Our results demonstrate that exosome secretion is coupled to Ca^{2+}-dependent plasma membrane repair and that ANXA6 may serve as a potential tether for the recruitment of MVBs to the plasma membrane.

Materials and Methods

Cell lines, media, and general chemicals

HCT116, HCT116 CD63-Nluc, HEK293T, HEK293T FLAG-Nluc-CD63, and U-2 OS cells were cultured at 37°C in 5% CO_2 and maintained in Dulbecco's Modified Eagle's Medium (DMEM) supplemented with 10% fetal bovine serum (FBS) (Thermo Fisher Scientific, Waltham, MA, USA). Cells were routinely tested (negative) for mycoplasma contamination using the MycoAlert Mycoplasma Detection Kit (Lonza Biosciences). HCT116, HEK293T, and U-2 OS cells were authenticated using STR profiling at the UC Berkeley Cell Culture Facility. For the experiments detailed in Figure 2B and C and Figure 2—figure supplement 1B, we cultured HCT116 CD63-Nluc and HEK293T FLAG-Nluc-CD63 cells in Ca^{2+}-free DMEM (Thermo Fisher Scientific). For Figure 2F, HCT116 CD63-Nluc cells were incubated in EV-depleted medium. EV-depleted medium was produced by ultracentrifugation at 186,000 × *g* (40,000 RPM) for 24 hr using a Type 45Ti rotor. Ionomycin was purchased from Cayman Chemicals. Unless otherwise noted, all other chemicals were purchased from Sigma-Aldrich (St. Louis, MO, USA).

Lentivirus production and transduction

HEK293T cells at 40% confluence within a 6-well plate were transfected with 165 ng of pMD2.G, 1.35 µg of psPAX2, and 1.5 µg of a pLKO.1-Hygro, lentiCRISPR v2-Blast, or pLJM1 plasmid using the TransIT-LT1 Transfection Reagent (Mirus Bio) as per the manufacturer's protocol. At 48 hr post-transfection, 1 ml of fresh DMEM supplemented with 10% FBS was added to each well. The lentivirus-containing medium was harvested 72 hr post-transfection by filtration through a 0.45 µm polyethersulfone (PES) filter (VWR Sciences). The filtered lentivirus was distributed in aliquots, snap-frozen in liquid nitrogen, and stored at –80°C. For lentiviral transductions, we infected HCT116 CD63-Nluc cells with filtered lentivirus in the presence of 8 µg/ml polybrene for 24 hr, and the medium was replaced. HCT116 CD63-Nluc cells were selected using 200 µg/ml hygromycin B or 4 µg/ml blasticidin S for 8 days and 6 days, respectively. The efficiency of each gene knockdown was assessed by immunoblot analysis.

Immunoblotting

Cells were lysed in PBS containing 1% TX-100 and a protease inhibitor cocktail (1 mM 4-aminobenzamidine dihydrochloride, 1 µg/ml antipain dihydrochloride, 1 µg/ml aprotinin, 1 µg/ml leupeptin, 1 µg/ml chymostatin, 1 mM phenylmethylsulfonyl fluoride, 50 µM N-tosyl-L-phenylalanine chloromethyl ketone, and 1 µg/ml pepstatin) and incubated on ice for 15 min. The whole cell lysate was centrifuged at 15,000 × *g* for 10 min at 4°C and the post-nuclear supernatant was diluted with 6× Laemmli buffer (without DTT) to a 1× final concentration. Samples were heated at 95°C for 5 min and proteins resolved on 4–20% acrylamide Tris-glycine gradient gels (Life Technologies). Proteins were then transferred to polyvinylidene difluoride membranes (EMD Millipore, Darmstadt, Germany), blocked with 5% dry milk in TBS, washed 3× with TBS-T and incubated overnight with primary antibodies in 5% bovine serum albumin in TBS-T. The membranes were then washed again 3× with TBS-T, incubated for 1 hr at room temperature with 1:10,000 dilutions of anti-rabbit or anti-mouse secondary antibodies (GE Healthcare Life Sciences, Pittsburgh, PA, USA), washed 3× with TBS-T, washed once with TBS and then detected with ECL-2 or PicoPLUS reagents (Thermo Fisher Scientific) for proteins from cell lysates or EV isolations, respectively.

Immunofluorescence microscopy

For immunofluorescence, we grew cells on Poly-D-Lysine (PDL)-coated coverslips which were then washed once with PBS, fixed in 4% EM-grade paraformaldehyde (PFA; Electron Microscopy Science Hatfield, PA, USA) for 15 min at room temperature, washed 3× with PBS and permeabilized/blocked in blocking buffer (2% BSA and 0.02% saponin in PBS) for 30 min at room temperature. Cells were then incubated with a 1:250 dilution of primary antibody and/or phalloidin stain overnight at 4°C, washed 3× with PBS, incubated with a 1:1000 dilution of fluorophore-conjugated secondary antibody for 1 hr at room temperature and washed 3× with PBS. Coverslips were then mounted overnight in ProLong-Gold antifade mountant with DAPI (Thermo Fisher Scientific) and sealed with clear nail polish before imaging. For microtubule visualization, cells were fixed using ice cold methanol and processed as above.

For Figure 6, we transfected U-2 OS cells grown on PDL-coated coverslips with the indicated plasmids using Lipofectamine 2000 as per the manufacturer's protocol. The medium containing the transfection mixture was removed ~5 hr post-transfection and replaced with DMEM supplemented with 10% FBS. Cells were treated 16 hr post-transfection with DMSO or 1 µM ionomycin with or without 5 µg/ml CF640R WGA conjugate (Biotium) as indicated for 10 min at 37°C. Treated cells were then washed with PBS, fixed in 4% EM-grade PFA for 15 min at room temperature, and processed as above. The concentrations utilized for each plasmid transfection were as follows: pN1-ANXA6(FL)-

mNeonGreen (200 ng/ml), pN1-ANXA6(N)-mNeonGreen (200 ng/ml), and pN1-ANXA6(C)-mScarlet (200 ng/ml).

The images in Figure 2—figure supplement 1 and Figure 4 were acquired on an Echo Revolve Microscope using the 60× Apo Oil Phase, NA 1.42 objective. The images in Figure 6 were acquired using an LSM900 confocal microscope system (ZEISS) using Airyscan 2 superresolution mode and a 63× Plan-Apochromat, NA 1.40 objective.

EV isolation and fractionation by iodixanol buoyant density gradient equilibration

Fresh aliquots of 5, 7.5, 10, 12.5, 15, 17.5, 20, 22.5, and 25% (v/v) iodixanol solutions were prepared by mixing appropriate volumes of Solution B (0.25 M sucrose, 2 mM $MgCl_2$, 1 mM EDTA, 20 mM Tris-HCl, and pH 7.4) and Solution D (41.7 mM sucrose, 2 mM $MgCl_2$, 1 mM EDTA, 20 mM Tris-HCl, pH 7.4, and 50% (w/v) iodixanol). Iodixanol gradients were prepared by sequential 500 µl overlays of each iodixanol solution in a 5 ml SW55 tube, starting with the 25% iodixanol solution and finishing with the 5% iodixanol solution. After the addition of each iodixanol solution, the SW55 tube was flash frozen in liquid nitrogen. Complete iodixanol gradients were stored at –20°C and thawed at room temperature for 45 min prior to use.

For the iodixanol gradients detailed in Figure 2F, conditioned medium (240 ml) was harvested from vehicle- or ionomycin-treated HCT116 CD63-Nluc cells. All subsequent manipulations were completed at 4°C. Cells and large debris were removed by low-speed sedimentation at 1,000 × *g* for 15 min in a Sorvall R6 +centrifuge (Thermo Fisher Scientific) followed by medium-speed sedimentation at 10,000 × *g* for 15 min using a fixed angle FIBERlite F14–6×500 y rotor (Thermo Fisher Scientific). The supernatant fraction was then centrifuged at 29,500 RPM for 1.25 hr in a SW32 rotor. The high-speed pellet fractions were resuspended in PBS, pooled, loaded at the top of a prepared iodixanol gradient, and centrifuged in a SW55 rotor at 36,500 RPM for 16 hr with minimum acceleration and no brake. Fractions (200 µl) were collected from top to bottom. An aliquot of each fraction was saved for luminescence analysis, and the rest was diluted in 6× Laemmli buffer (without DTT) for immunoblot analysis. Density measurements were taken using a refractometer.

For the iodixanol gradients detailed in Figure 2G, we harvested conditioned medium from vehicle- or ionomycin-treated HCT116 CD63-Nluc cells grown in a 12-well plate. All subsequent manipulations were completed at 4°C. Cells and large debris were removed by low-speed sedimentation at 1000 × *g* for 15 min followed by medium-speed sedimentation at 10,000 × *g* for 15 min in an Eppendorf 5430 R centrifuge (Eppendorf, Hamburg, Germany). Aliquots (200 µl) of conditioned medium from the supernatant of the medium-speed centrifugation were loaded at the top of a prepared iodixanol gradient and

centrifuged in a SW55 rotor at 36,500 RPM for 16 hr with minimum acceleration and no brake. Fractions (200 µl) were collected from top to bottom and analyzed for luminescence. Density measurements were taken using a refractometer.

Immunoisolation of MVBs and Ca^{2+}-dependent binding proteins

HCT116 CD63-Nluc cells were grown to ~90% confluence in 7×150 mm dishes. Cells were scraped into 5 ml of cold PBS per plate and centrifuged at 200 × *g* for 5 min at 4°C. The cold PBS was aspirated, and the cell pellet was resuspended in two volumes of cold lysis buffer (136 mM KCl, 10 mM KH_2PO_4 pH 7.4, 1 mM DTT, protease inhibitor cocktail [see Immunoblotting section], and 6% Optiprep [w/v]). The cell slurry was passed 14 times through a 25-gauge syringe in a cold room, and the post-nuclear supernatant was prepared by centrifugation of lysed cells at 1000 × *g* for 10 min at 4°C. The post-nuclear supernatant was diluted 1:2 with lysis buffer.

Beads from 300 µl of magnetic Protein G Dynabeads (Thermo Fisher Scientific) slurry were sedimented with a magnetic tube rack and resuspended in lysis buffer. The bead slurry was split evenly into three tubes and then re-centrifuged. The diluted post-nuclear supernatant was divided between the three tubes. Tube #1 also received 1 mM $CaCl_2$ (Beads only control), tube #2 also received 1 mM $CaCl_2$ and 5 µg anti-Nluc antibody (Ca^{2+}-treated), and tube #3 also received 1 mM EGTA and 5 µg anti-Nluc antibody (EGTA treated). The reaction was incubated for 15 min at room temperature. Beads were washed three times with lysis buffer. A beads only control and Ca^{2+}-treated samples both had 2 mM $CaCl_2$ added to the wash buffer. The EGTA-treated sample was washed with lysis buffer containing 2 mM EGTA. The beads only control and Ca^{2+}-treated samples were eluted with 50 µl lysis buffer containing 2 mM EGTA, and the EGTA-treated sample was eluted with lysis buffer containing 2 mM $CaCl_2$. All three samples were eluted again with 50 µl lysis buffer containing 0.2% TX-100.

CD63-Nluc exosome secretion assay

HCT116 CD63-Nluc cells were grown to ~80% confluence in 24-well plates. All subsequent manipulations were performed at 4°C. Conditioned medium (200 µl) was taken from the appropriate wells, added to a microcentrifuge tube, and centrifuged at 1000 × *g* for 15 min in an Eppendorf 5430 R centrifuge (Eppendorf, Hamburg, Germany) to remove intact cells. Supernatant fractions (150 µl) from the low-speed sedimentation were moved to a new microcentrifuge tube and centrifuged at 10,000 × *g* for 15 min to remove cellular debris. Supernatant fractions (50 µl) from this medium-speed centrifugation were then utilized to measure CD63-Nluc exosome luminescence. During these centrifugation steps, the cells

were placed on ice, washed once with cold PBS, and lysed in 200 µl of PBS containing 1% TX-100 and protease inhibitor cocktail.

To measure CD63-Nluc exosome secretion, we prepared a master mix containing the membrane-permeable Nluc substrate and a membrane-impermeable Nluc inhibitor using a 1:1000 dilution of Extracellular NanoLuc Inhibitor and a 1:333 dilution of NanoBRET Nano-Glo Substrate into PBS (Promega, Madison, WI, USA). Aliquots of the Nluc substrate/inhibitor master mix (100 µl) were added to 50 µl of the supernatant fraction from the medium-speed centrifugation and vortexed briefly, and luminescence was measured using a Promega GlowMax 20/20 Luminometer (Promega, Madison, WI, USA). An aliquot (1.5 µl) of 10% TX-100 was then added to each reaction tube for a final concentration of 0.1% TX-100, and the sample was briefly vortexed before luminescence was measured again. For the intracellular normalization measurement, the luminescence of 50 µl of cell lysate was measured using the Nano-Glo Luciferase Assay kit (Promega, Madison, WI, USA) as per the manufacturer's protocol. The exosome production index (EPI) for each sample is calculated as follows: EPI = ([medium] – [medium + 0.1% TX-100])/cell lysate.

For the CD63-Nluc exosome secretion assays in Figure 2C and D and Figure 2—figure supplement 1B, cytosol was not depleted as in the biochemical reconstitution assays detailed in Figure 5.

SLO time courses

HCT116 CD63-Nluc cells were grown to ~80% confluence in 24-well PDL-coated plates. Cells were washed with 200 µl of cold PBS and incubated with 200 µl of cold (4°C) 250 ng/ml SLO in Ca^{2+}-free DMEM with 1 mM EGTA. The cold, SLO-containing medium was aspirated, and 200 µl of pre-warmed (37°C) Ca^{2+}-free DMEM with 1.8 mM $CaCl_2$ was added. Cells were incubated at 37°C for the indicated times after which exosome secretion was measured as described in paragraph 2 of 'CD63-Nluc exosome secretion assay'.

Mechanical stress experiments

Two 15 cm plates of HCT116 CD63-Nluc cells were harvested with 10 ml of Accutase and diluted with 40 ml of Ca^{2+}-free DMEM. A cell slurry (16 ml) was added to three tubes and centrifuged at 300 × *g* for 5 min at room temperature. Cells were gently resuspended in either 0.5 ml Ca^{2+}-free DMEM or Ca^{2+}-free DMEM +2 mM Ca^{2+} (final). Cells were pumped through a 30-gauge needle at a flow rate of 3.5 µl/s ($\tau=4Q\eta/\pi R^3$ = ~89 dyn/cm^2, where Q=0.0035 cm^3/s, η=0.01 dyn*s/cm^2, 30 G average internal radius = 7.94×10^{-3} cm) or twice the flow rate of 7 µl/s ($\tau=4Q\eta/\pi R^3$=178 dyn/cm^2, where Q=0.0035 cm^3/s, η=0.01 dyn*s/cm^2, 30 G average internal radius = 7.94×10^{-3} cm) using a Harvard Apparatus syringe pump (Catalog No. 98–4730). Cells were incubated for 5 min at 37°C before being placed back on

ice. The cell suspension was centrifuged at 300 × *g* for 5 min, and the supernatant fraction was then filtered through a 0.45 µm PES filter. Exosome secretion was measured as described in paragraph 2 of 'CD63-Nluc exosome secretion assay,' in this assay without a cell lysate measurement.

Isolation of cytosol from cultured human cells

HCT116 WT cells were grown to ~90% confluence in 20×150 mm dishes. All subsequent manipulations were performed at 4°C. Each 150 mm dish was washed once with 10 ml of cold PBS and then harvested by scraping into 5 ml of cold PBS. The 5 ml cell suspension was then used to harvest cells from four additional 150 mm dishes, and this process was repeated until all the cells were harvested. Cells were then collected by centrifugation at 200 × *g* for 5 min, and the supernatant fraction was discarded. The cell pellet was resuspended in 3 ml of cold hypotonic lysis buffer (20 mM HEPES, pH 7.4, 10 mM KCl, 1 mM EGTA, 1 mM DTT, and protease inhibitor cocktail) and placed on ice. After 15 min, the cell suspension was transferred to a pre-chilled 7 ml Dounce homogenizer, and the cells were mechanically lysed by ~80 strokes with a tight-fitting Dounce pestle. The lysed cells were centrifuged at 1000 × *g* for 15 min to sediment intact cells and nuclei, and the post-nuclear supernatant was then centrifuged at 32,500 RPM (~128,000 × *g*) for 30 min in an Optima XE-90 ultracentrifuge (Beckman Coulter). The supernatant (cytosol fraction) was collected conservatively without disturbing the pellet and then concentrated using a 4 ml Amicon–3 k concentrator to a final protein concentration of ~40 mg/ml. The cytosol was distributed in aliquots, snap-frozen in liquid nitrogen, and stored at –80°C until use. The rat liver cytosol was prepared as described in Tang et al., 2020.

Reconstitution of CD63-Nluc exosome secretion in permeabilized cells

SLO was pre-activated in PBS containing 10 mM DTT at 37°C for 2 hr, distributed in aliquots into low-retention microcentrifuge tubes, snap-frozen in liquid nitrogen, and stored at –80°C until use. The protein concentration of each SLO batch was determined by a Bradford assay.

HCT116 CD63-Nluc cells were grown to ~80% confluence in 24-well PDL-coated plates. The PDL plate was placed on ice, and the cells were washed once with PBS containing 1 mM EGTA. The PBS wash was aspirated, replaced with 200 µl of cold transport buffer (20 mM HEPES, pH 7.4, 250 mM D-sorbitol, 120 mM KCl, 10 mM NaCl, 2 mM $MgCl_2$, 1.2 mM KH_2PO_4, 1 mM EGTA, and protease inhibitor cocktail), supplemented with 0.6 µg/ml of pre-activated SLO, and incubated at 4°C for 15 min. Unbound SLO was aspirated, and the cells were washed once with cold transport buffer. Cells were then permeabilized by the addition of pre-warmed transport buffer containing 2 mM DTT followed by a 10 min

incubation at 37°C. Permeabilized CD63-Nluc cells were then washed at 4°C in transport buffer, high-salt transport buffer (containing 1 M KOAc) and finally transport buffer (10 min each wash) to deplete cytosol.

Complete permeabilized cell exosome secretion assays (200 µl) consisted of permeabilized CD63-Nluc cells, cytosol (4 mg/ml final concentration), 20 µl 10× ATP^r (10 mM ATP, 400 mM creatine phosphate, 2 mg/ml creatine phosphokinase, 20 mM HEPES, pH 7.2, 250 mM D-sorbitol, 150 mM KOAc, and 5 mM MgOAc), 3 µl of 10 mM GTP, 4 µl of 100 mM $CaCl_2$ (2 mM final concentration), and cold transport buffer. The concentration of blocking IgG antibodies utilized in Figure 5E was 25 µg/ml. The assembled reaction mixes were added to the permeabilized CD63-Nluc cells for 5 min on ice prior to placing the entire 24-well PDL coated plate in a 30°C water bath for 2 min to stimulate exosome secretion. Permeabilized cells were then placed back on ice, and 100 µl of each reaction supernatant was loaded into a 0.4 µm AcroPrep filter plate (Pall Corporation) and centrifuged at 1500 × *g* for 1 min in an Eppendorf 5810 R centrifuge (Eppendorf, Hamburg, Germany) to collect CD63-Nluc exosomes. During this centrifugation step, 100 µl of cold transport buffer containing 2% TX-100 and protease inhibitor cocktail was added to each well of the 24-well PDL coated plate to lyse the cells and bring the volume up to 200 µl. Filtrate aliquots (50 µl) and 50 µl of the cell lysate were used to measure exosome secretion and normalized to the number of cells per reaction, respectively, using the cell-based CD63-Nluc exosome secretion assay protocol detailed above.

For the permeabilized cell exosome secretion assay detailed in Figure 5D, the nucleotide-depleted rat liver cytosol was generated by using a HiTrap Sephadex G-25 Desalting Column (Cytiva Life Sciences) as per the manufacturer's protocol.

Results

Design and validation of an endogenous CD63-Nluc exosome secretion assay

We sought to develop a cell-based exosome secretion assay that is quantitative, sensitive, amenable to high-throughput, and able to distinguish cell debris and *bona fide* exosomes. A previous study developed a luminescence-based assay to quantify exosome secretion by inserting Nluc into the endogenous locus of the tetraspanin protein CD63 (Hikita et al., 2018). We obtained the HCT116 CD63Nluc-KI #17 cell line (referred to herein as CD63-Nluc cells) from this group and built upon their assay.

Sequestration of CD63 during ILV biogenesis results in the amino- and carboxyl-termini oriented to the exosome lumen. We leveraged this topology along with the relative membrane permeabilities of the substrate and an inhibitor of Nluc to develop a quantitative cellular assay to monitor the secretion of exosomes (Figure 1A). Furimazine,

the substrate of Nluc, permeates through cellular membranes and enables luminescence from both cellular debris and intact CD63-Nluc exosomes present within the conditioned medium of cultured CD63-Nluc cells. The addition of a membrane-impermeable Nluc inhibitor eliminates luminescence derived from cellular debris where Nluc is readily accessible, while not affecting the luminescence derived from intact CD63-Nluc exosomes incubated with furimazine (Walker et al., 2017). Finally, solubilization of cellular membranes by the addition of the non-ionic detergent Triton X-100 (TX-100) exposes all CD63-Nluc to the inhibitor. The addition of the membrane-impermeable Nluc inhibitor depleted a significant portion of luminescence derived from the conditioned medium of CD63-Nluc cells (~30%) and membrane solubilization by TX-100 reduced luminescence to background levels (Figure 1B).

To further validate the localization of the CD63-Nluc luminescence signal to sedimentable vesicles, we subjected the conditioned medium fraction to differential centrifugation and found that CD63-Nluc luminescence was removed after high-speed sedimentation or upon the addition of TX-100 (Figure 1C). Next, we obtained a partially clarified conditioned medium fraction by differential centrifugation and fractionated the material on a linear iodixanol gradient (Figure 1D). CD63-Nluc vesicles equilibrated at a density of 1.11 g/ml, a buoyancy similar to published reports (Jeppesen et al., 2019). In a time course over 24 hr, we measured secreted CD63-Nluc luminescence in the presence of Nluc inhibitor alone or with TX-100 and found the signal increased linearly, consistent with exosome secretion over time (Figure 1E). The luminescence signal in the presence of the Nluc inhibitor and TX-100 remained constant, consistent with cell rupture/detachment during medium change. Thus, our modified CD63-Nluc assay faithfully reported the secretion of *bona fide* CD63-positive exosomes, and we have used this method to assess the molecular requirements for exosome secretion.

Elevation of cytosolic Ca^{2+} during plasma membrane damage stimulates exosome secretion

We investigated the relationship between elevation of cytosolic Ca^{2+} levels and exosome secretion. In agreement with previous reports (Messenger et al., 2018), influx of Ca^{2+} into the cytoplasm using the Ca^{2+} ionophore ionomycin (5 μM, 30 min) induced robust exosome secretion compared to the level of secretion of the vehicle control (Figure 2A). Exosome secretion initiated within 2 min of ionomycin treatment and was complete by 10 min (Figure 2B).

An influx of extracellular Ca^{2+} triggers lysosome exocytosis as a means to repair plasma membrane damage (Andrews and Corrotte, 2018; Corrotte et al., 2015; Corrotte and Castro-Gomes, 2019; Demonbreun and McNally, 2016). A similar process is elicited in

cells treated with a Ca^{2+} ionophore (Jaiswal et al., 2002). We reasoned that MVBs, like lysosomes, might fuse with the plasma membrane to facilitate membrane repair. Upon treatment with the pore-forming toxin, SLO, exosomes were secreted in a Ca^{2+}-dependent manner (Figure 2C). Treatment with 400 ng/ml or 800 ng/ml of SLO significantly increased exosome production, dependent on the presence of extracellular $CaCl_2$ (1.8 mM). Similar to ionomycin, SLO induced exosome secretion 2 min after initial application and was complete after 10–20 min (Figure 2D). In SLO time course experiments, pore formation was synchronized by pre-incubating cells with SLO on ice (Corrotte et al., 2015). We noted that SLO permeabilized exosomes as well as cells. SLO treatment of conditioned medium decreased the CD63-Nluc signal when the membrane-impermeable Nluc inhibitor was present (Figure 2—figure supplement 1A). Thus, our assay likely underestimates SLO-induced exosome secretion. To test whether plasma membrane damage also elicits exosome secretion in a different cell line, we generated a HEK293T reporter cell line that expresses FLAG-Nluc-CD63 under expression of the weak L30 promoter. We observed an increase in FLAG-Nluc-CD63 exosome secretion from this reporter cell line in a SLO dose- and Ca^{2+}-dependent manner (Figure 2—figure supplement 1B). Application of a physiological mechanical stress also induced exosome secretion in a Ca^{2+}-dependent manner (Figure 2E). HCT116 CD63-Nluc cells were pumped slowly through a narrow-gauge needle to simulate a capillary. In the low mechanical stress regime, cells transiently experienced ~89 dyn/cm^2 maximum fluid shear stress, whereas in the high-mechanical stress regime, cells transiently experienced ~178 dyn/cm^2 maximum fluid shear stress (Barnes et al., 2012). This form of mechanical stress increased exosome production but only when $CaCl_2$ was present in the conditioned medium. Endothelium and circulating lymphocytes routinely experience mechanical stress of ~95 dyn/cm^2 and transiently experience up to ~3000 dyn/cm^2 (Barnes et al., 2012).

Next, we used linear iodixanol density gradient fractionation to assess if the Ca^{2+}-dependent increase in extracellular CD63 was attributable to exosomes as opposed to the secretion of intact endosomes contained within plasma membrane-derived vesicles (Jeppesen et al., 2019). EVs from cells treated with ionomycin for 30 min or vehicle for 24 hr were separated on a high-resolution linear iodixanol gradient. A 30 min ionomycin treatment induced the secretion of low-buoyant density, ANXA2- and FLOT2-positive vesicles (Figure 2F, Fraction #8) compared to the 24 hr vehicle control. ANXA2 is a marker for a subpopulation of plasma membrane-derived EVs (Jeppesen et al., 2019). Alternatively, CD63 and Nluc signals equilibrated to higher buoyant density fractions corresponding to the position expected for exosomes (Figure 2F, Fraction #10). A comparison of ionomycin- and vehicle-treated samples showed drug treatment over equivalent times (4 hr) increased the Nluc luminescence in putative exosome fractions (Figure 2G, Fraction #10). Treatment

of cells with ionomycin for 4 hr did not induce apoptotic cell death (Figure 2—figure supplement 1C; Gil-Parrado et al., 2002).

MVBs traffic toward the cell periphery on microtubules or actin filaments (Mittelbrunn et al., 2015). We considered the possibility that Ca^{2+}-dependent exosome secretion depended on MVB traffic on microtubules or actin filaments. Treatment with nocodazole, a microtubule polymerization inhibitor, but not latrunculin A, an actin polymerization inhibitor, reduced vehicle- and ionomycin-induced exosome secretion (Figure 2H, Figure 2—figure supplement 1D and E).

We conclude that the influx of extracellular Ca^{2+} caused by several inducers of plasma membrane lesions triggers exosome secretion and that this secretion is dependent on the anterograde trafficking of MVBs on microtubules.

Identification of candidate proteins involved in Ca^{2+}-dependent exosome secretion

Next, we sought to identify cytosolic proteins that are recruited in a Ca^{2+}-dependent manner to MVBs. Such proteins may be involved in Ca^{2+}-dependent exosome secretion and plasma membrane repair. CD63-Nluc cells were ruptured by homogenization, and a post-nuclear supernatant fraction was supplemented with 1 mM $CaCl_2$ or 1 mM EGTA and mixed with immobilized Nluc antibody in order to immunoprecipitate (IP) MVBs and associated peripheral membrane proteins. After washing the immunoprecipitated MVBs to remove other organelles, Ca^{2+}-dependent MVB binding proteins were eluted from the IP fraction using 2 mM EGTA. MVB proteins retained after the EGTA elution were solubilized using 0.2% TX-100 (Figure 3A). The 0.2% TX-100 elution fractions were significantly enriched in LAMP1 and diminished in GAPDH compared to the input, regardless of the presence of $CaCl_2$ or EGTA in the elution (Figure 3B). A gel stained for total protein showed four intense protein bands unique to the EGTA-eluted sample (Figure 3C). These proteins were absent when the Nluc antibody was omitted or when the post-nuclear supernatant was treated with 1 mM EGTA instead of 1 mM $CaCl_2$. Three sections of the gel were excised and analyzed by mass spectrometry (Figure 3D). We identified annexin A6 (ANXA6) and copine 3 (CPNE3) in the upper gel slice, annexin A2 (ANXA2) in the middle gel slice, and S100 Ca^{2+}-binding protein A10 (S100A10) in the lower gel slice.

ANXA6 depletion blocks Ca^{2+}-dependent exosome secretion and stalls MVBs at the cell periphery

We tested the effect of knocking-down genes encoding the Ca^{2+}-dependent MVB-binding proteins identified in our proteomic analysis. We were unable to knock down ANXA2 using two different shRNAs. However, we were able to efficiently knock down ANXA6 and CPNE3 with two different shRNAs (Figure 4A and B), and in each case, Ca^{2+}-dependent exosome

secretion decreased relative to a GFP knockdown control (Figure 4C and D). One of the ANXA6 shRNAs also slightly decreased constitutive exosome secretion relative to the GFP control, although the effect was relatively small (Figure 4C). A polyclonal knockout of ANXA6 also decreased exosome secretion relative to a non-targeting control (Figure 4—figure supplement 1A and B).

In order to assess how ANXA6 depletion affected exosome secretion, we visualized CD63-positive compartments after Ca^{2+} influx. CD63-Nluc cells were treated with ionomycin or vehicle control for 30 min, fixed, and analyzed using immunofluorescence microscopy. We observed an accumulation of CD63-positive vesicles at the cell periphery, particularly in ionomycin-treated ANXA6 knockdown cells (Figure 4E). We suggest that ANXA6 may be necessary for Ca^{2+}-dependent exosome secretion, possibly at the point of docking between the MVB and the plasma membrane.

Biochemical reconstitution of Ca^{2+}- and ANXA6-dependent exosome secretion in permeabilized cells

Many studies probing genes that may contribute to exosome secretion have relied on depletion or overexpression experiments in live cells. We sought to develop an assay in permeabilized cells to allow a direct assessment of the roles of different gene products in exosome secretion.

SLO is a potent bacterial toxin secreted by group A streptococci that forms stable pores within cholesterol-containing biological membranes in a temperature-dependent manner (Alouf, 1980). SLO has been used to permeabilize cells to reconstitute various intracellular membrane trafficking and organelle exocytosis reactions because it forms stable pores that are large enough to allow the diffusion of large proteins, but not intact organelles, across the plasma membrane (Apodaca et al., 1996; Funato et al., 1997; Martys et al., 1995). We leveraged the cholesterol- and temperature-dependent properties of SLO to establish a permeabilized cell reaction that would allow us to study exosome secretion upon plasma membrane damage.

Reaction components including an ATP regeneration system (ATP^r), GTP, cytosol, and Ca^{2+} were mixed with SLO-permeabilized cells and incubated at 30°C and evaluated for exosome secretion just as in the cell-based exosome secretion assay (Figure 5A). We observed that addition of either rat liver cytosol or Ca^{2+} promoted exosome secretion slightly and that the addition of both rat liver cytosol and Ca^{2+} promoted exosome secretion ~12-fold over the control condition (Figure 5B). The addition of HCT116 WT cytosol and Ca^{2+} promoted exosome secretion ~15-fold over the control condition (Figure 5C). To assess the energy dependence of this reaction, we repeated the experiment using

nucleotide-depleted cytosol in either the absence or presence of the ATP^r and GTP (Figure 5D). We observed that the Ca^{2+}-only reaction was stimulated by the addition of the ATP^r and GTP (columns 3 and 7), whereas the stimulatory effect obtained with cytosol alone appeared to be nucleotide-independent (columns 2 and 6). The Ca^{2+} conditional and partial ATP dependence of the reaction may reflect distinct pools of MVBs, some perhaps already bound to the plasma membrane.

The participation of ANXA6 in the reconstitution was assessed with blocking IgG antibodies targeting epitopes on either GFP or ANXA6. Addition of an anti-GFP antibody slightly decreased exosome secretion whereas the equivalent addition of an anti-ANXA6 antibody (whose specificity was validated by immunoblot analysis in Figure 4A and Figure 4—figure supplement 1A) decreased exosome secretion to a background level seen in a reaction without added cytosol (Figure 5E). These results suggest a direct role of ANXA6 in the docking of MVBs at the cell surface.

ANXA6 truncations localize to different membranes upon ionomycin treatment

After demonstrating that ANXA6 is required for Ca^{2+}-dependent exosome secretion in intact and permeabilized cells, we sought to probe the membrane recruitment of distinct domains of ANXA6 upon Ca^{2+} influx. Previous studies have demonstrated that ANXA6 is recruited to a peripheral 'repair cap' that is formed at the site of plasma membrane lesions (Demonbreun et al., 2016). Unlike other members of the annexin protein family, ANXA6 contains two complete annexin domains, ANXA6(N) and ANXA6(C). To probe the roles of these domains, we generated fluorescent ANXA6 full length (FL), ANXA6(N), and ANXA6(C) fusion constructs and probed their localization in U-2 OS cells by superresolution microscopy.

We observed that ANXA6(FL) maintains a diffuse cytoplasmic distribution in unperturbed cells (Figure 6A). However, upon addition of ionomycin, ANXA6(FL) was recruited to both the plasma membrane (as indicated by wheat germ agglutinin [WGA] counterstain) and to intracellular vesicles, a portion of which were CD63-positive (Figure 6A). We also observed the budding of plasma membrane-derived vesicles in the presence of ionomycin. These may correlate to the low-buoyant density vesicles marked by ANXA2 and FLOT2 that were released from ionomycin-treated cells (Figure 2F, Fraction #8). Next, we expressed fluorescently tagged ANXA6(N) and ANXA6(C) constructs and assessed their localization upon the addition of DMSO or ionomycin, relative to the plasma membrane and CD63, respectively (Figure 6B and C). Similar to ANXA6(FL), ANXA6(N) and ANXA6(C) displayed cytoplasmic localization in unstimulated cells. Upon ionomycin treatment, we observed recruitment of ANXA6(N), but not ANXA6(C) to the cell periphery, relative to the WGA counterstain (Figure 6B). In contrast to ANXA6(N), we observed that ANXA6(C) became

enriched at intracellular membrane structures, a portion of which were positive for CD63 (Figure 6C). These two domains may serve to dock MVBs to the plasma membrane.

Conclusions

Our results suggest that exosome secretion is coupled to Ca^{2+}-dependent plasma membrane repair in HCT116 and HEK293T cells (Figure 7). We established cellular and biochemical exosome secretion assays to recapitulate and interrogate this process. Targeted proteomics was used to demonstrate that ANXA6 is recruited to MVBs in the presence of Ca^{2+}. We show, both in intact and permeabilized cells, that ANXA6 is required for Ca^{2+}-dependent exosome secretion. We then provide evidence that that ANXA6 depletion stalls MVBs at the cell periphery upon Ca^{2+} ionophore treatment. Finally, we demonstrate that truncations of ANXA6 are enriched at different cellular membranes upon cytosolic Ca^{2+} elevation.

Exosomes are secreted upon damage to the plasma membrane

We demonstrate that SLO-treated or mechanically stressed HCT116 CD63-Nluc and SLO-treated HEK293T FLAG-Nluc-CD63 cells secrete exosomes in response to Ca^{2+}-dependent plasma membrane repair (Figure 2 and Figure 2—figure supplement 1B). Such treatments may mimic conditions of physiologic stress in vivo and lead to wound-induced EV secretion. This may contribute to the diversity of EVs present in biological fluids, including in samples used for liquid biopsy. Plasma membrane repair is common, especially in certain tissues. In rats, 6.5% of cells in the vascular endothelium of the aorta undergo plasma membrane repair at a given time (Yu and McNeil, 1992); 20% of muscle cells repair their membrane after muscle contractions (McNeil and Khakee, 1992). Motile cancer cells also have high rates of plasma membrane repair (Bouvet et al., 2020).

Interestingly, Whitham, 2018 demonstrated that exercise stimulates the release of EV-associated proteins and myokines into circulating plasma (Whitham, 2018). In this study, a cohort of human participants had blood drawn from their femoral artery before and after 60 min of acute exercise on a cycle ergometer. Label-free quantitative proteomic analysis showed an increase in proteins such as CD63, TSG101, CD9, and ANXA2 within EVs isolated from plasma by differential centrifugation postexercise. It is tempting to speculate that the increase in EV secretion is caused by increased plasma membrane repair. We postulate that exosome secretion during plasma membrane repair may allow for simple detection of tissue-specific damage during the routine clinical analysis of blood or urine samples.

The biological functions of exosomes released during Ca^{2+}-stimulated secretion remain unclear. Much attention has focused on the role of exosomes in intercellular

communication (Meldolesi, 2018). A recent study from our laboratory established quantitative assays to measure the functional delivery of exosome cargo to recipient cells (Zhang and Schekman, 2023). Functional transfer of exosome cargo was inefficient, whereas functional intercellular transfer occurred quite effectively through the formation of open-ended membrane tubular connections. However, we do not exclude the possibility that exosomes and other EVs may functionally convey their cargo to recipient cells in specific physiological contexts (Ridder et al., 2014). Alternatively, a recent study showed that exosomes act as 'decoys' for pore-forming toxins such as α-toxin (Keller et al., 2020). During staphylococcus infection, cells upregulate exosome production. Instead of binding to the plasma membrane, α-toxin binds to exosomes. Correspondingly, we find that SLO binds exosomes at concentrations that may compete with plasma membrane binding (Figure 2—figure supplement 1A). Ca^{2+}-dependent exosome secretion allows for the rapid secretion of high levels of exosomes and may serve as a defense against bacterial toxins that perforate the plasma membrane.

Role of ANXA6 in exosome secretion

We find that ANXA6 is required for Ca^{2+}-dependent fusion of MVBs with the plasma membrane (Figure 4). Annexin proteins are known to be required for plasma membrane repair (Blazek et al., 2015; Bouter et al., 2015; Boye and Nylandsted, 2016; Croissant et al., 2021; Gerke and Moss, 2002; Koerdt et al., 2019). Depletion of ANXA6 compromises plasma membrane repair, and the N-terminal domain of ANXA6 is insufficient for membrane repair (Croissant et al., 2020; Potez et al., 2011; Swaggart et al., 2014). In addition to lysosome exocytosis, plasma membrane repair is accompanied by shedding of damaged membrane at the cell surface (Andrews and Corrotte, 2018). Annexins have been invoked in the capping and shedding of plasma membrane lesions (Demonbreun et al., 2016). Our results extend these conclusions to the fusion of MVBs at the cell surface.

Our data favors a model where ANXA6 is directly involved in tethering an MVB to the plasma membrane during exocytosis. ANXA6 is recruited to CD63-positive compartments in a Ca^{2+}-dependent manner (Figure 3). Additionally, CD63-positive membrane compartments stall near the plasma membrane in Ca^{2+}-stimulated, ANXA6-depleted cells (Figure 4E). This conclusion is strengthened by our observation that an anti-ANXA6 antibody blocks exosome secretion in permeabilized cells (Figure 5E). Unlike other members of the annexin family, ANXA6 contains two distinct annexin domains, possibly one for each membrane partner of a fusion pair. Upon ionomycin stimulation, we observed that the N-terminal annexin domain, but not the C-terminal annexin domain, was recruited to the plasma membrane and that the C-terminal annexin domain became enriched at intracellular membrane structures, a portion of which were CD63-positive (Figure 6B and

C). ANXA6 has also been demonstrated to tether liposomes in vitro in the presence of Ca^{2+} (Buzhynskyy et al., 2009). Alternative roles in docking, such as SNARE interactions or actin remodeling as seen for other annexins, remain possible (Gabel et al., 2015; Gerelsaikhan et al., 2012). Additionally, a recent study has demonstrated that the annexin isoform ANXA11 serves as a molecular tether that allows RNA granules to 'hitchhike' on moving lysosomes for their transport (Liao et al., 2019).

Figures:

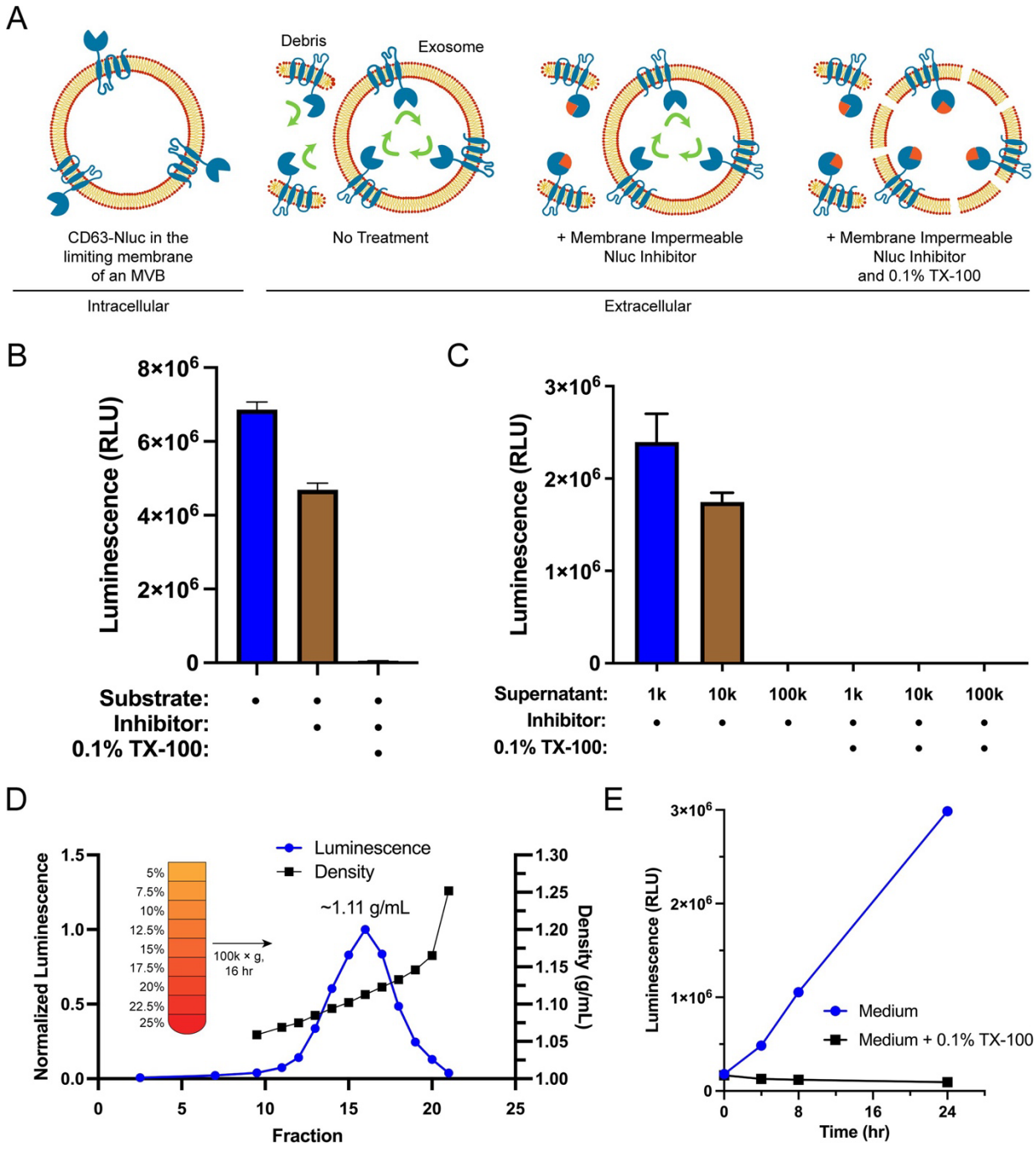

1. Endogenous CD63-nanoluciferase (Nluc) is a faithful reporter of exosome secretion. (**A**) Schematic illustrating the topology of CD63-Nluc in different membranes and the cellular CD63-Nluc secretion assay. (**B**) Luminescence from the conditioned medium of CD63-Nluc cells with or without furimazine, the membrane-impermeable Nluc inhibitor, and 0.1% TX-100 are shown. (**C**) Luminescence derived from the supernatant fraction of CD63-Nluc conditioned medium subjected to differential centrifugation (1k, 10k, and 100k) with or without 0.1% TX-100 are shown. (**D**) Membrane-protected luminescence (in blue circles) and buoyant density (in black squares) of CD63-Nluc conditioned medium subjected to a high-resolution linear density gradient are shown. (**E**) Membrane-protected luminescence from CD63-Nluc conditioned medium collected over 24 hr with (blue circles) or without 0.1% TX-100 (black squares). Data plotted represent the means of three independent experiments, and error bars represent SDs. Note, for Figure 1D and E, the error bars are smaller than the dots in the image.

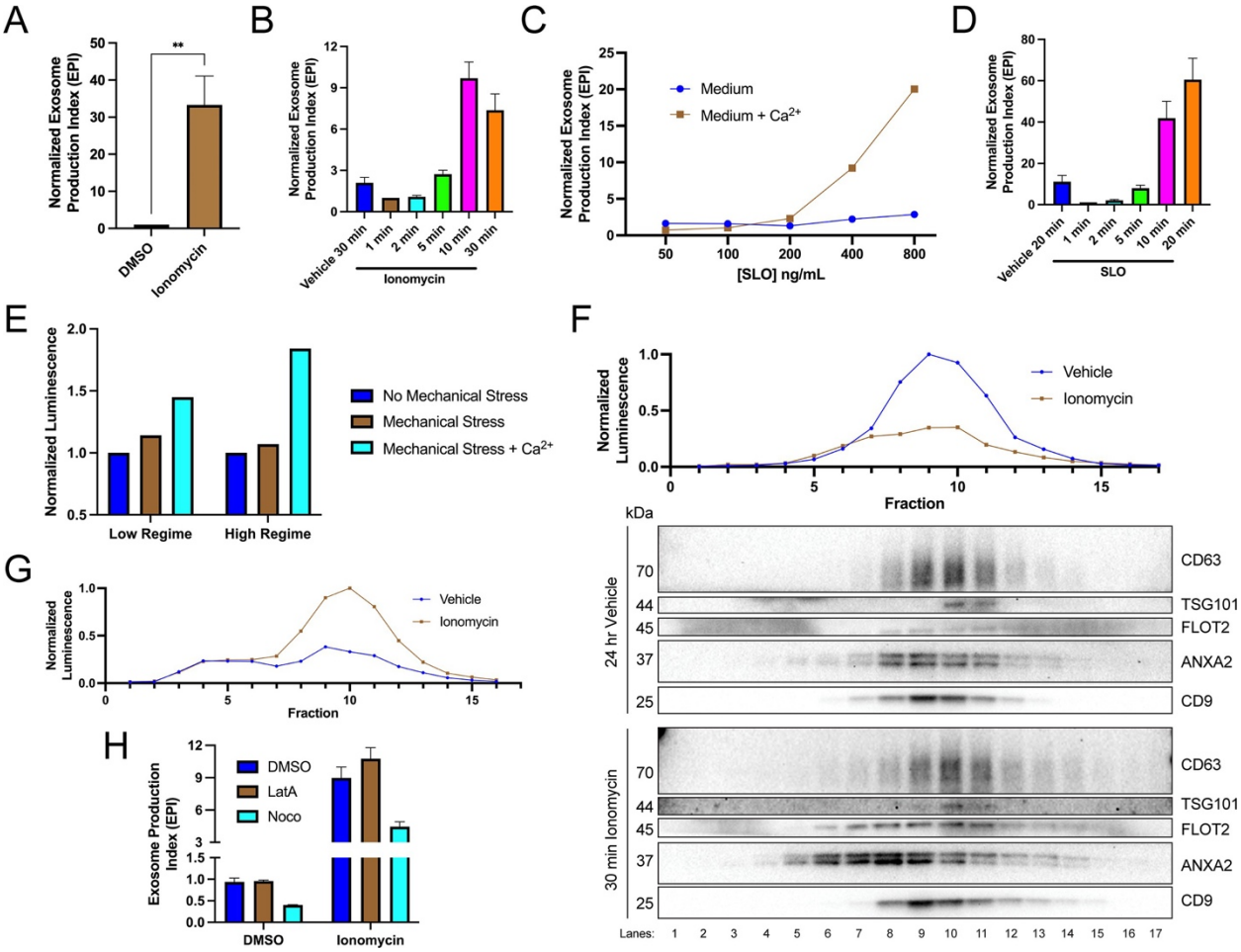

2. Elevation of cytosolic Ca^{2+} levels promotes exosome secretion. (**A**) Normalized exosome production from CD63-nanoluciferase (Nluc) cells treated with 5 μM ionomycin or DMSO (ionomycin vehicle) are shown. (**B**) Relative rate of exosome

secretion over time is shown. CD63-Nluc cells were treated with DMSO or 5 μM ionomycin for the indicated times, and the normalized exosome production index was calculated. (**C**) Normalized exosome production from CD63-Nluc cells treated for 30 min with increasing concentrations of streptolysin O (SLO), with or without 1.8 mM extracellular Ca^{2+}. Note, error bars are smaller than the dots in the image. (**D**) Relative rate of exosome secretion over time is shown. CD63-Nluc cells were treated with PBS or 250 ng/ml SLO for the indicated time points, and the normalized exosome production index was calculated. (**E**) Normalized luminescence derived from CD63-Nluc cells treated with a high or low dose of mechanical stress, with or without 1.8 mM extracellular Ca^{2+}. (**F**) Iodixanol gradient fractionation of conditioned medium 100k × g pellet fraction is shown. Conditioned medium from cells treated for 30 min with 5 μM ionomycin or 24 hr vehicle is compared. Line graphs show distribution of CD63-Nluc luminescence (with membrane-impermeable inhibitor added) across the linear gradient. Immunoblots show distribution of several extracellular vesicle (EV) markers across the linear gradient. (**G**) Iodixanol gradient fractionation of conditioned medium 10k × g supernatant fractions are shown. Conditioned medium from cells treated for 4 hr with 5 μM ionomycin or 4 hr vehicle is compared. Line graphs show distribution of CD63-Nluc luminescence (with membrane-impermeable inhibitor added) across the linear gradient. (**H**) Normalized exosome production from 30 min of 5 μM ionomycin or DMSO vehicle, co-treated with DMSO vehicle, 1 μM latrunculin A (LatA), or 10 μM nocodazole (Noco) is shown. Data plotted represent the means from three independent experiments, and error bars represent SDs. Statistical significance was performed using a Student's T-test (**$p<0.01$).

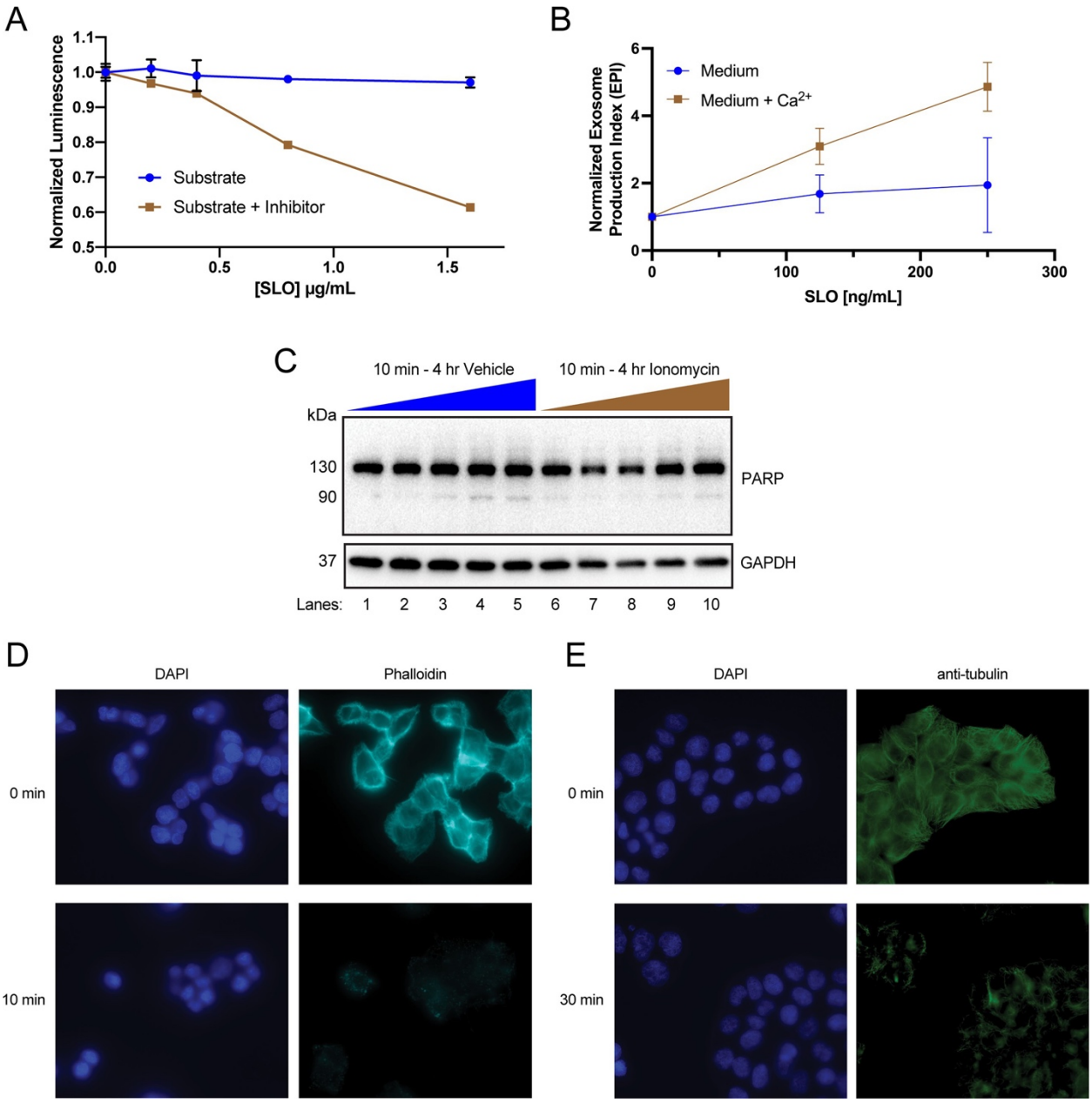

S2. Elevation of cytosolic Ca^{2+} levels promotes exosome secretion.

(**A**) Normalized luminescence derived from the 10k × g conditioned medium supernatant from CD63-nanoluciferase (Nluc) cells with or without the addition of the membrane-impermeable Nluc inhibitor, as a function of increasing streptolysin O (SLO) concentrations, is shown. (**B**) Normalized exosome production from HEK293T FLAG-Nluc-CD63 cells treated for 20 min with increasing concentrations of SLO, with or without 1.8 mM extracellular Ca^{2+}. (**C**) PARP and GAPDH immunoblots from HCT116 CD63-Nluc cells during a 4 hr ionomycin (5 µM) time course. (**D**) Phalloidin staining after treatment with 1 µM latrunculin A or (**E**) tubulin immunofluorescence after treatment with 10 µM

nocodazole. Data plotted represent the means from three independent experiments, and error bars represent SDs.

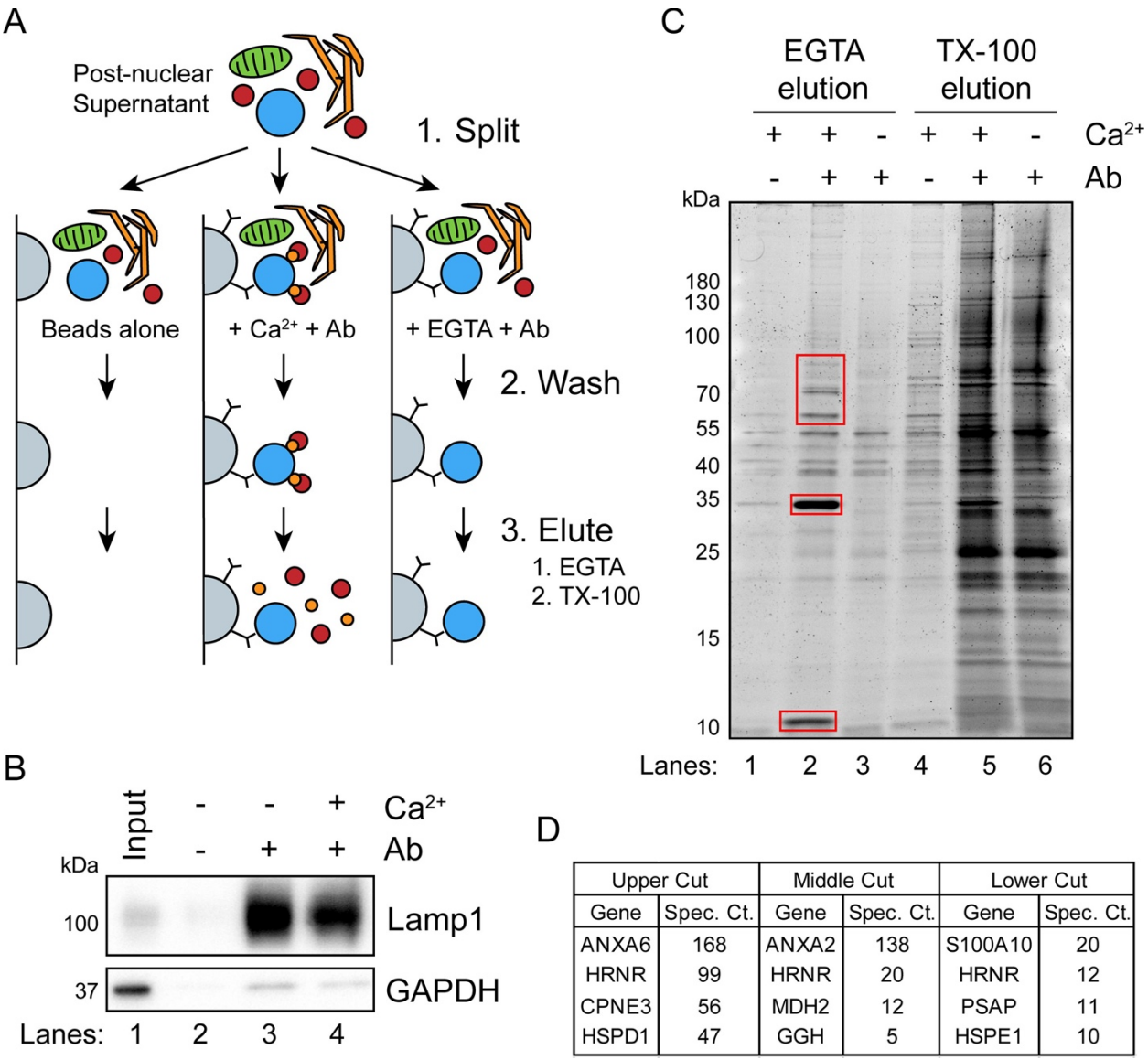

Upper Cut		Middle Cut		Lower Cut	
Gene	Spec. Ct.	Gene	Spec. Ct.	Gene	Spec. Ct.
ANXA6	168	ANXA2	138	S100A10	20
HRNR	99	HRNR	20	HRNR	12
CPNE3	56	MDH2	12	PSAP	11
HSPD1	47	GGH	5	HSPE1	10

3. A targeted proteomics approach identifies genes important for Ca^{2+}-dependent exosome secretion.

(A) Schematic illustrating the isolation of Ca^{2+}-dependent multivesicular body (MVB)/lysosome binding proteins (Ab: antibody; gray-beads, blue-MVB, green-mitochondria, orange-ER, red-proteins, and gold-Ca^{2+}). (B) Immunoblot analysis of LAMP1 and GAPDH from the TX-100 elutions, relative to the input, is shown. (C) Total protein gel (Sypro Ruby stained) of eluted fractions is shown. Red boxes indicate gel cuts sent for proteomic analysis. (D) Table depicting the top four proteomic hits from each gel cut are shown, excluding keratin family proteins.

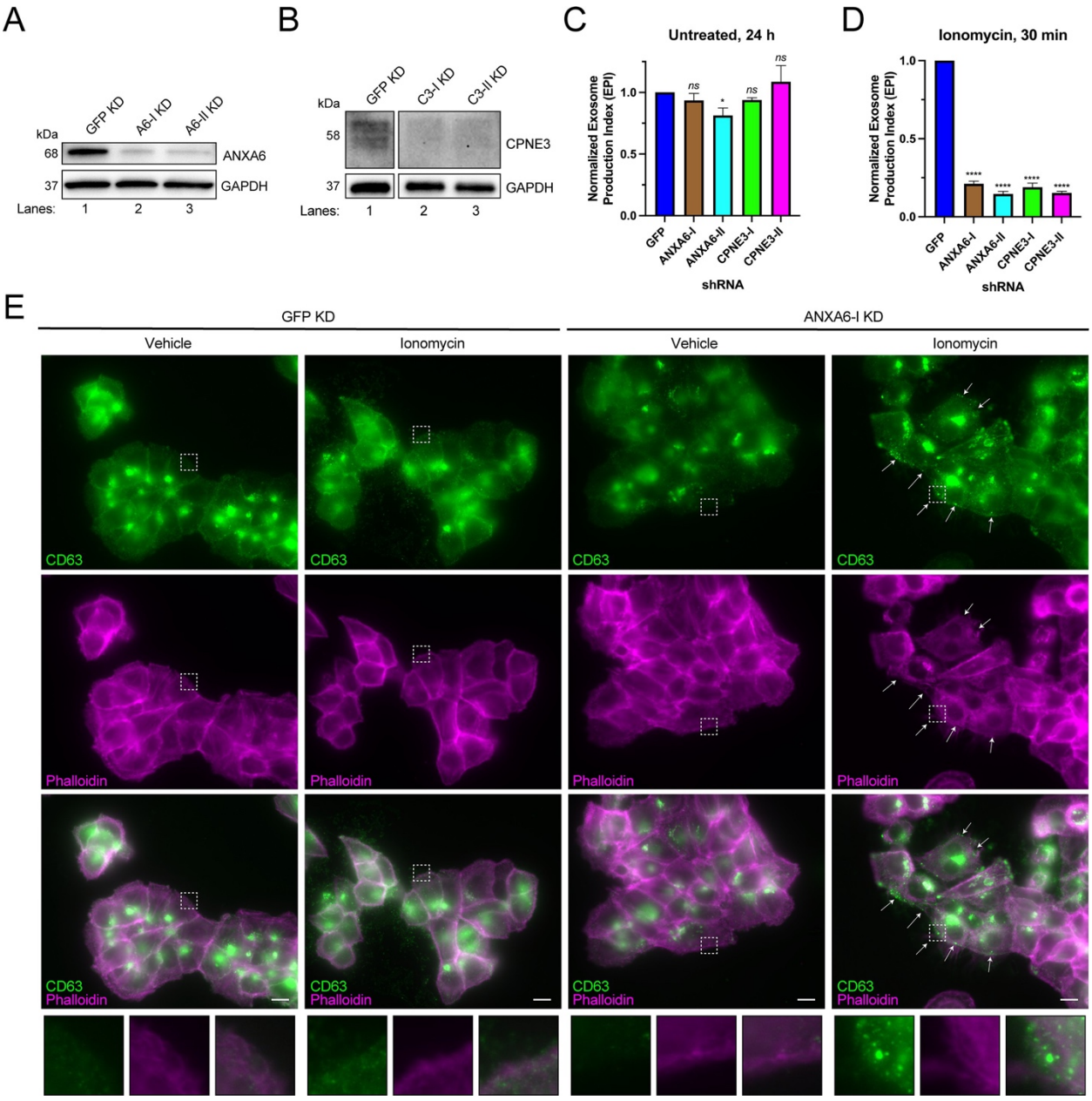

4. ANXA6 depletion blocks ionomycin-mediated exosome secretion and stalls multivesicular bodies (MVBs) at the cell periphery.

(A) Immunoblot analysis of ANXA6 and GAPDH expression from GFP, ANXA6-I, and ANXA6-II shRNA CD63-nanoluciferase (Nluc) cells is shown. (B) Immunoblot analysis of CPNE3 and GAPDH expression from GFP, CPNE3-I, and CPNE3-II shRNA CD63-Nluc cells are shown. (C) Normalized exosome production derived from GFP, ANXA6-I, ANXA6-II, CPNE3-I, and CPNE3-II shRNA CD63-Nluc cells grown in conditioned medium for 24 hr are shown. (D) Normalized exosome production derived from GFP, ANXA6-I, ANXA6-II, CPNE3-I, and CPNE3-II shRNA CD63-Nluc cells treated with 5 μM ionomycin for 30 min are shown. Data plotted represent the means from three independent experiments, and error bars represent

SDs. Statistical significance was performed using an ANOVA (*p<0.05, ****p<0.0001, and ns = not significant). (E) CD63 immunofluorescence and phalloidin staining of GFP or ANXA6-I shRNA CD63-Nluc cells after 30 min of DMSO or 5 μM ionomycin treatment are shown. White arrows indicate peripheral CD63 puncta. Scale bars: 10 μm.

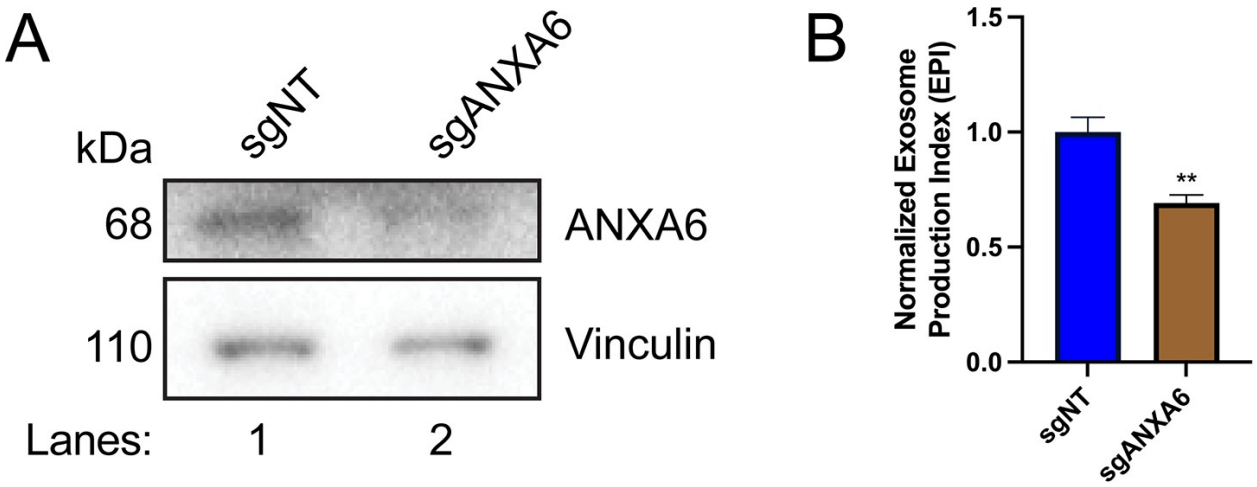

S4. Exosome secretion from polyclonal ANXA6 KO cells.

(A) Immunoblot analysis of ANXA6 and vinculin expression from sgNT and sgANXA6 CD63-Nluc cells are shown. (B) Normalized exosome production derived from sgNT and sgANXA6 CD63-Nluc cells treated with 5 μM ionomycin for 30 min is shown. Data plotted represent the means from three independent experiments, and error bars represent SDs. Statistical significance was performed using a Student's T-test (**p<0.01).

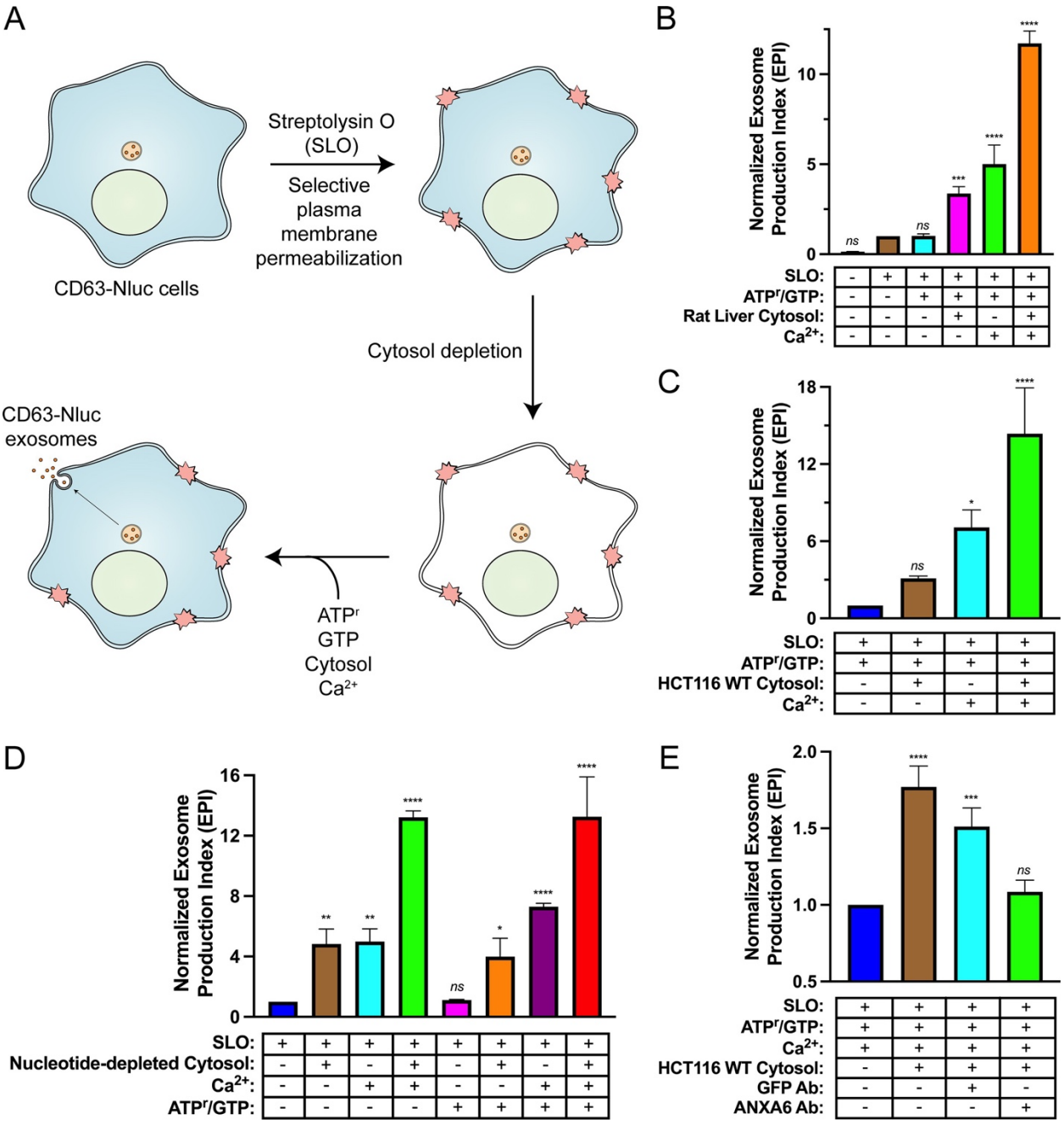

5. Biochemical reconstitution of Ca^{2+}- and ANXA6-dependent exosome secretion in permeabilized cells.

(A) Schematic illustrating the permeabilized cell exosome secretion assay. (B) Permeabilized cell exosome secretion reactions with or without SLO, ATP regeneration system (ATP^r)/GTP, rat liver cytosol, and Ca^{2+} are indicated. (C) Permeabilized exosome secretion assays with or without HCT116 WT cytosol and Ca^{2+} are shown. (D) ATP requirements for the permeabilized exosome secretion assay. Reactions with or without nucleotide-depleted rat liver cytosol, Ca^{2+}, and ATP^r/GTP are indicated. (E) Requirement of ANXA6 in the permeabilized exosome secretion assay. Reactions with or without HCT116

WT cytosol, an anti-GFP rabbit IgG antibody, and an anti-ANXA6 rabbit IgG antibody are depicted. Data plotted represent the means from three independent experiments, and error bars represent SDs. Statistical significance was performed using an ANOVA (*$p<0.05$, **$p<0.01$, ***$p<0.001$, ****$p<0.0001$, and ns = not significant).

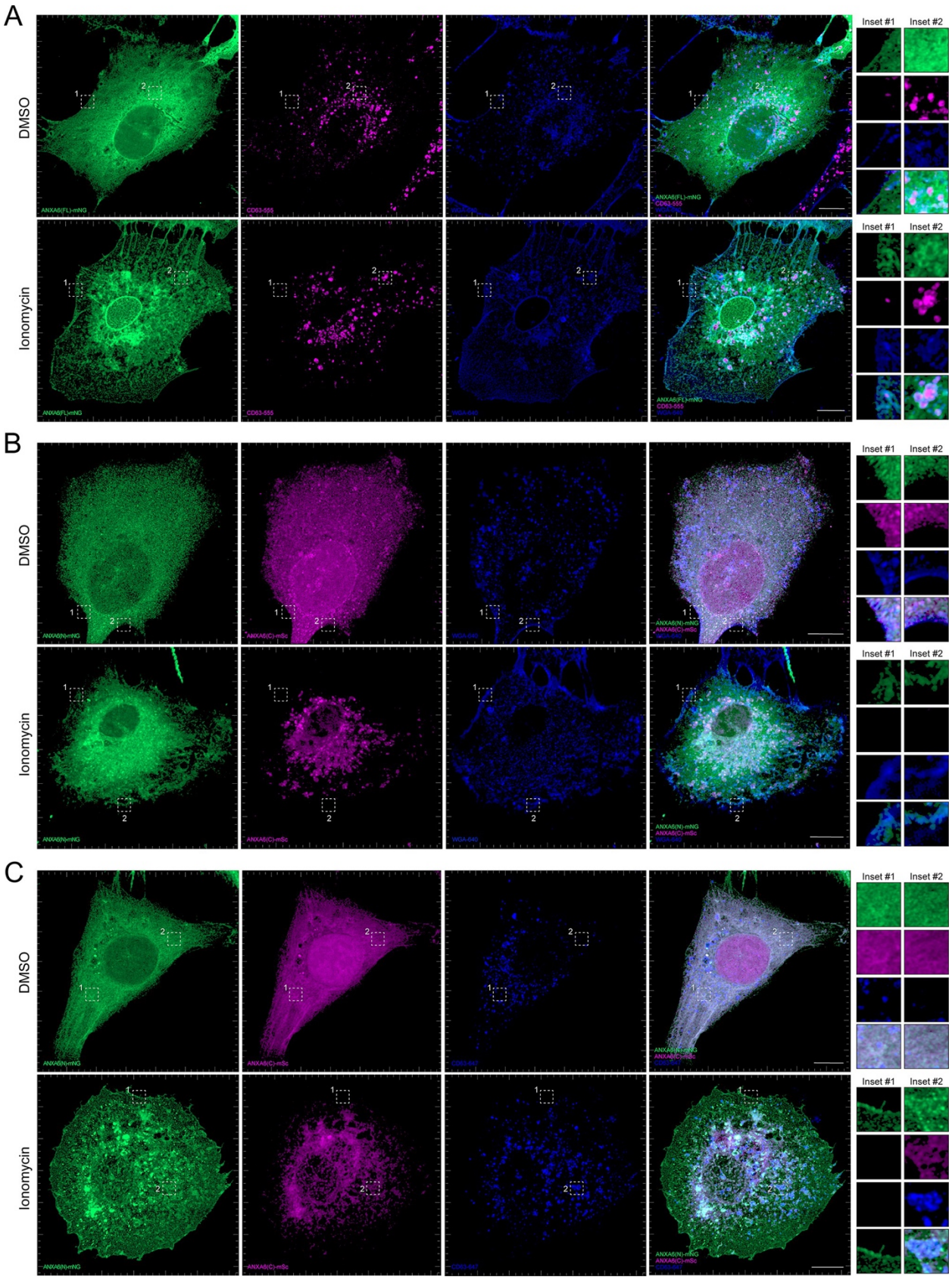

6. Localization of full-length and truncated ANXA6 constructs with or without

ionomycin treatment.
(A) Airyscan 3D projection of U-2 OS cells expressing ANXA6(FL)-mNG with endogenous CD63 and wheat germ agglutinin (WGA) counterstain upon treatment with DMSO or 1 µM ionomycin for 10 min. Green: ANXA6(FL)-mNG; magenta: endogenous CD63 immunofluorescence; blue: WGA CF640R conjugate. Scale bars: 10 µm. (B) Airyscan 3D projection of U-2 OS cells expressing ANXA6(N)-mNG and ANXA6(C)-mSc with WGA counterstain upon treatment with DMSO or 1 µM ionomycin for 10 min. Green: ANXA6(N)-mNG; magenta: ANXA6(C)-mSc; blue: WGA CF640R conjugate. Scale bars: 10 µm. (C) Airyscan 3D projection of U-2 OS cells expressing ANXA6(N)-mNG and ANXA6(C)-mSc with endogenous CD63 upon treatment with DMSO or 1 µM ionomycin for 10 min. Green: ANXA6(N)-mNG; magenta: ANXA6(C)-mSc; blue: endogenous CD63 immunofluorescence. Scale bars: 10 µm.

Chapter 2: Calpains Orchestrate Secretion of Annexin-containing Microvesicles during Membrane Repair

Attribution Statement: Portions of this chapter are adapted from previously published work: Williams et al. *JCB* 2025. The author of this document performed experiments, wrote portions of the initial draft, helped edit and organize the manuscript, and helped write the initial draft of the response to reviewers.

Introduction: EVs are enriched in annexins (Jeppesen et al., 2019), which bind to phospholipids in the presence of calcium. Annexins have roles in plasma membrane repair. Knockdowns of several individual annexins cause defects in membrane resealing in cultured cells (Koerdt and Gerke, 2017; Sønder et al., 2019). Muscle cells experience high rates of membrane damage *in vivo* due to repeated contractions and are dependent on the membrane repair machinery for survival. For example, 20% of muscle fibers in rat triceps are disrupted after eccentric exercise (McNeil and Khakee, 1992). Consistent with annexins playing a role in muscle repair, annexin mutations cause muscular dystrophy in mice (Defour et al., 2017; Swaggart et al., 2014). Upon plasma membrane damage, extracellular calcium flows into the cytoplasm. In the presence of micromolar calcium, annexins bind to membranes and may plug lesion sites by tethering membranes (Croissant et al., 2021). These membranes may come from intracellular organelles or from reticulation of the plasma membrane (Croissant et al., 2020). After annexin recruitment, annexin^{+} MVs are shed from the lesion (Foltz et al., 2021). Recently, Jeppesen et al. separated annexin-rich MVs from exosomes using density gradient centrifugation (Jeppesen et al., 2019). The contents, mechanism of their shedding, and roles of annexin-rich MVs in membrane repair are not understood.

Calpains are cytosolic, calcium-dependent cysteine proteases that, like annexins, have roles in membrane repair. Calpain-1/μ-calpain and calpain-2/m-calpain were the first characterized calpains and are highly abundant across tissues. Calpain-1 and calpain-2 have separate large subunits but share a small subunit. Calpain-3 – calpain-14 are less abundant and may be restricted to specific tissues (Shapovalov et al., 2022). Like many annexin knockouts, loss of calpain-1 and/or calpain-2 leads to impaired membrane resealing in cell culture (Prislusky et al., 2024) and severe muscular dystrophy in mice (Piper et al., 2020). Mutations in the muscle specific calpain-3 produce limb-girdle muscular dystrophy type R1 (Croissant et al., 2021). As with annexins, calpains are activated by micromolar concentrations of calcium *in vitro*. Because calpain targets include membrane-cytoskeleton anchors, it has been speculated that calpain-1/2 locally detach the plasma membrane from the cytoskeleton around the lesion site (Mellgren et al., 2009). In other systems, calpains also appear to be necessary for MV formation. Platelets

release MVs called microparticles during activation and clotting. Microparticle formation in platelets requires sustained elevation of cytosolic calcium and is blocked by calpain inhibitors (Fox et al., 1991). It is unknown if calpains cleave other proteins and facilitate repair and MV formation independently of membrane-cytoskeleton detachment.

Membrane repair appears to be important for cancer cell migration and metastasis (Gounou et al., 2023). Additionally, membrane repair protects cancer cells against T cell-mediated cytotoxicity (Ritter et al., 2022). To characterize membrane repair and mechanisms of MV secretion in cancer cells, we isolated and identified proteins within annexin$^+$ MVs produced by cells grown in culture. After finding several calcium-activated proteins implicated in membrane repair in MVs, we measured annexin secretion in MVs after membrane damage. Addition of sublytic levels of the pore forming toxin, streptolysin O, induced ~20-40-fold increase in vesicular annexin A2 secretion. We found that secreted annexin A1 and annexin A2 are cleaved by calpain-1/2, and that annexins in general are primary targets for calpains. Given that both annexins and calpains are required for membrane repair, we sought to understand the interplay of these proteins during membrane repair. Using an intracellular annexin A2 cleavage reporter, we found that annexin A2 was cleaved after membrane recruitment and wound scabbing, but before secretion. We show that cleaved annexin A2 is deficient in membrane and effector protein binding, and cleavage dissociates annexin A2-linked membranes. Mutant annexin A2 that cannot be cleaved by calpains was recruited normally after membrane damage but was secreted at lower levels in MVs compared to wildtype annexin A2. Our results link membrane repair to MV secretion and establish a chronology of annexin and calpain function during membrane repair.

Materials and Methods:

Cell lines, media, general chemicals, DNA, and RNA

HEK293T, C2C12 HCT116, and all HCT116-derived cell lines were grown at 37°C in 5% CO_2 in Dulbecco's Modified Eagle's Medium (DMEM) supplemented with 10% fetal bovine serum (FBS) (Thermo Fisher Scientific, Waltham, MA, USA). Cells were routinely tested, and found negative, for mycoplasma contamination with the MycoAlert Mycoplasma Detection Kit (Lonza Biosciences). HCT116, C2C12, and HEK293T cells were authenticated by the UC Berkeley Cell Culture Facility using STR profiling. For Figures 1 and S1, HCT116 or HEK293T cells were incubated in EV-depleted medium produced by ultracentrifugation of DMEM supplemented with 25% FBS at 186,000 × g (40,000 RPM) for 24 h using a Type 45Ti rotor. Ultracentrifuged medium was then diluted to 10% FBS with DMEM. For SILAC experiments, HEK293T cells were grown in High Glucose DMEM for SILAC (Athena Enzyme Systems), supplemented with 10% dialyzed FBS (Thermo Fisher Scientific, Waltham, MA,

USA) for 2 wk prior to exosome isolation. DMEM was supplemented with GlutaMax, L-leucine (800 µM), L-methionine (200 µM), and either L-lysine (800 µM) and L-arginine (400 µM) or L-lysine $^{13}C_6$, $^{15}N_2$ (800 µM) and L-arginine $^{13}C_6$, $^{15}N_4$ (400 µM). EV-depleted SILAC medium was prepared as described for EV-depletion of normal medium. C2C12 cells were differentiated for 5 d in DMEM supplemented with 2% horse serum and 1 µM insulin. Antibodies for immunoblot were: rabbit anti-vinculin (Abcam ab129002), rabbit anti-annexin A6 (Abcam 201024), rabbit anti-annexin A1 (Abcam ab214486), rabbit anti-annexin A2 (Abcam ab185957), rabbit anti-calpain 1 (Proteintech 10538-1-AP), mouse anti-CD63 (BD Biosciences 556019), rat anti-CD63 (LSBio LS-C179520), mouse anti-alix (Santa Cruz sc-53540), mouse anti-flotillin-2 (BD Biosciences 610384), rabbit anti-CD9 (CST D801A), mouse anti-tubulin (Abcam ab7291), rabbit anti-streptolysin O (GeneTex GTX64171), mouse anti-NanoLuc (R&D Systems MAB10026), rabbit anti-HA (CST C29F4), rabbit anti-LC3 (Novus NB100-2220), rabbit anti-Lamp1 (CST D2D11). RNA for mRNA-seq was purified using the Direct-zol RNA Miniprep kit (Zymo Research).

Lentivirus production and transduction

The pLJM1 backbone was used for stable expression of annexin A2 and S100A10 in HCT116 cells. Fusion protein domains were separated by $(GGSG)_2$ linkers. For low expression of annexin A2-Nluc (Figure 2, S2, S3), wt/Tr/Mt-annexin A2-mScarlet/mNeonGreen (Figure 5, S5), wt/Tr/Mt-annexin A2-HA (Figure 5) and S100A10-mNeonGreen (Figure 5), the pLJM1 CMV promoter was replaced with the RPL30 promoter. pLJM1 plasmids expressing mNeonGreen-tagged proteins contained puromycin resistance cassettes. For pLJM1 plasmids expressing mScarlet and Nluc-tagged proteins, the puromycin resistance cassette was replaced with a blasticidin resistance cassette. The pLIX403-puro backbone was used for stable, doxycycline-inducible mCherry-VPS4a(E228Q) expression.

HEK293T cells at 40% confluence within a 6-well plate were transfected with 165 ng of pMD2.G, 1.35 µg of psPAX2, and 1.5 µg of a pLJM1 or pLIX403 plasmid using the TransIT-LT1 Transfection Reagent (Mirus Bio) as per the manufacturer's protocol. At 48 h post-transfection, 1 ml of fresh DMEM supplemented with 10% FBS was added to each well. The lentivirus-containing medium was harvested 72 h post-transfection by filtration through a 0.45 µm polyethersulfone (PES) filter (VWR Sciences). The filtered lentivirus was distributed in aliquots, snap-frozen in liquid nitrogen, and stored at –80°C. For lentiviral transductions, we infected HCT116 cells with filtered lentivirus in the presence of 8 µg/ml polybrene for 24 h, and the medium was replaced. HCT116 cells were selected using 1 µg/ml puromycin or 4 µg/ml blasticidin S for 4 days and 6 d, respectively. Gene expression was assessed by immunoblot analysis.

Immunoblotting

Cells were washed once with PBS and lysed in TBS containing 1% TX-100, 1 mM EGTA, and a protease inhibitor cocktail (1 mM 4-aminobenzamidine dihydrochloride, 1 µg/ml antipain dihydrochloride, 1 µg/ml aprotinin, 1 µg/ml leupeptin, 1 µg/ml chymostatin, 1 mM phenylmethylsulfonyl fluoride, 50 µM N-tosyl-L-phenylalanine chloromethyl ketone, and 1 µg/ml pepstatin), and incubated on ice for 10 min. The whole cell lysate was centrifuged at 1,000 × g for 10 min at 4°C and the post-nuclear supernatant was diluted with 6× Laemmli buffer (without DTT) to a 1× final concentration. Samples were heated at 95°C for 5 min and proteins resolved on 4–20% acrylamide Tris-glycine gradient gels (Life Technologies). Proteins were then transferred to polyvinylidene difluoride membranes (EMD Millipore, Darmstadt, Germany), blocked with 5% bovine serum albumin (BSA) in TBS, washed 3× with TBS-T and incubated overnight with primary antibodies in 5% BSA in TBS-T. The membranes were then washed again 3× with TBS-T, incubated for 1 h at room temperature with 1:10,000 dilutions of anti-rabbit or anti-mouse secondary antibodies (GE Healthcare Life Sciences, Pittsburgh, PA, USA), washed 3× with TBS-T, washed once with TBS and then detected with ECL-2 or PicoPLUS reagents (Thermo Fisher Scientific) for proteins from cell lysates or EV isolations, respectively.

Synchronized SLO Treatment

Lyophilized SLO (Sigma) was pre-activated in PBS containing 10 mM DTT at 37°C for 1 h, distributed in aliquots into low-retention microcentrifuge tubes, snap-frozen in liquid nitrogen, and stored at –80°C until use. The protein concentration of the SLO batch was determined by a Bradford assay. HCT116 cells plated two days before (70-80% confluent) were washed with cold PBS and incubated in prechilled DMEM (w/o Calcium), 1 mM EGTA, and the indicated SLO concentration for 15 min at 4°C. Cells were washed once with cold PBS and replaced with prewarmed 37°C DMEM (w/o Calcium) + 1.8 mM $CaCl_2$ and incubated for 20 min at 37°C.

Crude, High-Speed Extracellular Vesicle Pellet Centrifugation

Conditioned medium from 8 x 15 cm plates (240 ml) was harvested from untreated (Figure 1) or 200 ng/ml SLO-treated (Figure S2g, 3a, 3b, 4e) HCT116 cells. All subsequent manipulations were completed at 4°C. Cells and large debris were removed by low-speed sedimentation at 1,000 × g for 15 min in a Sorvall R6 +centrifuge (Thermo Fisher Scientific) followed by medium-speed sedimentation at 10,000 × g for 15 min using a fixed angle FIBERlite F14–6×500 y rotor (Thermo Fisher Scientific). The supernatant fraction was then centrifuged at 29,500 RPM (~100k x g) for 1.25 h in a SW32 rotor. The high-speed pellet fractions were resuspended in PBS unless otherwise stated and pooled (600 µl total).

EV fractionation by buoyant iodixanol density gradient equilibration

Fresh aliquots of 5.4, 10.8, 16.2, and 21.6% (v/v) iodixanol solutions were prepared by mixing appropriate volumes of PBS and Solution D (PBS and 54% (w/v) iodixanol). A 27% (v/v) iodixanol solution was prepared by mixing the resuspended high-speed pellet fraction with Solution D. Iodixanol gradients were prepared by sequential 1 ml overlays of each iodixanol solution in a 5 ml SW55 tube, starting with the 27% iodixanol solution and finishing with the 5.4% iodixanol solution. Gradients were centrifuged in a SW55 rotor at 36,500 RPM for 16 h with acceleration set at a minimum level and no brake. Fractions (350 µl) were collected from top to bottom. Density measurements were taken using a refractometer. Each fraction was diluted in 6× Laemmli buffer (without DTT) for immunoblot analysis.

EV fractionation by buoyant sucrose step gradient equilibration

Fresh aliquots of 10, 40, and 60% (v/v) sucrose solutions were prepared in 20 mM Tris (pH 7.4). A 55% (v/v) sucrose solution was prepared by mixing the resuspended high-speed pellet with the 60% sucrose solution. Sucrose gradients were prepared by sequentially layering 1 ml of the 40% and 10% sucrose solution over 3 ml of the 55% sucrose solution in a 5 ml SW55 tube. Gradients were centrifuged in a SW55 rotor at 36,500 RPM for 16 h with minimum acceleration and no brake. Fractions (400 µl) were collected from top to bottom. Density measurements were taken using a refractometer. Each fraction was diluted in 6× Laemmli buffer (without DTT) for immunoblot analysis.

For SILAC experiments, after flotation, the 3rd and 4th fraction from the top of gradient were diluted with 10 ml PBS and centrifuged to sediment EVs. Pellet fractions were resuspended in TBS + 2% SDS, and protein concentration was determined using a microBCA kit (Thermo). Fraction 3 protein (1 µg) from heavy cells was mixed with Fraction 4 protein (1 µg) from light cells and vice versa. Glycerol (10%) was added to both mixes and samples were loaded onto a SDS page gel. Proteins were electrophoresed into the stacking gel, and the gel was stained using Sypro Ruby using the overnight protocol (Thermo). Protein samples were excised from the gel, digested in-gel with trypsin, and analyzed by quantitative mass spectrometry.

Exosome Pulldowns

For $CD63^+$ EV immunoprecipitation, Protein G Magnetic Dynabeads (50 µl) (Thermo Fisher Scientific) were washed twice with 200 µl PBS using a magnetic rack to capture beads between washes. The resuspended high-speed pellet fraction and 1 µg anti-CD63 (clone H5C6, BD Biosciences), were added to the beads and incubated with rotation overnight at 4°C. The beads were washed 3x with 600 µl cold PBS, incubating for 1 min between

washes. EVs were eluted with 30 µl PBS + 0.1% Triton X-100 for 5 min. Fractions were diluted in 6× Laemmli buffer (without DTT) for immunoblot analysis.

For pulldown of EVs with exposed phospholipids using annexin A5, the high-speed extracellular vesicle pellet fraction from 2 x 15 cm plates of SLO-treated cells was resuspended in 200 ul of annexin binding buffer (10 mM HEPES pH 7.4, 140 mM NaCl, 2mM calcium chloride). Biotin-X ANXA5 (5 µl) (Thermo Fisher Scientific) was added, mixed, and incubated for 15 min at room temperature. Annexin binding buffer (350 µl) and 50 µl of Steptavidin Dynabeads (Thermo Fisher Scientific), prewashed with 50 µl annexin binding buffer, was added to the binding reaction and incubated for 10 min. The beads were washed twice with 400 µl annexin binding buffer and eluted with 200 µl of 10 mM HEPES pH 7.4, 140 mM NaCl, 2mM EGTA, 0.1% TX-100. Fractions were diluted in 6× Laemmli buffer (without DTT) for immunoblot analysis.

ANXA2-Nluc and CD63-Nluc secretion assay

Assays were performed as described previously (Williams et al., 2023), with slight modifications. HCT116 CD63-Nluc or ANXA2-Nluc cells were grown to ~80% confluence in 24-well plates. All subsequent manipulations were performed at 4°C. Conditioned medium (200 µl) was taken from the appropriate wells, added to a microcentrifuge tube, and centrifuged at 1000 × g for 15 min in an Eppendorf 5430 R centrifuge (Eppendorf, Hamburg, Germany) to remove intact cells. Supernatant fractions (150 µl) from the low-speed sedimentation were passed through a 0.45-micron filter (96-well format) by centrifuging at 1000 × g for 5 min. Filtered fractions (50 µl) were used to measure luminescence. During these centrifugation steps, the cells were placed on ice, washed once with cold PBS, and lysed in 200 µl of PBS containing 1% TX-100 and protease inhibitor cocktail.

To measure vesicular Nluc secretion, we prepared a master mix containing the membrane-permeable Nluc substrate and a membrane-impermeable Nluc inhibitor using a 1:1000 dilution of Extracellular NanoLuc Inhibitor and a 1:333 dilution of NanoBRET Nano-Glo Substrate into PBS (Promega, Madison, WI, USA). Aliquots of the Nluc substrate/inhibitor master mix (100 µl) were added to 50 µl of the supernatant fraction from the medium-speed centrifugation and vortexed briefly, and luminescence was measured using a Promega GlowMax 20/20 Luminometer (Promega, Madison, WI, USA). For the intracellular normalization measurement, the luminescence of 50 µl of cell lysate was measured using the Nano-Glo Luciferase Assay kit (Promega, Madison, WI, USA) as per the manufacturer's protocol. The EV production index (EPI) for each sample is calculated as follows: EPI = medium/cell lysate.

Isolation of cytosol from cultured human cells

Isolations were performed as described previously (Williams et al., 2023), with slight modifications. HCT116 WT cells were grown to ~90% confluence in 150 mm dishes. All subsequent manipulations were performed at 4°C. Each 150 mm dish was washed once with 10 ml of cold PBS and then harvested by scraping into 5 ml of cold PBS + 1 mM EGTA. The 5 ml cell suspensions from either 4 (Figure 4a, 4b) or 20 (Figure 4i-j) 150 mm dishes were combined. Cells were then collected by centrifugation at 200 × g for 5 min, and the supernatant fraction was discarded. The cell pellet was resuspended in 2 vol of lysis buffer (TBS, 1 mM EGTA, 0.2 mM PMSF, and for Figure 4i-j, 10 μM E64) and placed on ice. Cells were mechanically lysed by 15 strokes through a 22-gauge needle. Cell lysates were centrifuged at 1000 × g for 15 min to sediment intact cells and nuclei, and the post-nuclear supernatant was then centrifuged at 49,000 RPM for 15 min in an TLA-55 ultracentrifuge (Beckman Coulter). The supernatant (cytosol fraction) was collected conservatively without disturbing the pellet.

Protein purification of ANXA2, ANXA2-S100A10 Complex, ANXA2-HaloTag

Pet28a vectors expressing ANXA2, S100A10, or ANXA2-HaloTag were transformed into Rosetta (DE3) BL21 *E. coli*, and grown in 250 ml LB cultures at 37°C. At O.D. 600 = 0.5, protein expression was induced with 50 μM IPTG. Cultures were grown overnight at 18°C and centrifuged at 3k x g for 10 min. Pellet fractions were kept at -80°C until time for purification. Pellet samples were thawed and resuspended in 7.5 ml *E. coli* Lysis Buffer (1x TBS, 1x Protease Inhibitor Cocktail, 10 μl Benzonase [NEB], 1 mg/ml lysozyme, 5 mM DTT, 1 mM EGTA). Bacteria were lysed by sonication for 5 sec on (20% power), 20 sec off, 5 times. *E. coli* lysate was centrifuged for 5 min at 1,000 x g at 4°C. The supernatant fraction was removed and transferred to a high-speed, 1.5 ml centrifuge tube (Beckman Coulter). For purification of ANXA2-S100A10 complex only, ANXA2 lysate and S100A10 lysate were mixed 1:1. 2 mM $CaCl_2$ (final) was added and incubated for 5 min at room temperature. Lysates were centrifuged at >100k x g (49k RPM) in a TLA 55 for 10 min and the supernatant was discarded. The membrane pellet was resuspended with a 5 ml annexin wash buffer (1x TBS, 5 mM $CaCl_2$, 5 mM ATP, 5 mM DTT), using a 25-gauge needle for thorough resuspension. The resuspended pellet was centrifuged again at 100k x g (49k RPM) in a TLA 55 rotor for 10 min. The supernatant fraction was carefully removed, and the membrane pellet resuspended with 1 ml annexin elution buffer (1x TBS, 5 mM DTT, 10 mM ATP). DTT was replaced with TCEP for downstream labeling of the eluted annexin A2 with quencher. The resuspended pellet fraction was centrifuged again at 100k x g (49k RPM) in a TLA 55 for 10 min. The supernatant fraction was carefully removed, and aliquots were flash frozen in liquid nitrogen for storage at -80°C. For labeling, annexin A2-Halo (14 μM) elution was mixed with 16 μM JF646 Halo Ligand (Promega). For self-quenched annexin A2-Halo, 286 μM Tide Quencher 5WS-Maleamide (AAT Bioquest) was also added to this reaction and

incubated overnight at 4°C. The maleamide reaction was quenched with 5 mM DTT and unreacted Halo Ligand and Quencher were removed using two Bio-Spin 6 (Tris) columns (Bio-rad).

Protein purification of dCAPN1 and dCAPN2

Human dCAPN1[C115S]-3xFlag-6xHis and dCAPN2[C105S]-3xFlag-6xHis were both cloned into PetDuet-1 coexpressing CAPNS1(86-269). *E. coli* cultures were grown at 37°C in 200 ml cultures to an O.D.600 of 0.5, and expression induced with 50 uM IPTG. Cultures were grown overnight at 18°C. *E. coli* were centrifuged at 3k x g for 10 min and resuspended in 5ml TBS + 0.2 mM PMSF. Cells were sonicated 5 times (5 sec on 15 sec off, 20% power), and lysates sedimented at 10k x g for 15 min. Supernatant fractions were applied to HisPure beads (500 µl of slurry) pre-washed with lysis buffer. Slurries were rotated at 4°C for 1 h and then washed 3 x with 5 ml 1.5x TBS + 20mM imidazole and centrifuged at 600 x g after washes to collect beads. Protein was eluted with 1 ml 1x TBS + 300mM imidazole. Aliquots (50 µl) were snap frozen in liquid nitrogen.

Capture of CAPN1 and CAPN2 Substrates and Interactors

$CaCl_2$ (2mM final) was added to E64-containing cytosol isolated as described above and incubated for approximately 1 h. In parallel, 125 µl anti-Flag agarose beads (Chromotek) were sedimented at 1k x g for 2 min and resuspended in 300 µl wash buffer (TBS + 1mM $CaCl_2$ + 0.01% Tween-20). The resuspended beads were split into 3 tubes. Flag (3x) peptide, dCAPN1-3xFlag, or dCAPN2-3xFlag bait were added to the beads (6 µM final for each bait) in a 300 µl reaction. Bait proteins were bound to beads for 1 h at 4°C. Beads were wash once with 500 µl wash buffer and once with 500 µl lysis buffer (TBS + 10µM E64 + 0.2mM PMSF + 1 mM EGTA), with centrifugation at 1k x g for 2 min between washes to sediment beads. $CaCl_2$-containing lysate (1.5 ml) was added to each of the 3 conditions and incubated for 2 h at 4°C. Beads were washed 3 with 1ml wash buffer, with centrifugation at 1k x g for 2 min between washes to sediment beads. Calpain substrates were eluted with 100 µl elution 1 buffer (TBS + 5mM EGTA), and stable calpain interacting proteins were eluted with 100 µl elution 2 (TBS + 1x Laemmli Buffer).

Measurement of plasma membrane permeabilization by SLO over time

For measurement of plasma membrane permeabilization in bulk, we resuspended dissociated HCT116 cells in PBS + 5 mM EGTA. Cell slurries (50 ul, 4 x 10^5 cells per reaction) were incubated on ice in a qPCR plate with the indicated concentration of SLO. Cells were sedimented at 300 x g and resuspended in 50 µl of ice-cold PBS + 5 mM EGTA + 2.5 µM SYTOX Green (Thermo Fisher). The plate was sealed with optical film and placed in a qPCR machine (Bio-Rad CFX96) pre-cooled to 4°C and then rapidly heated to 37°C with

fluorescence measured every 20 sec using SYBR green settings. For measurement of plasma membrane permeabilization with microscopy, we grew HCT116 cells to 70% confluence in a 35 mm glass bottom dish (MatTek). Cells were placed in a 37°C, 5% CO_2 chamber on an LSM900 microscope and then washed once with 1 ml Ca^{2+}-free DMEM and incubated with Ca^{2+}-free DMEM + 200 ng/ml SLO + 2.5 µM SYTOX Green. Where indicated, 1 mM Ca^{2+} was added to the incubation media. SYTOX Green uptake was measured by imaging with the 10x objective, taking images every 10 sec for 10 min.

GUVs and Liposomes

For GUV assays, we mixed lipids in the following molar ratios: 38.5:20:20:3:18.5 DOPC:POPE:DOPS:PIP(4,5)P2:cholesterol (1 µmole total lipid) in 500 µl of 5% methanol, 95% chloroform. The lipid mix was smeared onto two indium tin oxide-coated glass plates, and for 30 min solvent was evaporated under vacuum on a heat block preheated to 55 °C. A circular rubber spacer coated with vacuum grease was placed on the glass slide into which buffer was introduced (1mM Tris pH 7.4, 250 mM sucrose), followed by covering with a second glass slide. Electrodes were clipped to each plate, and the chamber was placed in a 50°C oven. A function generator was used to apply an electric field (10 Hz, 1.4 V) for 90 min. For the last 30 min, the frequency was decreased by 0.5 Hz every 5 min. The GUV-containing solution was drained from the chamber and mixed with GUV buffer (5 mM Tris pH 7.4, 250 mM glucose). After settling to the bottom of the slide overnight at 4°C, GUVs were resuspended in GUV buffer with 2 mM $CaCl_2$ and 5 mM TCEP and mixed with combinations of 1 µM ANXA2-Halo-JF646 and 1 µM S100A10-mScalet.

For liposome assays, we mixed lipids in a glass beaker in the following molar ratios: 38:20:20:3:0.5:18.5 DOPC:POPE:DOPS:PIP(4,5)P2:TexasRed-PE:cholesterol (1 umol total lipid) in 500 ul of 5% methanol, 95% chloroform. The lipid mix was placed on a heat block preheated to 55 °C and solvent was evaporated under vacuum for 30 min. Lipids were resuspended in degassed TBS and incubated at 55 °C with intermittent vortexing for 15 min. The lipid solution was pumped 15 times through an extruder with a 200-micron filter. Liposomes were diluted 1:5 into TBS with 2 mM $CaCl_2$ and 5 mM TCEP, with indicated combinations of 300 nM untagged ANXA2, ANXA2-S100A10 complex, and porcine CAPN-I.

Microscopy and Laser Ablation

The images in Figure 5i-j, S2e, S5d, were acquired on an Echo Revolve Microscope using the 10× air objective. For image quantification in Figure 5i-j, the “Analyze Particles” function in ImageJ was used to quantify aggregates area. The images in Figure 2a, 2c, S2a-d, 4h, 5c, 5e, 5g S5b, and 6d were acquired using an LSM900 confocal microscope system (ZEISS) using confocal mode, a 63× Plan-Apochromat, NA 1.40 objective, and a heated, CO_2

controlled chamber. Cells were bathed in DMEM with 2.5 μM FM1-43 (Biotium) added where indicated. For laser ablations using the LSM900, a 1 μM x 1 μM square was positioned over the edge of a cell not adjacent to another cell. The 1 μM x 1 μM square was ablated for 100-200 iterations using the UV laser at 100% power.

Repair caps were quantified in Zen 3.1 (Zeiss) by measuring intensities within a box that encapsulated the repair cap. This intensity was normalized to a boxed piece of membrane that was not ablated.

Results

Annexins and other calcium-responsive proteins are secreted within microvesicles

To characterize microvesicles (MVs) secreted in culture, we utilized serial centrifugation followed by equilibrium density gradient centrifugation. This established method separates EVs based on their buoyant density (Shurtleff et al., 2018). Following a 1k x g centrifugation to remove cells and further centrifugation at 10k x g to remove large EVs, small EVs were sedimented from conditioned medium at 100k x g. Sedimented particles were resuspended and placed at the bottom of an iodixanol gradient and centrifuged to separate HCT116-derived small EVs into a low-density, annexin$^+$ population and a high-density, CD63$^+$ population (Figure 1a). The CD63$^+$ population is thought to represent exosomes, and the annexin A2$^+$ population is thought to represent a subpopulation of MVs (Jeppesen et al., 2019). Vesicles centrifuged from conditioned medium were immunoprecipitated with CD63 antibody (Figure 1b). Known exosome markers, CD9 and alix, coprecipitated with CD63$^+$ vesicles, but annexin A1 did not. CD63$^+$ vesicle proteins were immunoisolated only when anti-CD63 antibody was pre-conjugated to the beads (Figure S1a). We assessed whether annexins were localized to the lumen or the extracellular face of MVs by proteinase K treatment. We found that annexin A2 mostly localized to the lumen of MVs (Figure 1c). Luminal flotillin-2 and annexin A2 sedimented with EVs even in the presence of the membrane impermeable calcium chelator, EGTA, and both were degraded by proteinase k only in the presence of Triton X-100.

Using stable isotope labeling by amino acids in cell culture (SILAC), we identified proteins enriched in the low-density fraction relative to the high-density fraction. EVs secreted by HEK293T cells grown with heavy arg/lys or light arg/lys amino acids were collected from conditioned medium, centrifuged at 100k x g, and pellet material was resuspended and placed beneath a sucrose step gradient (Figure 1d). After separation by high-speed centrifugation (Figure S1b), heavy amino acid labeled, low buoyant density EVs, collected from the 10-40% sucrose interface, were mixed with light amino acid labeled, high buoyant EVs, collected from the middle of the 40% sucrose fraction (and vice versa)

prior to mass spectrometry analysis. As expected, conventional exosome proteins (CD63, ESCRTs, syntenin-1, etc.) were enriched in the high buoyant density fraction (Figure 1e, Table S1). Conversely, in the low buoyant density fractions Ca^{2+}-responsive proteins including annexins, EHD proteins (EHD1, EHD4), plasma membrane snare machinery (SNAP23, STXBP3), and the Ca^{2+}-transporting ATPase (ATP2B1) were enriched. Annexin, EHD (Demonbreun et al., 2016), and snare (Zhen et al., 2021) proteins are all implicated in plasma membrane repair. As expected for plasma membrane derived vesicles, we also detected several plasma membrane proteins including CD276 and CD59.

Membrane damage stimulates secretion of annexin $A2^+$ microvesicles from the repair site

We showed previously that in addition to exosomes, secretion of this annexin $A2^+$ EV population is stimulated by the Ca^{2+} ionophore, ionomycin (Williams et al., 2023). In addition, we have previously visualized secretion of annexin $^+$ MVs from muscle cells during Ca^{2+}-dependent membrane repair (Foltz et al., 2021). Given these previous data, and our proteomics results, we speculated that secretion of these vesicles might be stimulated by membrane damage. First, we visualized (Figure 2a, Video 1-2) and quantified (Figure 5h) FM1-43 staining of HCT116 cells after laser ablation wounding. FM1-43 is membrane impermeable but can stain intracellular membranes brightly if the plasma membrane is disrupted. Within 1 min of ablation, a repair scab of brightly stained membranes formed at the ablation site. For several min after ablation, intracellular membranes slowly stained, suggesting the lesion site was plugged but not fully sealed. As dye influx slowed, vesicles were shed from the damaged cell. These vesicles were intensely stained at a level comparable to the repair site, possibly indicating they were shed directly from the repair site. In addition, as vesicles were shed over the next 5 min, the repair scab slowly lost staining intensity.

Next, we visualized annexin dynamics after laser ablation. We focused on annexin A2, as total mRNA-seq revealed that annexin A2 was likeley the most abundant annexin in HCT116 cells (Figure 2b). Indeed, there were twice as many annexin A2 reads as the rest of the annexin reads combined. This difference is not due to a difference in transcript size, as annexin A1, A2, A3, and A5 are all ~1.5 kilobases in length. Less than 1 min after ablation, annexin A2 was rapidly recruited to the membrane around the lesion site (Figure 2c). For the next 5-10 min after recruitment, annexin $A2^+$ vesicles were shed from the ablation site. As these vesicles were shed, the membrane-recruited annexin A2 dissipated. The morphology of the repair scab varied (Figure S2a). Occasionally, annexin $A2^+$ filopodia-like structures emerged rapidly after ablation, before shedding from the damage site. We also observed size variation in annexin $A2^+$ EVs, ranging from 1 μm (Figure S2b) to 100-200 nm

(Figure 2c). In these larger vesicles, we could distinguish complete recruitment of annexin A2 to the membrane, suggesting that the Ca^{2+} concentration in these vesicles was significantly higher than the intracellular concentration. We also compared repair site recruitment of annexin A2 to annexin A1 (Figure S2c) and annexin A6 (Figure S2d). More annexin A2 was recruited compared to A1 or A6, further indicating that annexin A2 was the most abundant annexin in HCT116 repair scabs.

To quantitatively access vesicle shedding during membrane repair, we used the pore forming toxin, streptolysin-O (SLO), to damage the plasma membrane. We began to observe increased cell death at 800 ng/ml SLO as assessed by SYTOX Green staining after treatment (Figure S2e). Thus, we considered treatments of 200 ng/ml SLO and less, sublytic. We synchronized pore formation by pre-incubating cells at 4°C with SLO. At this temperature, SLO binds to the plasma membrane but does not open into a pore (Corrotte et al., 2015). Cells were washed to remove excess SLO, after which pores open synchronously as the temperature was raised to 37°C.

To assess the dynamics of pore formation using this system, we measured uptake of SYTOX Green into HCT116 cells in Ca^{2+}-free medium. Because the repair machinery requires Ca^{2+} influx, under these conditions, SLO pores remained open and were not repaired (Corrotte et al., 2015). SLO pores opened within 40 sec to 1 min, as measured by the length of the lag phase in SYTOX Green uptake (Figure 2d). Next, we applied SLO to cells expressing a low level of annexin A2-nanoluciferase (Nluc). Using an assay described previously that measures luminal luciferase activity (Williams et al., 2023), we quantified secretion of membrane enclosed annexin A2-Nluc over time (Figure 2e, S2f). Neither annexin A2-Nluc nor CD63-Nluc were secreted within the first two min of SLO treatment. By 5 min, both annexin A2-Nluc and CD63-Nluc secretion peaked, and by 10 min secretion had ceased. Accounting for the 1 min it took for SLO pores to open, vesicle secretion initiated 1 min after pore formation and peaked after about 4 min. Next, we measured annexin$^+$ MV secretion at increasing concentrations of SLO (Figure 2f). Annexin A2-Nluc reached maximal secretion with 100-200 ng/ml SLO whereas CD63-Nluc, a marker of exosomes, did not reach maximal secretion within the tested concentration range. Annexin A2$^+$ MV secretion was stimulated at lower levels of damage, whereas late endosome exocytosis is required at higher levels of damage.

Membrane repair and repair cap shedding involves the phospholipid scramblases, TMEM16F or TMEM16E (Foltz et al., 2021; Wu et al., 2020). We speculated that annexin$^+$ EVs may have high levels of anionic phospholipids, such as phosphatidylserine, on the extracellular leaflet if they are derived by budding from the plasma membrane repair site. We found that annexin A1$^+$ and A2$^+$ EVs were more efficiently captured by an immobilized

form of the phosphatidylserine-binding protein annexin A5 compared to CD63$^+$ and Alix$^+$ exosomes (Figure S2g). Thus, annexin$^+$ EVs are enriched in phosphatidylserine and/or phosphatidylethanolamine in their outer membrane leaflet.

Membrane repair also requires Endosomal Sorting Complexes Required for Transport (ESCRT) machinery (Jimenez et al., 2014). Although some reports suggest ESCRTs and annexins work in tandem during membrane repair (Sønder et al., 2019), others have reported independent activity (Jimenez et al., 2014). ESCRT-mediated vesicle fission depends upon the ATPase activity of Vps4. Inducing short term expression of dominant negative VSP4a diminished vesicular annexin A2-Nluc signal compared to the uninduced control (Figure S2h). We conclude that annexin$^+$ MV shedding during membrane repair at least partially depends on the ESCRT pathway.

Annexins within microvesicles have altered apparent molecular weight

Next, we examined the role of extracellular Ca^{2+} in secretion of these annexin$^+$ vesicles. Significant levels of annexin proteins were detected in buoyant fractions of a sucrose density gradient, but only when Ca^{2+} was present in the medium (Figure 3a). We noted that annexin A1 and A2 within MVs migrated at a lower apparent molecular weight. No such annexin mobility shifts were detected in cell lysates even after SLO treatment (Figure 3b). We confirmed that annexin proteins were secreted in a distinct vesicle fraction from exosomes after SLO treatment. As expected annexin A1, A2, and A6 were present in a low-density fraction, relative to high-density, CD63$^+$ exosomes (Figure 3c). Annexin A6 also appeared to shift in molecular weight, although the apparent molecular weight change was much larger for annexin A6 (~70kDa to ~35 kDa) than for annexin A1 (~38kDa to ~34kDa) or A2 (~37kDa to ~35 kDa). Because muscle cells experience some of the highest rates of membrane damage, we examined this effect using C2C12 cells. As with tumor cells, myotubes, differentiated from C2C12 cells, secreted EVs with apparently processed annexins in response to SLO treatment (Figure S3a).

We speculated that SLO pores may be present on annexin$^+$ vesicles derived from the secreted plasma membrane repair scab. Indeed, others reported such pores on vesicles secreted from SLO-treated cells (Romero et al., 2017). In our experiments, SLO was secreted predominantly on larger vesicles that sedimented at 10k x g (Figure S3b). We reasoned that such perforated vesicles would be accessible to membrane impermeable compounds. As expected, a larger fraction of annexin A2-Nluc secreted in larger vesicles was accessible to a membrane impermeable Nluc inhibitor compared to annexin A2-Nluc secreted in smaller vesicles (Figure S3c). We conclude that cells secrete both perforated and sealed EVs in response to membrane damage.

Calpain-1/2 proteases cleave annexins during microvesicle shedding

We investigated the basis of the apparent molecular weight change of the annexins in MVs. Annexins are substrates for phosphorylation by kinases including Src or PKC (Bharadwaj et al., 2013), and for proteolysis by enzymes including metalloproteases (Blume et al., 2012), plasmin, cathepsins, and calpains (Williams et al., 2010). We tested the role of Ca^{2+} in the apparent molecular weight change for annexins and found that addition of 1 mM in a lysate of HCT116 cells resulted in a rapid conversion of annexin A2 (Figure 4a).

Calpains are a well characterized family of Ca^{2+}-dependent proteases that are necessary for membrane repair in cells. Calpains 1 & 2 are the highest expressed calpains across tissues and have ~10 fold higher transcript levels in HCT116 cells compared to other calpains (Jin et al., 2023). Addition of the highly specific calpain 1 & 2 inhibitor, calpastatin domain I (K_i = 15nM), inhibited the apparent molecular weight shift at a concentration near the K_i (Figure 4b). The less specific, membrane permeable calpain inhibitor, ALLN (K_i = 200nM), also inhibited the apparent molecular weight shift near the K_i (Figure S4a). We purified annexin A2-halotag using a one step, tag-free purification method (Figure S4b). Annexin A2-halotag gel mobility-shifted in apparent molecular weight from ~70kDa to ~67kDa when combined with purified calpain-1 and Ca^{2+} (Figure 4c). The cleavage appeared to be remarkably specific, producing only the 67kDa species, even in incubations at equal concentrations of calpain and annexin A2-halotag (2μM). Purified calpain-1 also cleaved recombinant annexin A6 into 35kDa products (Figure S4c, S4d) which matched the shift in apparent molecular weight of annexin A6 in MVs (Figure 3c). The consensus sequence that predicts the substrate specificity of calpain-1/2 is not well defined (Sorimachi et al., 2012). Therefore, we mapped the calpain cleavage site on annexin A2 by mass spectrometry and detected peptides covering the first 50 amino acids of the protein (Figure 4d, Table S2). Mass spectrometry of processed annexin A2 revealed a cleavage that removed the first 18 resulting in a polypeptide starting at residue Thr-19. The conversion of annexin A2 in MVs was blocked in cells treated with ALLN (Figure 4e). We conclude that MV annexins are cleaved by Ca^{2+}-dependent calpain-1/2.

Given that both annexins and calpains are important for membrane repair, we sought to understand the interplay between these two proteins. Based on the location of the cleavage site (Ser-18/Thr-19), we designed a reporter for annexin A2 cleavage by calpain (Figure 4f). Purified annexin A2-halotag was labeled with a fluorescent halo ligand and a maleimide fluorescence quencher. As the only accessible cysteine on annexin A2-halotag is Cys8, the cleavable N-terminus could be site-specifically labeled with the quencher. Addition of calpain-1 to the reporter led to a robust increase in fluorescence *in vitro* as the

N-terminus containing the quencher was cleaved (Figure 4g). Next, we used this reporter in cells, using a previously described delivery protocol (Teng et al., 2018; Walev et al., 2001). Cells were treated with SLO and the reporter in the absence of calcium, and the reporter was allowed to diffuse into the cells. After washing the cells, addition of calcium triggered the repair process and annexin A2 cleavage was visualized in the cells as an increase in halotag-JF646 fluorescence (Figure 4h). Within 1-2 min, bright, cleaved annexin A2-halotag puncta formed on distended parts of the cell surface, presumably at repair scabs. After puncta formation, vesicles could be seen ejecting from these puncta. These vesicles were also brightly stained, similar to the repair scab puncta. Thus, annexin A2 cleavage by calpain is highly localized in cells and occurs after annexin A2 recruitment and scabbing at the plasma membrane.

Many proteins are reported substrates for calpains. We wondered if annexin proteins are primary targets for calpains, or if they represent a minor fraction of total. We developed an unbiased, substrate-trapping approach to identify calpain-1/2 substrates (Figure S4e). Calpains (3xFlag-tagged), inactivated by mutation of the catalytic cysteine to serine, were immobilized on anti-flag beads. Cytosol was incubated with the beads and substrates in the presence of Ca^{2+} bound to the open calpain active site. Addition of EGTA chelated Ca^{2+} to close the active site, which resulted in substrates eluting from the beads. Stable, Ca^{2+}-independent interactors were retained. We coexpressed and purified CAPN1[C115S]-3xFlag-6xHis (dCAPN-I) and CAPN2[C105S]-3xFlag-6xHis (dCAPN-II) each in complex with calpain small subunit, CAPNS1(86-268) (Figure S4f).

Using dCAPN-I and dCAPN-II baits, we captured calpain substrates (EGTA elution) and stable interactors (subsequent SDS elution) from HCT116 cytosol (Figure 4i). Consistent with calpains targeting annexins in the presence of Ca^{2+}, EGTA quantitatively eluted annexin A6 from dCAPN-I and dCAPN-II baits. Many known calpain substrates are targeted by both calpain-1 and calpain-2. Consistent with these observations, the gel patterns of the dCAPN-I and dCAPN-II EGTA elution were similar. Next, we analyzed EGTA elutions using high resolution mass spectrometry and ranked proteins by their exponentially modified protein abundance index in the dCAPN-I sample (Figure 4j, Table S3). As expected, the endogenous calpain-1/2 inhibitor, calpastatin, was captured by dCAPN-I and dCAPN-II baits, but not by the 3xFlag alone control. In addition, we recovered plectin (PLEC), a known calpain substrate that links the cytoskeleton to the plasma membrane (Muenchbach et al., 1998). The significant abundance of PLEC and EPPK1 exclusively in the dCAPN-I and dCAPN-II elutions is consistent with the role suggested for calpains in severing the plasma membrane from the cytoskeleton.

S100A10, annexin A3, annexin A2, and annexin A1 were the top few substrates in the dCAPN-I sample. In addition, we found six other annexins (A4, A5, A6, A7, A11) with lower peptide counts. High levels of all the same annexins were identified in the dCAPN-II sample, but not in the 3xFlag alone control. We also found many novel potential calpain-1/calpain-2 substrates including NSF and AHNAK, the latter of which forms a complex with annexin A2 and S100A10 that may be important for plasma membrane repair (Rezvanpour et al., 2011). Our data suggest that annexins and potentially annexin interactors during membrane repair are a major target for calpain-1/2.

Calpain cleavage decreases annexin A2's membrane binding and scabbing activity

We next considered how cleavage changes annexin behavior at the repair site. To investigate this, we designed two annexin A2 mutants. The published structure of calpain-2 with its endogenous inhibitor, calpastatin, suggests two calpastatin prolines are important for recognition (Hanna et al., 2008). Annexin A2 also has two prolines (Pro-27 and Pro-28) directly adjacent to the calpain cleavage site. Mutating this site (P27D/P28D) rendered calpain incapable of cleaving annexin A2 (Figure 5a). We also created a second truncation mutant, annexin A2(18-339) (tr-annexin A2), that reproduced annexin A2 post-cleavage (Figure 5b). For technical reasons, SLO was added to cells at 37°C. This procedure resulted in delayed, asynchronous pore formation and repair.

Although cleaved annexin A2 retained some Ca^{2+}-dependent membrane association activity *in vitro* (Figure S5a), its membrane binding was attenuated (Figure 5c). High doses of SLO cause large scale translocation of annexins to the plasma membrane (Babiychuk et al., 2009). After HCT116 cells were treated with a high, near-lytic (400 ng/ml) dose of SLO, tr-annexin A2-mNeonGreen was recruited more slowly to the plasma membrane compared to wt-annexin A2-mScarlet. In addition, a significant pool of tr-annexin A2 remained cytosolic unlike wt-annexin A2 which was almost completely recruited to the membrane. Mt-annexin A2 was recruited as quickly as wt-annexin A2 to the plasma membrane (Figure S5b).

S100 proteins bind to and modify annexin function. The first 10-12 amino acid segment of annexin A2 binds to S100A10 (K_d = 13nM) (Réty et al., 1999). Thus, we predicted that calpain-cleaved annexin A2 would be incapable of interacting with S100A10. Immunoprecipitation of wt- and mt-annexin A2-HA captured S100A10. As expected, however, tr-annexin A2-HA no longer coprecipitated S100A10 (Figure 5d). Because previous reports suggest that annexin A2 may interact with other S100 proteins (Jaiswal et al., 2014), we tested the specificity of the annexin A2-S100A10 interaction. Using annexin A2-Halo or calpain-treated annexin A2-Halo as bait, we captured annexin A2 interacting proteins (Figure S5c). Two proteins of apparent molecular masses of 10 and 40 kDa appeared in the

annexin A2-halo elution, but not in the calpain-treated annexin A2-halo elution. Gel excision-mass spectrometry identified these proteins as annexin A2 and S100A10, with no peptides mapping to any other S100 protein.

Annexin A2 and S100A10 formed an oligomer (Figure S5f). We wished to test the possibility that this oligomer promoted the tight recruitment and membrane bridging activity of annexin A2. A reduced binding of S100A10 might account for the lowered membrane recruitment of tr-annexin A2. The membrane recruitment of S100A10 was enhanced in comparison to wt-annexin A2 after HCT116 cells were treated with a high dose of SLO (Figure 5e). We noted that S100A10 required annexin to bind membranes (Figure S5d) and was destabilized and degraded *in vivo* after annexin A2 depletion (Bharadwaj et al., 2021). This suggested that all membrane recruited S100A10 is bound to a pool of annexin A2 and that calpain dissociates the S100A10-annexin A2 dimer of dimers.

We confirmed that annexin A2 is required for membrane repair in our HCT116 cell model. Using a CRISPR Cas9 intron trapping approach (Reber et al., 2018), we generated an annexin A2 knockout (Figure 6b). Scabbing/plugging was monitored over time in the presence of a high concentration of Sytox Green (2.5 μM) and SLO. After 6 min of SLO treatment, significantly more Sytox Green entered annexin A2 knockout cells compared to wildtype HCT116 cells (Figure 5f). This difference was dependent on addition of calcium to the medium (Figure S5e). In a 37°C incubation, SLO binding and pore formation took closer to 3-4 min (Figure S5e), suggesting that the increased Sytox Green influx in annexin A2 KO cells occurred within 2 min of pore formation. We next tested the effect of annexin A2 KO on repair scab formation (Figure 5g, 5h). Wild-type cells ablated with a laser in the presence of FM1-43 revealed a brightly stained repair scab distended from the ablation site by 1 min post injury. This repair scab was nearly absent in annexin A2 KO cells. We conclude that annexin A2 knockout caused a defect in scabbing during the early stages of membrane repair.

Annexin A2-S100A10 dimer of dimers aggregate liposomes *in vitro* (Drücker et al., 2013) in a manner that may resemble lesion site scabbing *in vivo*. We purified both annexin A2 and annexin A2-S100A10 dimer of dimers (Figure S5f) and mixed them with liposomes. Addition of annexin A2 or, to a larger extent, addition of annexin A2-S100A10 caused liposomes to aggregate (Figure 5i-j). Addition of calpain-1 dissolved annexin A2 and annexin A2-S100A10 liposome aggregates. Thus, calpain cleavage reduces annexin A2 membrane recruitment, terminates annexin A2-S100A10 association, and dissolves annexin A2-mediated membrane scabs.

The catalytic activity of the calpains is upregulated by $PI(4,5)P_2$ allowing the proteins to partially associate with membranes in vivo (Leloup et al., 2010). We wondered whether

calpains, like annexins, could be recruited to membranes in the presence of calcium (Figure S5G). We centrifuged membranes from the post nuclear supernatant (PNS) of a cell lysate, either in the presence or absence of 1 mM Ca^{2+}. Membranes sedimented in the presence of Ca^{2+} were washed with 5 mM EGTA. High levels of annexin A1 and A2 and activated, autolyzed calpain-1 were eluted and recovered in the wash supernatant sample. In contrast, annexins and calpain-1 did not sediment along with membranes when 1 mM Ca^{2+} was not added to the PNS. Thus, calpains are also recruited to membranes in the presence of calcium Ca^{2+}, either by directly binding membrane lipids or by interacting with membrane-associated proteins.

Inhibiting annexin cleavage causes defects in repair scab secretion during membrane repair

We next tested the role of calpain-mediated cleavage in the shedding of annexin A2 scabs (Figure 6a). Calpain inhibition significantly lowered annexin $A2^+$ MV secretion. To test the specificity of the effect to annexin A2, we transfected annexin A2 KO cells with wt-annexin A2-Nluc or mt-annexin A2-Nluc (Figure 6b). SLO-treated cells secreted lower levels of vesicular mt-annexin A2 compared to wt-annexin A2 (Figure 6c). Next, we transfected annexin A2 KO cells with wt-annexin A2-mScarlet or mt-annexin A2-mScarlet and imaged rescue after laser ablation (Figure 6d, 6e). Transfection of annexin A2-mScarlet partially rescued repair scab formation. Quantification of the FM1-43-stained repair scab revealed that cells rescued with mt-annexin A2-mScarlet had a larger repair scab compared with cells rescued with wt-annexin A2-mScarlet, with some overlap in the error bars during the time course (Figure 6d). Visualization of annexin A2-mScarlet after ablation revealed that the mt-annexin $A2^+$ repair scab often had long (5 μm) filipodia-like structures extending from the repair site. In contrast, the mt-annexin $A2^+$ repair scab was smaller and more compact. We conclude annexin cleavage is an integral part of the membrane repair and shedding process.

Conclusions:

Annexin-dependent membrane repair is a two-step process

We find that calpains target annexins during plasma membrane repair, driving secretion of damaged membranes as microvesicles and propose a model of plasma membrane repair that is analogous to cutaneous wound repair (Figure 6f). After epidermal damage, blood flows into the wound and clots. Clotting is driven by fibrin cross linking and scabbing over the wound. In a second, slower process, proteases including plasmin and collagenase cut the crosslinks, and the scab eventually falls off the repaired wound (Kearney et al., 2022). During plasma membrane repair, annexins, including annexin A2, are

rapidly recruited to the plasma membrane within 45 sec of damage induced by laser ablation (Figure 2c) or SLO (Figure 5c). An annexin$^+$ membrane scab-like structure forms at the lesion site that may be visualized with the dye, FM1-43, and slows FM1-43 staining of intracellular organelles after laser ablation (Figure 2a). These "scabs" have either condensed or filipodia-like structures (Figure S2a). Because the cell simultaneously decreases in size (Video 1-2), we hypothesize that the scab is derived from lateral compression of the plasma membrane. Like fibrin, annexin A2 and other annexins may mediate this scabbing by crosslinking membranes at the wound site. *In vitro*, annexins crosslink liposomes (Figure 5i-j). Annexin A2 knockout cells lose latency to a membrane impermeable dye within 2 min of wounding with SLO (Figure 5f), a period that coincides with annexin A2 recruitment to the membrane lesion (Figure 2c). Finally, the FM1-43-stained repair scab is virtually absent in laser-damage annexin A2 knockout cells (Figure 5g, 5h). S100 proteins may promote this process by enhancing annexin recruitment (Figure 5e) and scabbing (Figure 5i-j). In a second stage, as for plasmin, calpain-1/2 cleave annexins (Figure 3a, 3c, 4a-e). Calpain cleavage of annexin A2 peaks by 1-2 min and is spatially restricted within putative repair scabs (Figure 4h). Calpain cleavage of annexin A2 dissociates aggregated liposomes *in vitro* (Figure 5i-j) and prevents S100A10 binding (Figure 5d). Calpain cleavage and dissociation promotes secretion of annexin A2 in microvesicles after SLO wounding (Figure 6a-c). However, calpain inhibition only partially blocks SLO-induced shedding, indicating other mechanisms may drive shedding from the repair site. Secretion of both perforated and closed vesicles (Figure S3b-c) peaks by 5 min and abates by 10 min (Figure 2e). Rescue of annexin A2 knockout with uncleavable annexin A2 causes a larger repair scab to form after laser wounding (Figure 6d, 6e). This descabbing process may increase the flexibility of the repair scab to facilitate budding and shedding, leading to a smaller repair scab at steady state. Because of their ability to induce strong membrane curvature, annexins form blebs (Boye et al., 2018) and lattice-like sheets *in vitro* (Lin et al., 2020). Cleavage may destabilize these structures, potentially preventing annexin overactivation.

Depending on the type of plasma membrane wound and the extent of damage, different repair machinery and mechanisms may be employed. Although we and others have visualized ectocytosis at the membrane damage site (Foltz et al., 2021; Wu et al., 2020), other mechanisms including endocytosis of damaged membranes are also reported (Stefani et al., 2024; Zhen et al., 2021). Additionally, we previously showed that late endosomes fuse with the plasma membrane during membrane repair (Williams et al., 2023), and others have observed early endosomes (Raj et al., 2023) and lysosomes (Reddy et al., 2001) fusing with the plasma membrane during membrane repair. Here, we observe that late endosome exocytosis, measured by CD63$^+$ exosome secretion, appears to be

reserved for higher levels of plasma membrane damage compared to ANXA2^{+} MV secretion (Figure 2f). We hypothesize that these diverse repair mechanisms may occur in concert to heal a plasma membrane lesion.

Whereas some reports suggest that calpains and annexins are important for pore toxin repair (Prislusky et al., 2024), other reports propose that this machinery is reserved for repair of larger lesions (Jimenez et al., 2014; Piper et al., 2020). Although our data supports that annexins and calpains are involved in repairing smaller SLO pores, this machinery may be even more important for repair of large lesions. Compared to SLO-wounding, laser ablation likely generates larger wounds and may affect integrity of the actin cytoskeleton proximal to the wound. We advise caution when directly comparing conclusions from SLO and laser-wounding experiments.

Substrate trapping reveals new targets for calpain-1/2

Using unbiased proteomics, we identified targets for calpain-1 and -2. Because calpain substrate recognition appears not to rely on primary sequence alone, computationally predicting calpain targets is challenging. Our dataset predicts hundreds of new calpain targets which may aid the development of new prediction algorithms. Although calpains were known to cleave membrane-cytoskeleton anchors during repair (Mellgren et al., 2007), we have extended the targets to include annexins A1, A2 and A6 (Figure 4i-j, Figure 4b, S4d). However, we do not exclude membrane-cytoskeleton anchor proteins as important calpain targets. When preparing the input lysate for substrate trapping, we depleted membranes and organelles by centrifuging the lysate at high speed (~100k x g). This step prevented pulldown of membranes and associated, nonspecific membrane proteins, as calpains interact with membranes in the presence of calcium (Figure S5G). However, high speed ultracentrifugation may have decreased membrane-cytoskeleton anchor protein abundance in the input lysate.

A comparison of the annexin transcripts suggest that annexin A2 may be the most abundant annexin in HCT116 cells (Figure 2b), possibly explaining why annexin A2 knockout HCT116 cells are defective in membrane scabbing (Figure 5f-h). In other cell lines, however, other annexins may be more abundant. For all tested annexins (A1, A2, and A6), calpain cleavage is predicted to terminate membrane-bridging activity. For the single annexin domain proteins like annexin A2, calpains cleave at the N-terminus (Figure 5d), preventing dimerization. For annexin A6, a tandem annexin domain protein, calpain cleaves between the annexin domains (Figure 3c, S4d). Thus, no matter the annexin, calpain cleavage should terminate the membrane-bridging activity of the annexin, potentially promoting scab breakdown. Besides annexin A1, A2, and A6, our substrate trapping experiment suggests many other annexins are also targeted by calpains (Figure 4i-j).

Annexin A2 is thought to form a “membrane repair complex” with S100A10, AHNAK, and with dysferlin in muscle cells (Rezvanpour et al., 2011). This complex may mediate calcium-dependent patching of membrane lesions. AHNAK and S100A10 were identified in our proteomic analysis of calpain targets. In muscle cells, dysferlin interacts with annexin A2 and is also directly targeted by calpain 1/2 (Redpath et al., 2014). We suggest that by targeting annexins, AHNAK and dysferlin, calpains may control membrane scabbing proteins during calcium-dependent membrane repair. Low level expression of a C-terminal truncation mutant of annexin A6, similar to the calpain-cleaved form of annexin A6, caused dominant-negative inhibition of membrane repair (Demonbreun et al., 2016; Swaggart et al., 2014). This observation supports our view that annexin cleavage destabilizes the repair cap and likely occurs after scrabbing. If calpains cleave annexin A6 prior to annexin recruitment, scrabbing/repair cap formation is inhibited.

Calpain cleavage may modulate aspects of annexin function other than cell surface scabbing. The N-terminal domain of annexins interact with other proteins directly or indirectly through S100 proteins. Annexin A2, for example, may interact with the cytoskeleton (Jaiswal et al., 2014; Prislusky et al., 2024). Calpain cleavage would terminate such an interaction. In this model, calpains-1/2 would act in accordance with their previously described function, targeting connections between the actin cytoskeleton and the plasma membrane (Dourdin et al., 2001; Mellgren et al., 2007). Both calpain activities, descabbing of annexins and detaching of the membrane from the cytoskeleton may be important for membrane repair and shedding.

Ca^{2+}-dependent production of MVs secrete annexins and annexin cleavage products

Lower levels of annexin-containing microvesicles are secreted into the culture medium by unstimulated cells (Figure 1a-c). It is tempting to speculate that some low level of membrane damage, repair and MV secretion occurs continuously. Consistent with this model, MVs are enriched with an array of Ca^{2+}-responsive proteins (Figure 1e), many of which are important for membrane repair. Also, the annexins in constitutively secreted MVs are cleaved by calpains, which requires micromolar calcium influx for activation. Such “damage” may be a consequence of the passaging of cells or the use of bovine serum which contains complement proteins capable of perforating human cells (Triglia and Linscott, 1980). Other processes such as cell death or the activation of a very high flux channel (e.g. P2X7) may elevate Ca^{2+} to levels sufficient for secretion of these vesicles (Golia et al., 2023). We suggest that these are normal processes that occur in animals and may explain the representation of MVs in all bodily fluids.

N-terminal peptides from annexins, particularly from annexin A1, mediate anti-inflammatory signaling. Annexin A1-derived peptides bind to Formyl Peptide Receptors

(FPRs) on the surface of immune cells, dampening proinflammatory signals and promoting proresolving processes such as efferocytosis (Perretti and Dalli, 2023). We propose that calpains may also generate these peptides. Once cleaved, N-terminal peptides may diffuse directly through the membrane or through vesicular disruptions. Annexin A1 N-terminal peptide intercalates into phospholipid membranes, suggesting that it may penetrate membranes (Hu et al., 2008). These peptides could then stimulate immunologically silent disposal of damaged membrane products.

Figures:

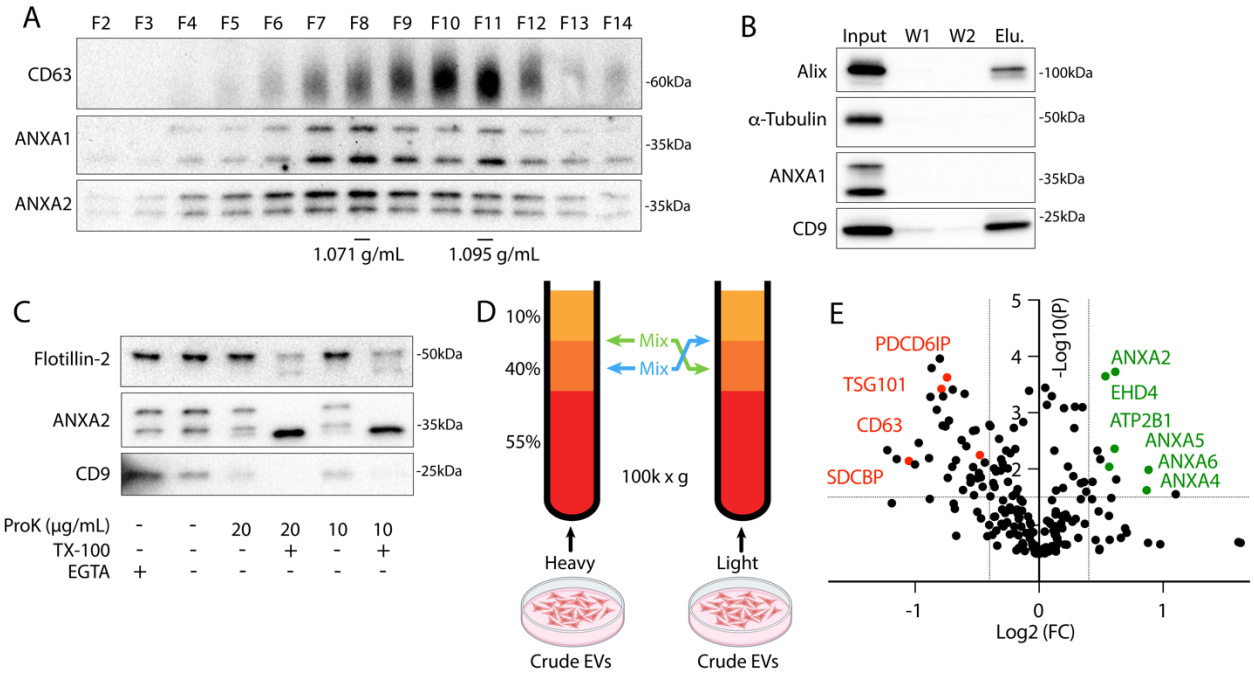

1. Annexin-containing extracellular vesicles are distinct from exosomes.

(A) Immunoblots show distribution of EV markers across an iodixanol gradient of the conditioned medium 100k × g pellet fraction. Samples were taken from low (F2-Fraction #2) to high density (F14-Fraction #14). (B) Immunoblots show depletion of annexins from exosomes after immunoprecipitation with anti-CD63 beads from the conditioned medium 100k × g pellet fraction (W1-wash #1, W2-wash #2). (C) Immunoblots show degradation of EV markers in the conditioned medium 100k × g pellet fraction after treatment with indicated combinations of proteinase K (ProK) and 0.1% Triton X-100 (TX-100). For EGTA treatments, 5 mM EGTA was introduced into the medium prior to centrifuging the conditioned medium at 100k × g. (D) Schematic illustrating the separation of EVs for quantitative proteomics using sucrose step gradients is shown. (E) Volcano plot shows enriched proteins in the high buoyant density fractions (red) relative to the low buoyant density fractions (green). P-values were calculated using a t-test.

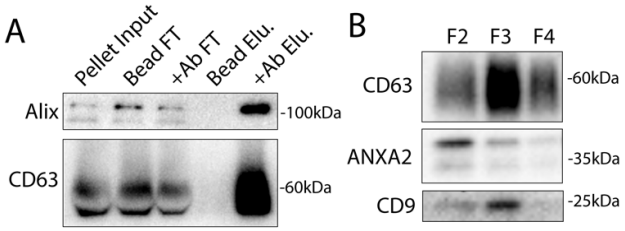

S1. Annexin-containing extracellular vesicles are distinct from exosomes.

(A) Immunoblots show enrichment of exosome proteins from the conditioned medium 100k × g pellet (Pellet Input) after immunoprecipitation with protein G beads when anti-CD63 antibody (Ab) is added to the binding reaction (FT- Binding Reaction Flow Through, Elu- Binding Reaction Elution). (B) Immunoblots show distribution of EV markers across a sucrose step gradient of the conditioned medium 100k × g pellet fraction. Samples taken from low density (F2-Fraction #2) to high density (F4-Fraction #4).

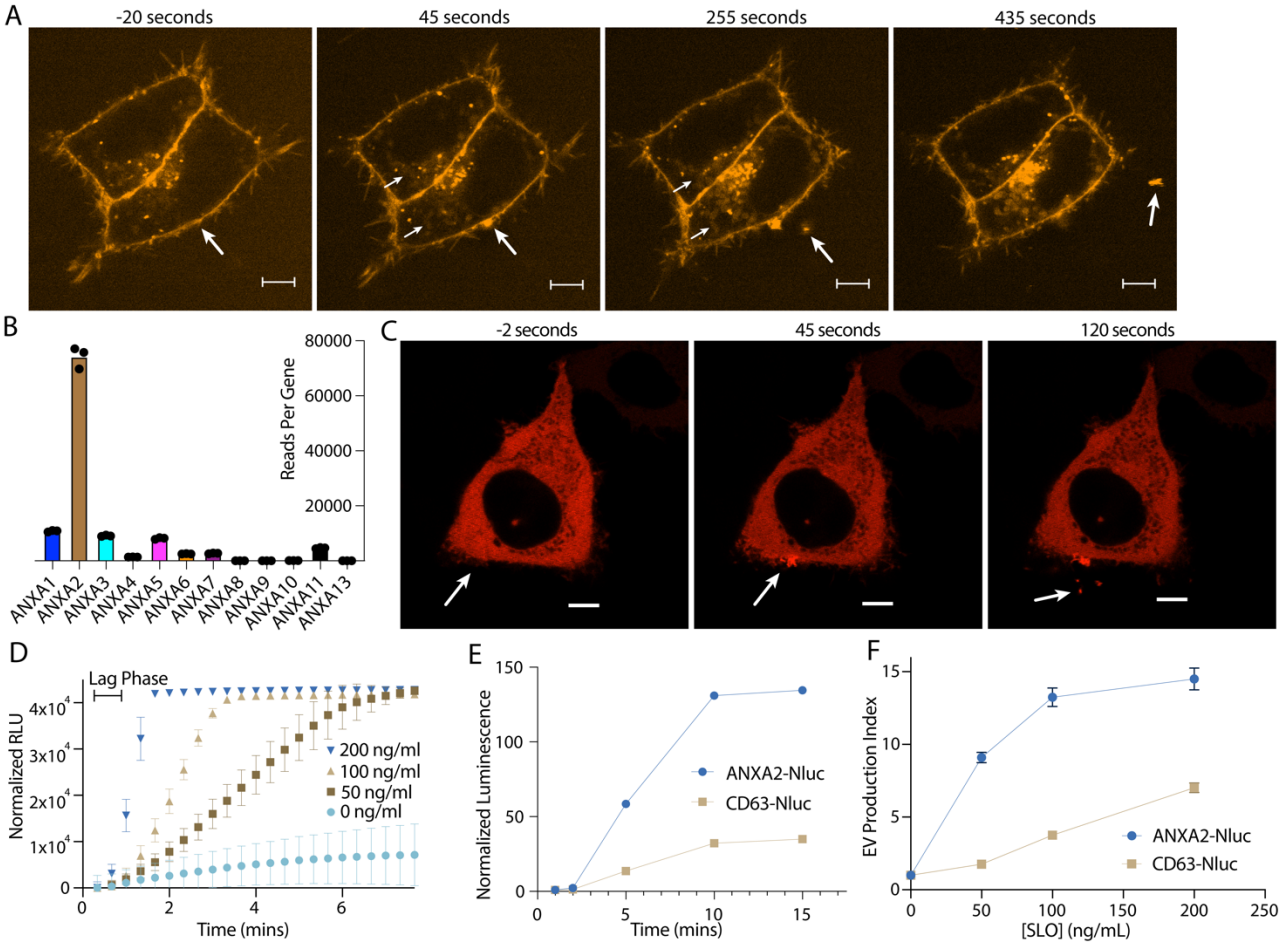

2. Annexin-containing extracellular vesicles are shed from the repair scab after plasma membrane damage.

(A) Representative confocal micrographs of FM1-43 infiltration are shown. Image times are relative to the first image taken post ablation. Large arrows in pane I and II indicate the site of ablation. Small arrows in pane II and III indicate the staining of intracellular compartments in an ablated (lower arrows) and a non-ablated cell (upper arrows). Large arrows in pane III and IV indicate extracellular vesicles. Scale Bars: 5 μm. (B) Quantification of mRNA-seq reads mapping to each annexin paralog is shown. (C) Representative confocal micrographs of ANXA2-mScarlet recruitment after ablation are shown. Image times are relative to the first image taken post ablation. White arrows in pane I and II indicate the site of ablation. Arrow in pane III indicates an extracellular vesicle. Scale Bars: 5 μm. (C) Sytox Green staining over time in the absence of extracellular Ca^{2+} after cells pretreated with the indicated concentration of SLO were rapidly heated from 4°C to 37°C. (E) Membrane-protected luminescence in medium fractions at indicated time points after ANXA2-Nluc or CD63-Nluc cells pretreated with 200 ng/μl SLO were rapidly heated from

4°C to 37°C is shown. (F) EV production index from ANXA2-Nluc or CD63-Nluc cells treated with increasing concentrations of SLO is shown.

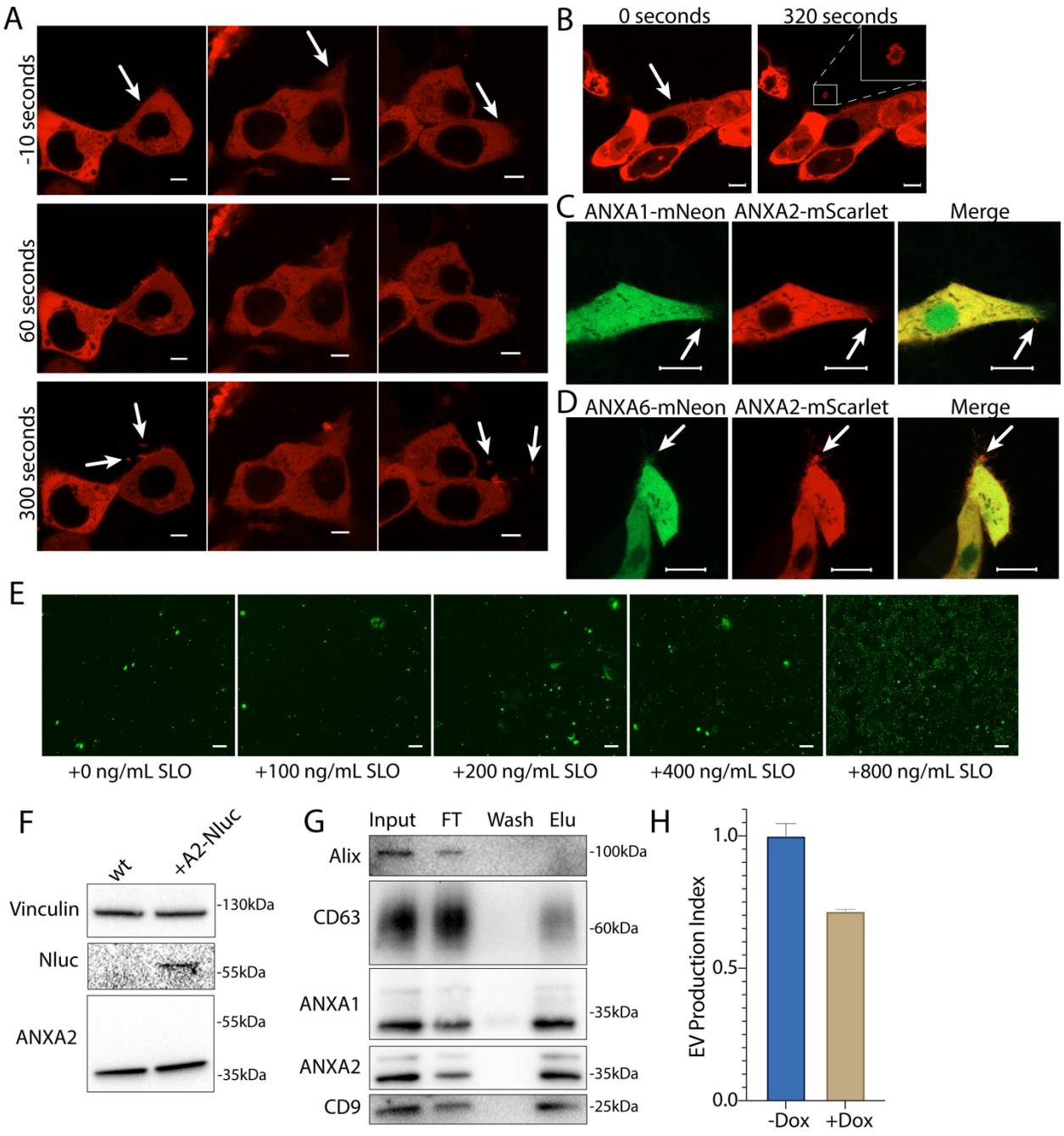

S2. Annexin-containing extracellular vesicles are shed from the repair scab after plasma membrane damage.

(A) Confocal micrographs of ANXA2-mScarlet recruitment in three laser ablation experiments are shown. Image times are relative to the first image taken post ablation. White arrows in the top panes indicate the sites of ablation. Arrows in the bottom panes indicate extracellular vesicles. Scale Bars: 5 μm. (B) Representative confocal micrographs of ANXA2-mScarlet shedding are shown. Image times are relative to the first image taken post ablation. White arrows in panel indicate the site of ablation. Scale Bars: 5 μm. (C) Representative confocal micrographs of ANXA2-mScarlet, ANXA1-mNeonGreen-expressing cells after laser ablation. Arrows indicate the ablation site. Scale Bars: 10 μm. (D) Representative confocal micrographs of ANXA2-mScarlet, ANXA6-mNeonGreen-expressing cells after laser ablation. Arrows indicate the ablation site. Scale Bars: 10 μm. (E) Representative widefield micrographs of cells stained with 1 μM Sytox Green after a treatment period with the indicated SLO concentration and recovery period. Scale Bars: 150 μm. (F) Immunoblots show expression of annexin A2-Nluc (A2-Nluc) using a low expression promoter. (G) Immunoblots show enrichment of EV markers after capture with immobilized annexin A5 from the conditioned medium 100k × g pellet fraction (FT-Flow Through, Elu-Elution). (H) EV production index from ANXA2-Nluc cells expressing mCherry-VPS4a (dominant mutant) under control of a doxycycline-inducible promoter. Cells were pretreated with 200ng/ml doxycycline (Dox) or DMSO for 6 h followed by treatment with 200 ng/ml SLO.

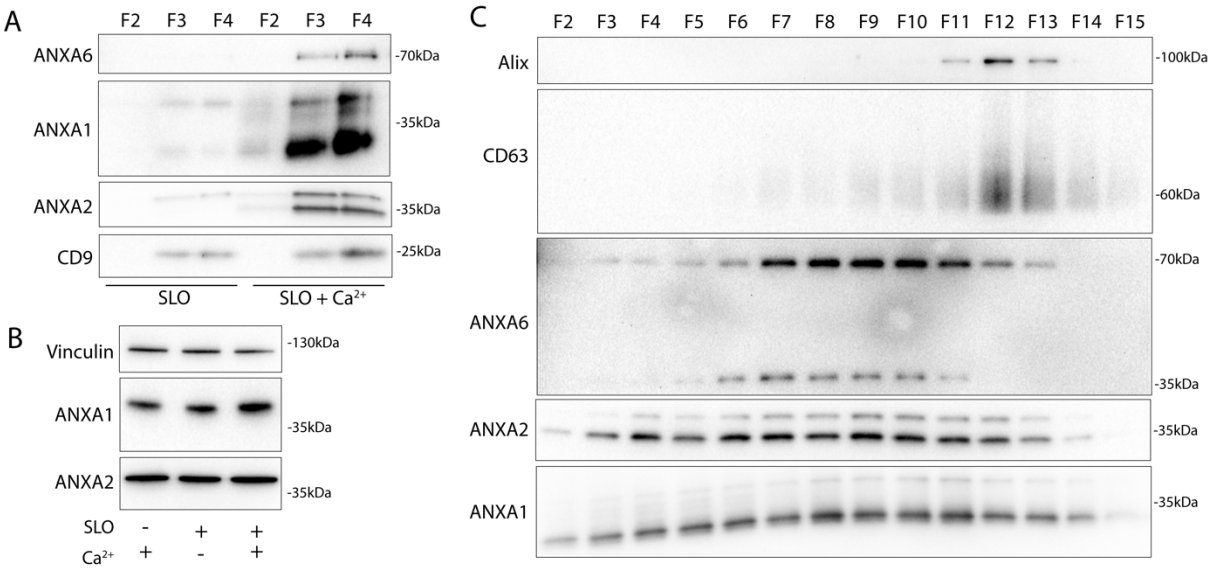

3. Annexins within extracellular vesicles are shifted in apparent molecular weight.

(A) Immunoblots of gradient fractions show enrichment of indicated EV markers after 200 ng/mL SLO treatment, with or without 1 mM Ca^{2+} in the media. F2, F3, and F4 refer to buoyant fractions of a sucrose step gradient of the conditioned medium 100k × g pellet fraction. (B) Immunoblot analysis of cell lysates after treatment with indicated combinations of 1 mM Ca^{2+} and 200 ng/mL SLO is shown. (C) Immunoblots show separation of indicated EV markers after 200 ng/mL SLO treatment. F2-F15 refer to fractions #2-15 of an iodixanol gradient of the conditioned medium 100k × g pellet fraction, moving from low to high density.

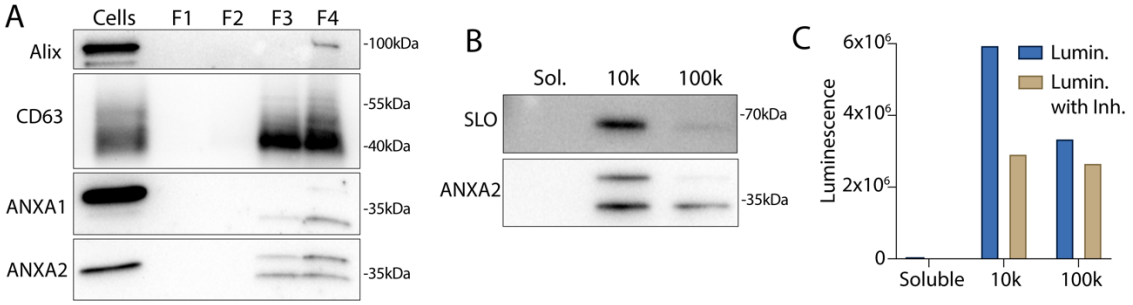

S3. Annexins within extracellular vesicles are shifted in apparent molecular weight.

(A) Immunoblots show enrichment of indicated EV markers relative to cell lysate after treatment of C2C12 myotubes with 200 ng/mL SLO. F1, F2, F3, and F4 refer to buoyant fractions of a sucrose step gradient of the conditioned medium 100k × g pellet fraction, moving from low to high density. (B) Immunoblot and (C) luminescence analysis of the 10k × g pellet fraction (10k), the 100k × g pellet fraction (100k), and the remaining soluble supernatant (Sol.) after serial centrifugation of conditioned media from ANXA2-Nluc cells treated with 200 ng/ml SLO. For each fraction, Nluc luminescence (lumin.) was measured with or without membrane impermeable Nluc inhibitor (Inh.).

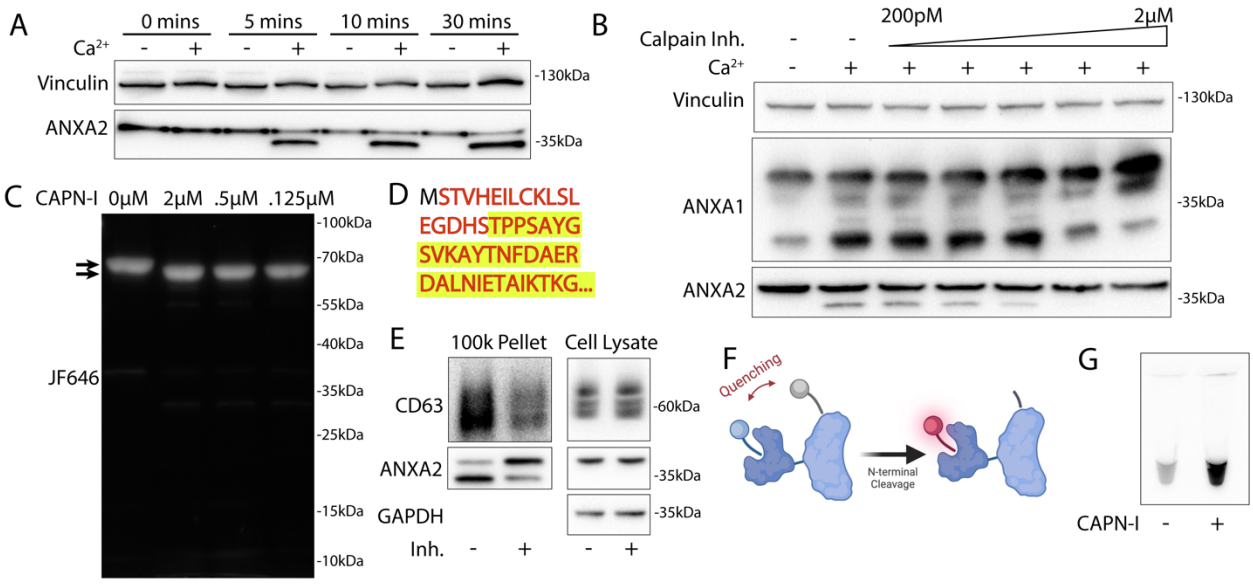

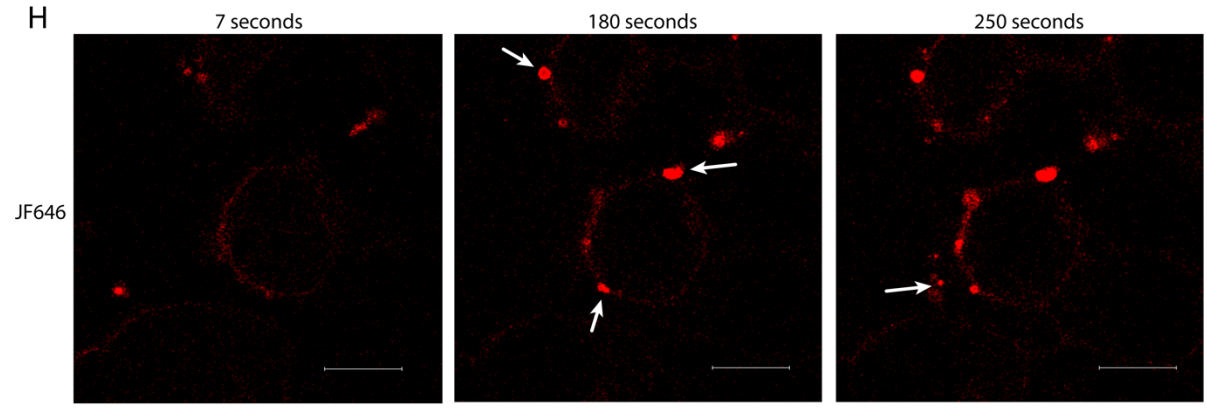

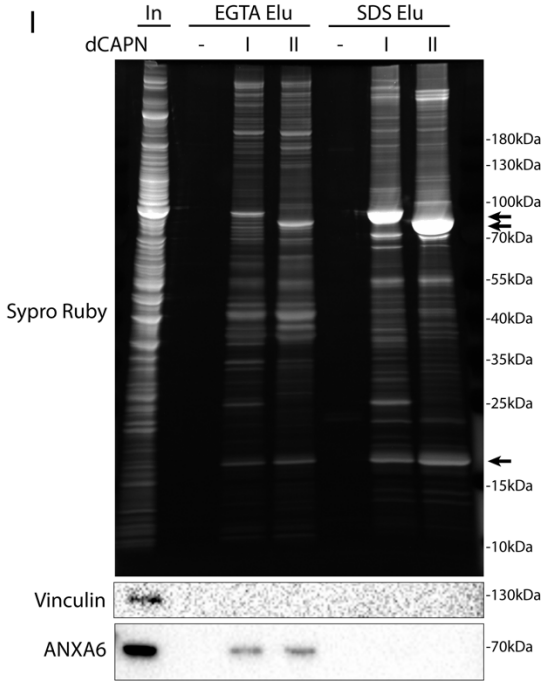

J

Gene Name	CAPN1 emPAI	CAPN2 emPAI	3xFlag emPAI
1. S100A10	3.8	2.5	0.90
2. ANXA3	3.1	5.1	0
3. CAPN1	2.7	4.7	0
4. ANXA2	2.6	3.6	0.47
5. RPS19	2.2	0.92	0.66
6. ANXA1	2.2	2.5	0
⋮	⋮	⋮	⋮
9. EPPK1	1.9	3.6	0
10. CAPNS1	1.7	2.6	0
11. PLEC	1.5	2.3	0
⋮	⋮	⋮	⋮
27. NSF	1.2	2.9	0
⋮	⋮	⋮	⋮
38. CAPN2	0.99	4.9	0
⋮	⋮	⋮	⋮
61. ANXA5	0.79	1.4	0
⋮	⋮	⋮	⋮
67. CAST	0.72	1.5	0

4. Calpain-1/2 cleave annexins which are then shed in microvesicles. (A) Immunoblot analysis of cytosol fractions after incubation with or without 1 mM Ca^{2+}. (B) Immunoblot analysis of cytosol fractions after incubation with or without 1 mM Ca^{2+}, with a range of concentrations of calpastatin domain I inhibitor (Calpain Inh.). (C) In gel fluorescence of JF646-labeled, recombinant annexin A2-Halo incubated with indicated concentration of purified, porcine calpain-1. Arrows indicate uncleaved and cleaved product. (D) Mapping of tryptic peptides to the first 50 amino acids of annexin A2. Mass spectrometry analysis of recombinant annexin A2 (red text) is compared to tryptic digest-mass spectrometry analysis of recombinant annexin A2 treated with purified, porcine calpain-1 (yellow highlight). (E) Immunoblot analysis of cell lysate and conditioned medium 100k × g pellet fraction after treating cells with 200 ng/ml SLO in the presence or absence of 10 μM calpain inhibitor, ALLN. (F) Schematic illustrating the recombinant annexin A2-Halo reporter, labeled with a 5WS maleimide quencher on the N-terminus and a JF646 halo ligand on the C-terminus. (G) JF646 fluorescence of an *in vitro* reaction containing 5 μM self-quenched annexin A2 with or without 0.5 μM porcine calpain-1. (H) Representative confocal micrographs of dequenched annexin A2-Halo-JF646 fluorescence in cells. Times are relative to the first image taken post addition of 1 mM Ca^{2+}. White arrows in pane II indicate puncta on the cell periphery. Arrow in pane III indicates an extracellular vesicle. Scale Bars: 10 μm. (I) Total protein (Sypro Ruby staining) and immunoblot analysis of substate trapping experiment, using 3xFlag (-), 3x-Flag C115S calpain-1 (dCAPN-I), or 3x-Flag C105S calpain-2 (dCAPN-II) as bait is shown. Arrows indicate calpain proteins. (J) Table listing proteins identified in EGTA elutions from 3xFlag, 3x-Flag C115S calpain-1 (dCAPN-I), or 3x-Flag C105S calpain-2 (dCAPN-II) capture experiments. Proteins are listed by Exponentially Modified Protein Abundance Index (emPAI) in the dCAPN-I elution. Keratin proteins were not included in the list.

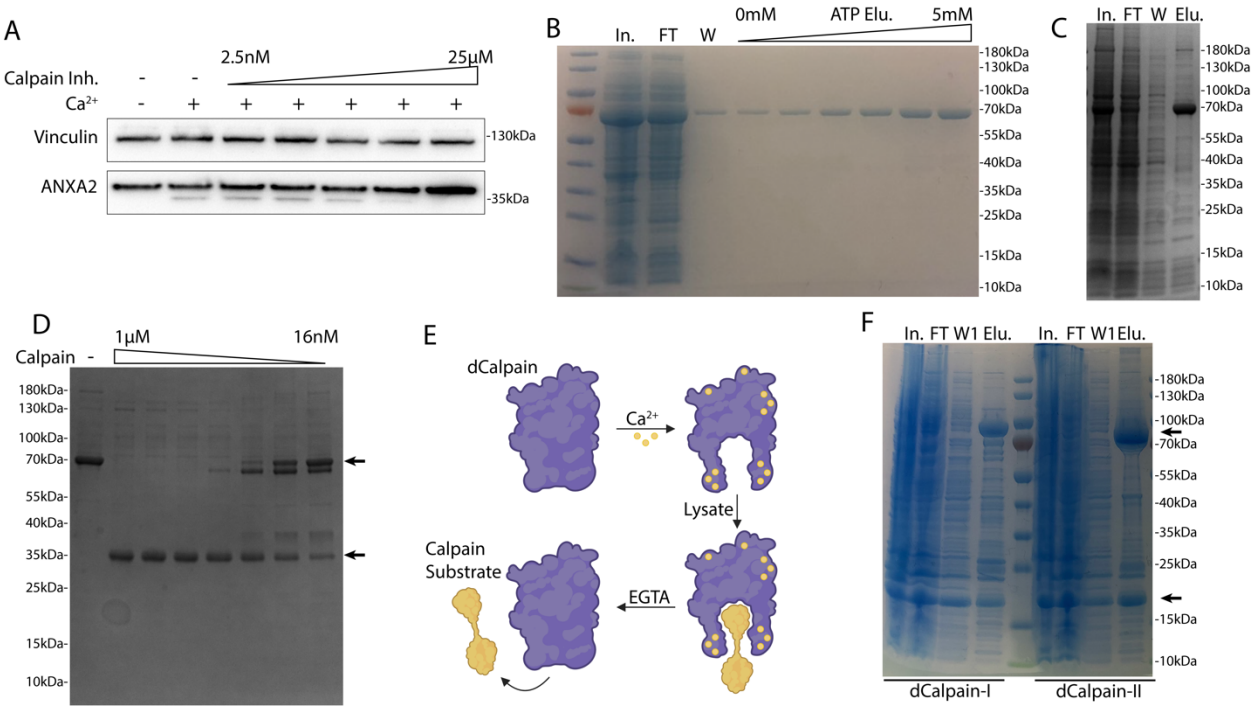

S4. Calpain-1/2 cleave annexins which are then shed in microvesicles.

(A) Immunoblot analysis of cytosol fractions after incubation with or without 1 mM Ca^{2+}, with a range of concentrations of ALLN inhibitor (Calpain Inh.). (B) Coomassie-stained gel showing purification of annexin A2-Halo from *E. coli* (In- lysate input, FT- 100k x g pellet fraction flow through, W- $CaCl_2$-containing 100k x g pellet wash, ATP Elu- elution from 100k x g pellet fraction with increasing concentrations of ATP). (C) Coomassie-stained gel showing purification of annexin A6-HA from *E. coli* (In- lysate input, FT- 100k x g pellet flow through, W- $CaCl_2$-containing 100k x g pellet wash, Elu- elution off 100k x g pellet with 10mM ATP). (D) Coomassie-stained gel showing the mobility of recombinant annexin A6-HA, incubated with a range of concentrations of purified, porcine calpain-1. Arrows indicate uncleaved and cleaved product. (E) Schematic illustrating substrate binding and elution of substrates (yellow) to catalytic cysteine-to-serine mutant calpain baits (dCAPN, purple). (F) Coomassie-stained gel showing initial, his-tag purification of CAPN1[C115S]-3xFlag-6xHis (dCalpain-I) and CAPN2[C105S]-3xFlag-6xHis (dCalpain-II) in complex with CAPNS1(86-268) from *E. coli* (In- lysate input, FT- bead flow through, W- bead wash, Elu- elution from Ni^{2+} with 300 mM imidazole). Arrows indicate calpain proteins.

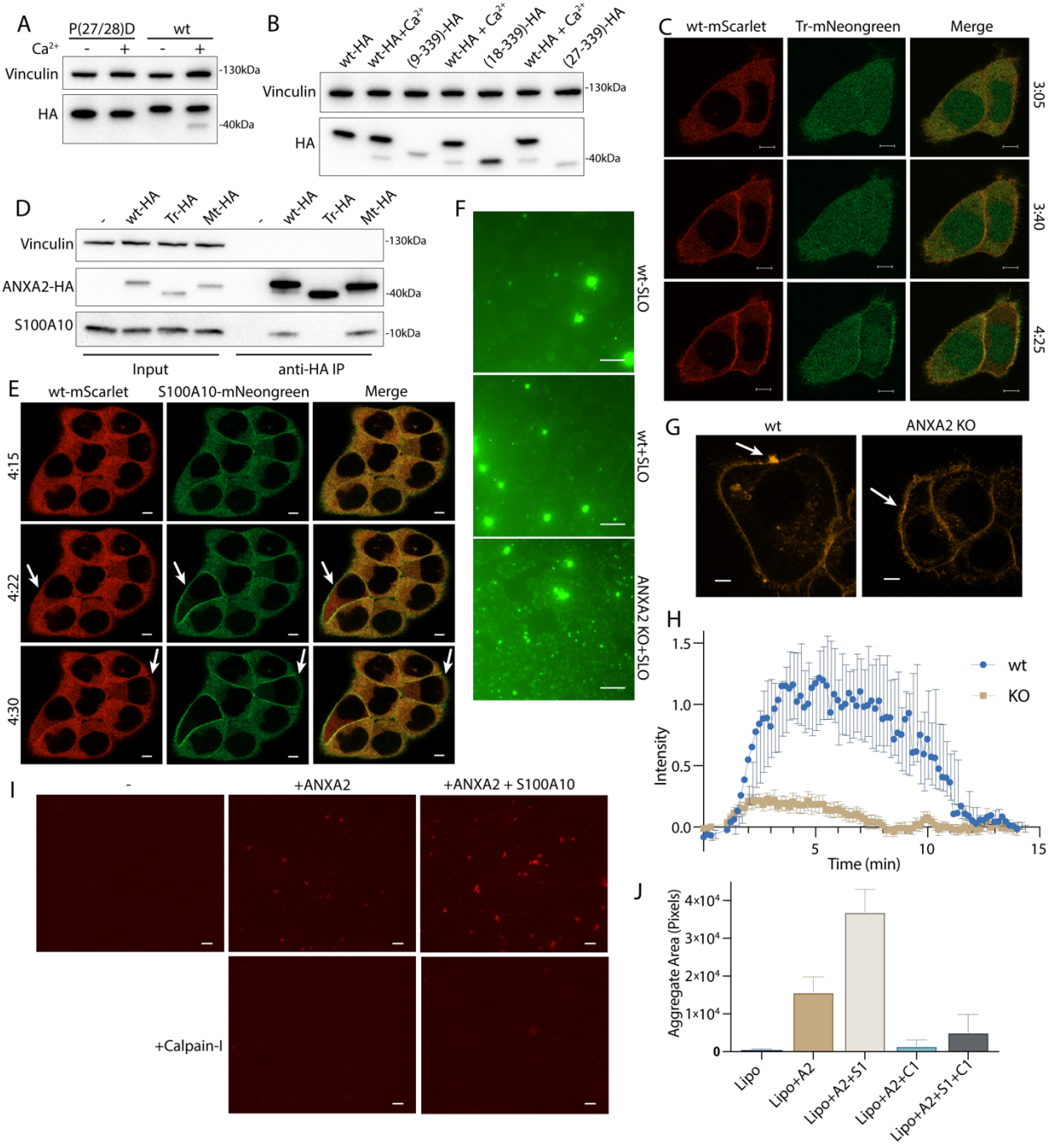

5. Calpain cleavage attenuates the membrane binding and scabbing activity of annexin A2.

(A) Immunoblot analysis of lysates from cells expressing wildtype ANXA2-HA or ANXA2[P27D, P28D]-HA. Ca^{2+} (1 mM) was added to lysis buffer where indicated. (B) Immunoblot analysis of lysates from cells expressing wildtype ANXA2-HA or ANXA2-HA with the indicated N-terminal truncations. Ca^{2+} (1 mM) was added to lysis buffer where indicated. (C) Representative confocal micrographs of ANXA2-mScarlet (wt-mScarlet),

ANXA2(18-339)-mNeonGreen (Tr-mNeonGreen)-expressing cells. Image times are relative to the addition of 400 ng/ml SLO. Scale Bars: 5 μm. (D) Immunoblot analysis of lysates and anti-HA immunoprecipitation elutions from cells expressing wildtype ANXA2-HA (wt-HA), ANXA2(18-339)-HA (Tr-HA), ANXA2[P27D, P28D]-HA (Mt-HA), or no HA construct. (E) Representative confocal micrographs of ANXA2-mScarlet (wt-mScarlet), S100A10-mNeonGreen-expressing cells. Image times are relative to the addition of 400 ng/ml SLO. Arrows indicate cells with annexin A2 and S100A10 translocating to the membrane. Scale Bars: 5 μm. (F) Representative widefield micrographs of wildtype or annexin A2 knockout cells, with 2.5 μM Sytox Green added for 6 min. SLO (200 ng/ml) was added with Sytox Green in the indicated panels. Scale Bars: 100 μm. (G) Representative confocal micrographs of FM1-43 stained (2.5 μM) wildtype or annexin A2 knockout cells, 100 sec after laser ablation. Scale Bars: 5 μm. (H) Quantification over time of the repair scab intensity from FM1-43 stained (2.5 μM) wildtype or annexin A2 knockout cells. 6 cells were ablated for each condition. (I) Representative widefield micrographs and aggregate size quantification (J) of Texas Red-labeled 200 nm liposomes mixed with the indicated combinations of 300 nM annexin A2 (A2), annexin A2-S100A10 (A2+S1), or Calpain-1 (C1). Scale Bars: 50 μm.

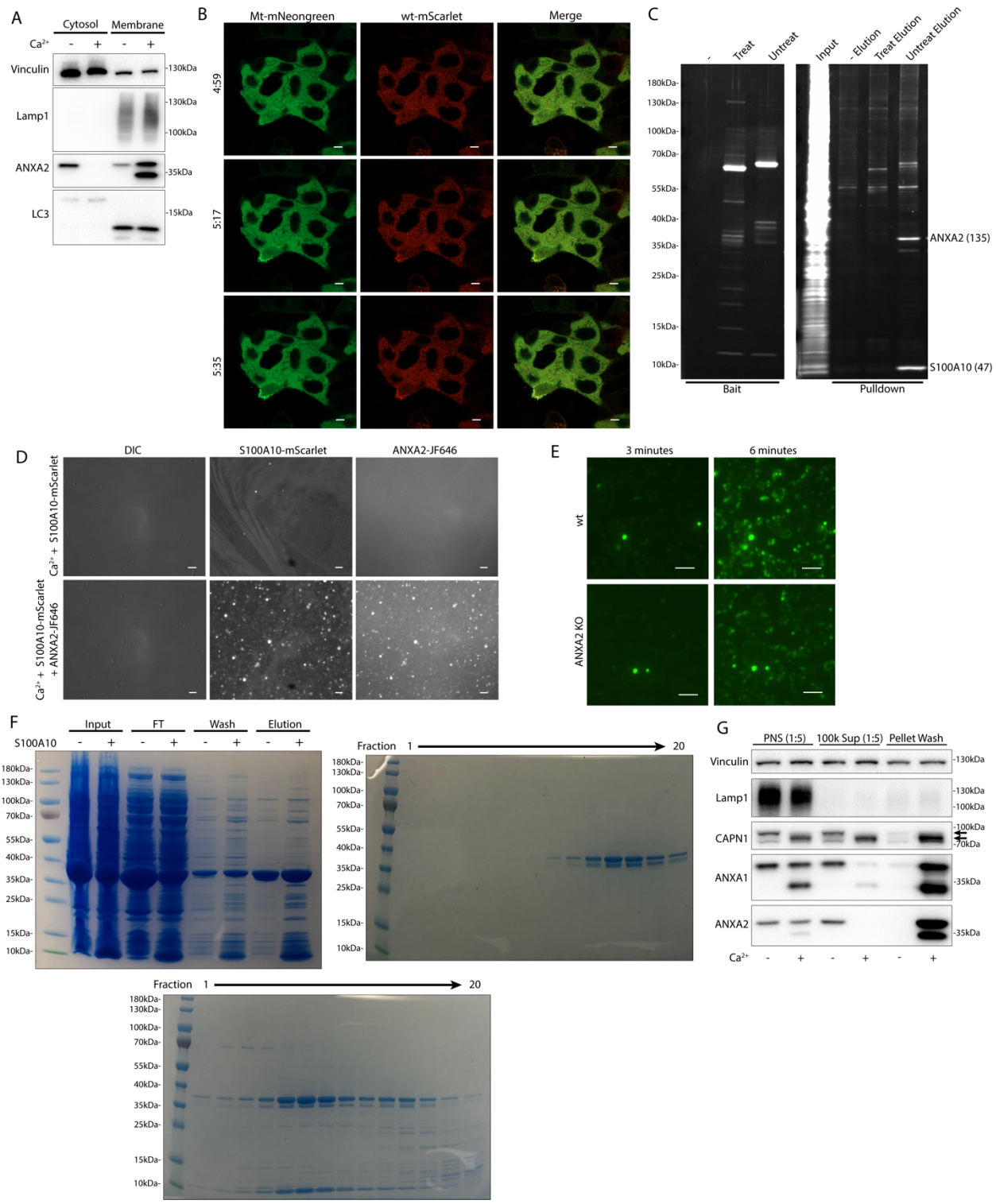

S5. Calpain cleavage attenuates the membrane binding and scabbing activity of annexin A2.

(A) Immunoblot analysis of cytosol and membrane factions, with or without 1 mM Ca^{2+} added prior to fractionation. (B) Representative confocal micrographs of ANXA2-mScarlet (wt-mScarlet), ANXA2[P27D, P28D]-mNeonGreen (Mt-mScarlet)-expressing cells. Image times are relative to the addition of 400 ng/mL SLO. Scale Bars: 5 μm. (C) Total protein (Sypro Ruby staining) analysis of HaloTag "pulldown" is shown, using no bait (-), porcine calpain-1-treated annexin A2-haloTag bait (Treat), or untreated annexin A2-haloTag bait (Untreat). Proteins are labeled with spectral counts, in parentheses, from gel excision-mass spectrometry. (D) Representative widefield micrographs of purified S100A10-mScarlet (1 μM) binding to GUVs with or without annexin A2-HaloTag-JF646 (1 μM). Scale Bars: 50 μm. (E) Representative widefield micrographs of wildtype or annexin A2 KO cells treated with 200 ng/ml SLO and 2.5 μM Sytox Green without Ca^{2+} in the media. Scale Bars: 100 μm. (F) Coomassie-stained gels showing purification of annexin A2 or annexin A2-S100A10 complex from *E. coli*. Panel I shows the initial purification by eluting annexin A2 from the *E. coli* lysate pellet fraction in a Ca^{2+}-dependent manner (Input- lysate input, FT-100k x g pellet flow through, Wash- $CaCl_2$-containing 100k x g pellet wash, Elution- 10mM ATP elution from 100k x g pellet fraction). Where indicated lysate from S100A10-expressing *E. coli* was mixed 1:1 with annexin A2 *E. coli* lysate before purification. Panel II and III show size exclusion chromatography fractions of annexin A2 and annexin A2-S100A10 complex, respectively. (G) Immunoblot analysis shows mechanically lysed cells sequentially fractionated into post nuclear supernatant (PNS, diluted 1:5 before loading), 100k x g centrifuged PNS supernatant (100k Sup, diluted 1:5 before loading), and 100k x g pellet washed with 5 mM EGTA and recentrifuged (Pellet Wash). Samples where 1 mM Ca^{2+} was initially added to PNS are indicated. Arrows indicate uncleaved and autolyzed CAPN1.

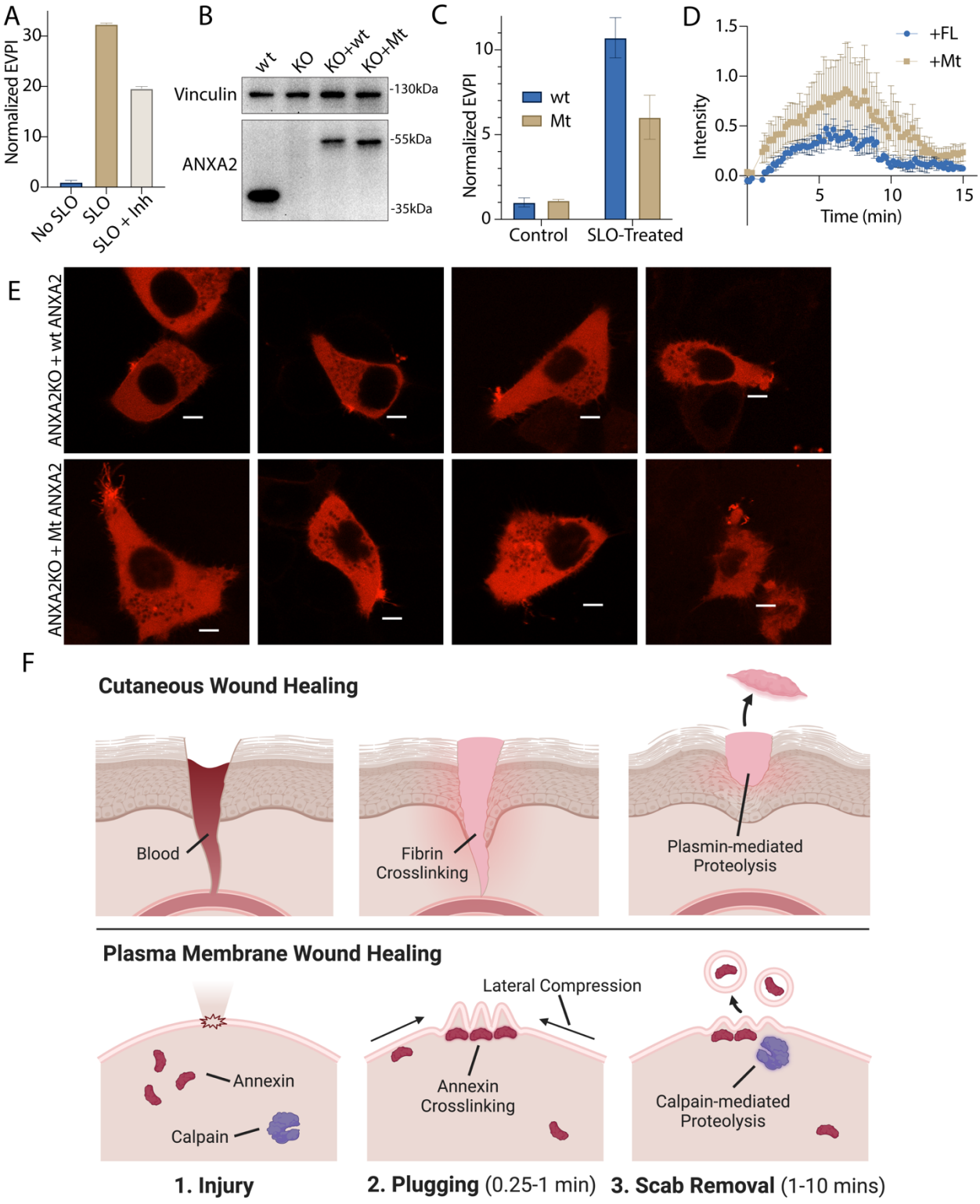

6. Inhibition of annexin A2 cleavage decreases annexin A2^{+} microvesicle secretion during membrane repair.

(A) EV production index from ANXA2-Nluc cells treated with the indicated combinations of 200ng/ml SLO and 20 μM calpain Inhibitor, ALLN. (B) Immunoblot analysis of lysates from wildtype cells (wt), annexin A2 knockout cells (KO), and annexin A2 knockout cells expressing wildtype annexin A2-Nluc (KO + wt) or ANXA2[P27D, P28D]-Nluc (KO + Mt). (C) EV production index from wildtype ANXA2-Nluc (wt) or ANXA2[P27D, P28D]-Nluc (Mt) cells treated with or without SLO. (D) Quantification over time of the repair scab intensity from FM1-43 stained (2.5 μM) annexin A2 knockout cells rescued with ANXA2-mScarlet (wt) or ANXA2[P27D, P28D]-mScarlet (Mt). Cells (6) were ablated for each condition. (E) Confocal micrographs of 8 laser ablated annexin A2 knockout cells rescued with either wild-type ANXA2-mScarlet (wt) or ANXA2[P27D, P28D]-mScarlet (Mt). Images are 2 min, 30 sec after ablation. Scale Bars: 5 μm. (F) Schematic depicting the current model of plasma membrane repair and annexin^{+} MV secretion.

Chapter 3: The Mitochondrial Calcium Uniporter and the Annexin-binding protein, Sorcin, Coordinate ESCRT Recruitment during Plasma Membrane Repair

Introduction: The plasma membrane is the outer boundary of the metazoan cell, and its integrity is required to maintain cellular homeostasis. The plasma membrane may sustain damage during cell contraction, infection, migration, metastasis, and after fluid shear stress. Failure of membrane repair machinery results in human diseases like muscular dystrophies. The cellular machinery that repairs the membrane after damage is incompletely understood. The mitochondrial calcium uniporter (MCU) is a channel on the inner mitochondrial membrane that is required for mitochondrial calcium uptake. Previously, the MCU was proposed to assist in plasma membrane repair by generation of mitochondrial reactive oxygen species. It is unknown if the MCU promotes plasma membrane repair by other mechanism.

We perform genome wide CRISPRi screening to identify novel mediators of plasma membrane repair in metastatic cancer cells. We identify two novel repair proteins EMRE and Sorcin. EMRE is a membrane of the MCU complex. Although other components of the MCU were previously implicated in membrane repair, the mechanism was proposed to involve generation of mitochondrial reactive oxygen species. Here we show that EMRE and the MCU prevent cytosolic calcium overload during membrane repair.

Materials and Methods

Lentivirus production and transduction

For lentiviral expression of shRNA or mRNA, HEK293T cells at 40% confluence within a 6-well plate were transfected with 165 ng of pMD2.G, 1.35 µg of psPAX2, and 1.5 µg of a pLJM1 or pLIX403 plasmid using the TransIT-LT1 Transfection Reagent (Mirus Bio) as per the manufacturer's protocol. At 48 h post-transfection, 1 ml of fresh DMEM supplemented with 10% FBS was added to each well. The lentivirus-containing medium was harvested 72 h post-transfection by filtration through a 0.45 µm polyethersulfone (PES) filter (VWR Sciences). The filtered lentivirus was distributed in aliquots, snap-frozen in liquid nitrogen, and stored at –80°C. For lentiviral transductions, we infected MDA-MB-231 cells with filtered lentivirus in the presence of 8 µg/ml polybrene for 24 h, and the medium was replaced. HCT116 cells were selected using 0.5 µg/ml puromycin for 5 days. Gene expression was assessed by immunoblot analysis.

For lentiviral expression of the CRISPRi library, HEK293T cells at 40% confluence within two 15 cm plates were each transfected with 1 µg of pMD2.G, 7 µg of psPAX2, and 8 µg of dual CRISPRi library (Addgene 187246) using 48 µl TransIT-LT1 Transfection Reagent (Mirus Bio) as per the manufacturer's protocol. At 48 h post-transfection, 10 ml of fresh DMEM

supplemented with 10% FBS was added to each plate. The lentivirus-containing medium was harvested 72 h post-transfection by filtration through a 0.45 µm polyethersulfone (PES) filter (VWR Sciences). The filtered lentivirus was distributed in aliquots, snap-frozen in liquid nitrogen, and stored at –80°C. For lentiviral transductions, we infected 5 x 15 cm plates of an MDA-MB-231 clone expressing dCas9-Zim3 with filtered lentivirus in the presence of 8 µg/ml polybrene for 24 h, and the medium was replaced. dCas9-Zim3 cells were selected using 0.5 µg/ml puromycin for 8 days. The virus concentration used resulted in 20% confluence after selection.

CRISPRi Screening

After selection, 9 plates of 80% confluent CRISPRi library cells were washed once with 10 ml PBS each and dissociated from the plate with 5 ml Accutase. The cell slurry was pooled in a 50 mL conical, and cells were spun down at 300 x g for 4 minutes. Cells were reuspended in 12 ml of TBS, split equally into 3 tubes, and brought up to 2 mil cells/ml in each tube. Equal volume of TBS + Ca^{2+} (2mM), TBS + Ca^{2+} + PFO (3.125 ng/mL), or TBS + PFO (0.78 ng/mL PFO) were added to each tube. Cells were mixed by gentle inversion and incubate at 37°C for 20 minutes. Cells were spun back down at 300 x g for 4 minutes and resuspend in 12 mL media. Cell slurry was split equally into 6 x 15 cm plate for each condition. 36 hours later, cells (~25 million for each condition) were collected with accutase and stored at -80°C.

Genomic DNA Isolation

Cells for each condition were lysed with 5ml lysis buffer (20 mM Tris-Cl (pH 8.0) 10 mM EDTA, 100 mM NaCl, 0.5 % (w/v) SDS) in a 15ml falcon tube. An equal volume of phenol:chloroform:isoamyl alcohol (25:24:1) pH 8 was added and shaken till an emulsion formed. The emulsion was incubated for 5 min. Tubes were spun at 5k x g for 1 hour. The aqueous, upper phase was removed (~4.5 ml) into a 15 ml falcon tube and 2.5 ml TE buffer was added to the phenol:chloroform:isoamyl alcohol phase and DNA was reextracted. 7 ml of chloroform was added to the 7.5 ml of removed aqueous phase and shaken till an emulsion formed. The emulsion was incubated for 5 min. Tubes were spun at 5k x g for 1 h. The aqueous, upper phase was removed (~7 ml) into a 50 ml falcon tube and 2.5 ml TE buffer was added to the chloroform phase and DNA was reextracted. 1 ml of 3M Sodium Acetate, pH 5.2 was added to the aqueous phase. 20ml of EtOH was added to the ~10ml of aqueous phase and mixed. Samples were stored overnight at 4°C. Tubes were spun at 5k x g at 4 degrees for 1 h. All but 1 ml of supernatant was removed, and the pellet resuspended in the remaining supernatant. Pellet and remaining supernatant were transferred to a 1.5ml tube. The pellet was resedimented at 20k x g at 4°C for 5 minutes. The supernatant was carefully removed, and pellet resuspended in 1 ml 70% EtOH. The pellet was resedimented

at 15k x g at RT for 5 minutes. The supernatant was carefully removed, and pellet resuspended in 1 ml 70% EtOH. The pellet was resedimented at 15k x g at RT for 5 minutes. The supernatant was carefully removed, and pellet allow to air dry for 10 minutes. The pellet was resuspended in 1x 0.75ml RNase ONE (promega) buffer. 3.75 µl RNase ONE (promega) and RNase A (Thermo) was added to the reaction and incubated for 6 hours at 37°C. 75 µl of 3M Sodium Acetate, pH 5.2 was added to the reaction. 1.5 ml of EtOH was added to the ~0.75 ml of aqueous phase and mixed. Samples were stored overnight at 4 degrees. Tubes were spun at 5k x g at 4°C for 1 h. All but 1 ml of supernatant was removed, and the pellet resuspended in the remaining supernatant. Pellet and remaining supernatant were transferred to a 1.5 ml tube. The pellet was resedimented at 20k x g at 4°C for 5 min. The supernatant was carefully removed, and pellet resuspended in 1 mL 70% EtOH. The pellet was resedimented at 15k x g at RT for 5 min. The supernatant was carefully removed, and pellet resuspended in 1 ml 70% EtOH. The pellet was resedimented at 15k x g at RT for 5 min. The supernatant was carefully removed, and pellet allow to air dry for 10 min. The pellet was resuspended in 1x 0.75 ml 2.5 mM Tris pH 8.

Library Preparation and Sequencing

A PCR reaction was set up with the following components: 20 µl oJR441 reverse primer (100 µM, CAAGCAGAAGACGGCATACGAGATGCGGCCGGCTGTTTCCAGCTTAGCTCTTAAA), 20 µl indexed forward primer (100 uM, AATGATACGGCGACCACCGAGATCTACACnnnnnnnnCGCGTATCCCTTGGAGAACCACC), 1 ml NEBNext Ultra II Q5 MasterMix, and 200 µg sample gDNA. Each PCR was brought up to 2 mL with dH2O and distributed into 100 µl PCR reactions. The following PCR amplification program was used: (1) 98 ºC, 30 sec; (2) 98 ºC, 10 sec; (3) 63 ºC, 75 s; steps 2-3 repeated 21x; 72 ºC, 5 min. A 0.5-0.65X double SPRI (Beckman Coulter) purification was used to purify the PCR amplicon. Sequencing was performed using a NextSeq P2 100PE (400 mil PE reads) with custom sequencing (Read 1: CGCGTATCCCTTGGAGAACCACCTTGTTGG, Read 2: GCGGCCGGCTGTTTCCAGCTTAGCTCTTAAAC) and indexing primers (Index: CCAACAAGGTGGTTCTCCAAGGGATACGCG).

Cell Viability Assays

Cells were plated two days before in a 24 well plate and grown to 70% confluence. Cells were treated +/- 100 ng/ml PFO in 200 uL Opti-mem for 30 minutes. Media was replaced with 200 µl fresh DMEM + 10% FBS and cells were allowed to recover for 1 h.

For MTT assays, 200 µl DMEM + 10% FBS + 1 mg/mL MTT (3-(4,5-dimethylthiazol-2-yl)-2,5-diphenyltetrazolium bromide) was added to the cells and allowed to incubate for 1 h. The

media was removed and replaced with 200 µl DMSO, and vigorously resuspended. Absorbance was read at 570 nm with a 630 nm reference.

For LDH assays, recover media was aspirated and replaced with 200 µl lysis buffer from the Pierce LDH Cytotoxicity Assay Kit. Lysate was thoroughly mixed by pipetting up and down. 10 µl of lysate was mixed with 40 µl fresh lysis buffer and 50 µl Reaction Mix from the Pierce LDH Cytotoxicity Assay Kit and mixed. The plate was incubated at room temperature for 30 minutes protected from light. The absorbance at 490 nm and 680 nm was measured. To determine LDH activity, the 680 nm absorbance value (background signal from instrument) was subtracted from the 490 nm absorbance.

Results

A genome-wide CRISPRi screen identifies novel mediators of membrane repair

We sought to identify mediators of plasma membrane repair by performing a knockdown CRISPRi survival screen after treatment with the bacterial pore forming toxin, Perfringolysin O (PFO). However, previous survival screens after pore toxin treatment generally do not identify membrane repair factors (Liu et al., 2020; Virreira Winter et al., 2016). Instead, these screens primarily identify factors that affect toxin binding and pore formation on the plasma membrane. Addition of a counter screen might allow identification of bona fide plasma membrane repair factors.

Influx of extracellular calcium upon damage is required for plasma membrane repair. Indeed, ~5-fold less PFO is required to kill MDA-MB-231 (MM231) cells in the absence of extracellular Ca^{2+} (Figure 1a). We devised a genome wide CRISPRi survival screen based on this sensitization (Figure 1b). Library-transduced MM231 cells were treated without PFO or a dose of PFO that achieved 75% killing efficacy in the presence or absence of Ca^{2+} (black arrows, Figure 1a). Following cell collection and deep sequencing of PCR-amplified barcodes, guide enrichment was compared between conditions.

As expected, when comparing the no treatment condition with the high PFO with Ca^{2+} treatment condition, the most enriched knockdown guides appeared to be involved in PFO binding to the plasma membrane (Figure 1c). PFO is part of the Cholesterol-dependent Cytolysin (CDC) family that recognizes cholesterol on the outer leaflet of animal cell membranes. The top enriched knockdown guides were all involved with cholesterol uptake and trafficking to the outer leaflet of the plasma membrane.

When comparing the low PFO without Ca^{2+} condition with the high PFO with Ca^{2+} treatment condition, we no longer enriched cholesterol trafficking knockdown guides (Figure 1d). Instead, several Ca^{2+}-binding proteins were enriched. The top hit after ranking genes by the ratio of PFO without Ca^{2+} to PFO with Ca^{2+} was annexin A11, a gene recently shown to be

required for ESCRT recruitment during plasma membrane repair. Also, in the top 10 hits (Figure 1d, inset) was S100A10, a protein we previously showed was recruited to plasma membrane lesions with annexin A2, although this complex is apparently cleaved by calpains during the repair process.

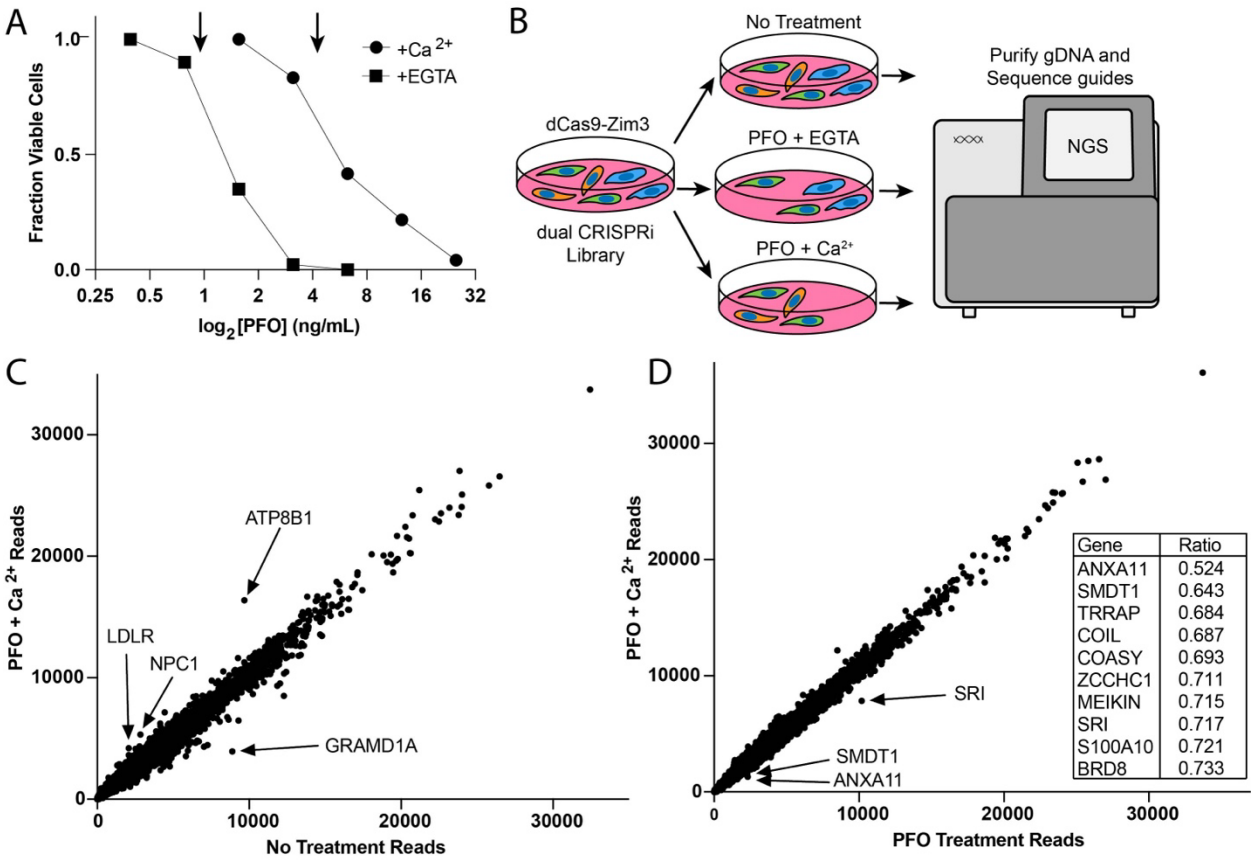

We also found Ca^{2+}-binding proteins that have not been previously implicated in membrane repair. Sorcin (SRI) is a homologue of ALG-2, a protein that is required for ESCRT recruitment after lysosome membrane damage. Sorcin is also known to bind annexin A11, suggesting it may link annexins to ESCRT recruitment. SMDT1, also known as EMRE, was the second strongest hit on our screen after annexin A11. EMRE is a required subunit of the MCU. Although EMRE has not been directly implicated in membrane repair, we note that other subunits of the MCU have been previously implicated. Remarkably, mutations in EMRE were recently shown to cause limb-girdle muscular dystrophy, a disease that may be associated with plasma membrane repair failure in muscle (Bulthuis et al., 2023). Thus, we wanted to understand how EMRE and the MCU is involved in membrane repair.

EMRE depletion causes Ca^{2+} overload during membrane repair

Expression of shRNAs targeting EMRE depleted EMRE mRNA nearly 16-fold relative to β-actin mRNA (Figure 2a). EMRE-depleted cells appeared healthy and grew at the same rate as wildtype cells. Using an MTT viability assay, we assessed sensitization of EMRE knockdown cells to plasma membrane damage (Figure 2b). ~Half as many EMRE knockdown cells survived 100 ng/ml PFO treatment as nontargeting GFP knockdown cells. As the MTT assay measures the activity of cytosolic oxidases, impaired mitochondrial activity may affect viability measurements. However, MTT measurements did not appear to be an artifact of altered metabolic activity, as DIC images showed significantly fewer

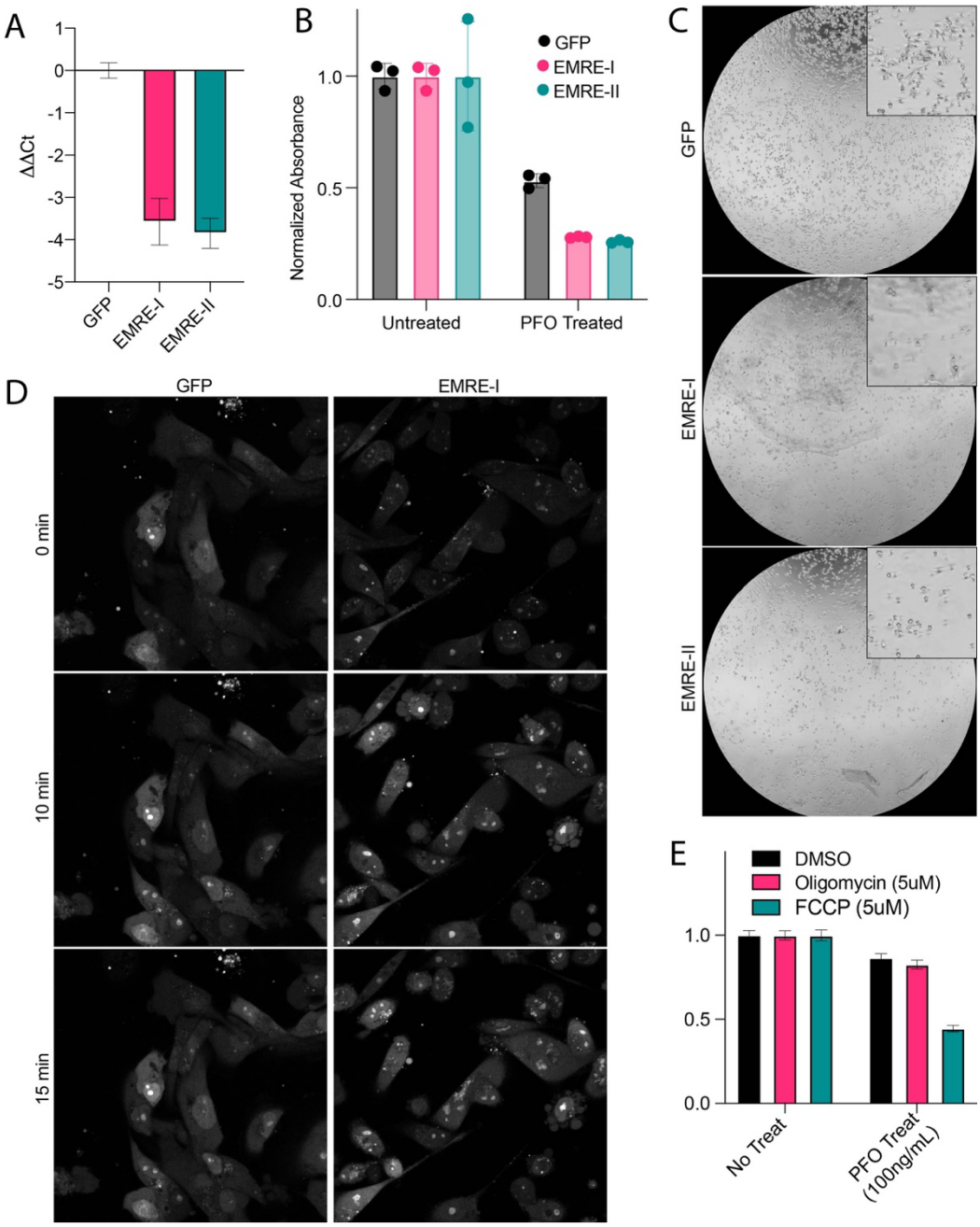

surviving EMRE knockdown cells compared to nontargeting GFP knockdown cells (Figure 2c).

We noticed that PFO-treated EMRE knockdown cells had a rounded morphology. Ca^{2+} overload is known to cause cell rounding by uncontrolled myosin contractions. After loading cells with the Ca^{2+} sensitive dye, Rhod-2, we observed cells after PFO treatment (Figure 2d). We noticed significant increases in cytosolic Ca^{2+} in EMRE-depleted cells. As cytosolic Ca^{2+} increased, several cells contracted and started blebbing. In cells expressing nontargeting GFP shRNA, cytosolic Ca^{2+} increased modestly, but then decreased after.

Next, we tested whether acute inhibition of mitochondrial Ca^{2+} uptake independent of the MCU might sensitize cells to PFO treatment. The mitochondrial ATP synthase produces ATP by harnessing the proton gradient across the inner mitochondrial membrane. This gradient also drives Ca^{2+} into the inner membrane space at concentrations up 200 μM. Equilibration of the proton gradient using the protonophore, FCCP, significantly sensitized cells to PFO (Figure 2e), as measured by LDH assays. This effect was independent of ATP production, as direct inhibition of the ATPase with oligomycin did not significantly sensitize cells to PFO.

Our data suggests that mitochondrial calcium uptake prevents cytosolic Ca^{2+} overload during membrane repair. However, our data could also be explained by increased Ca^{2+} influx due to failure of mitochondrial-mediated membrane repair, in line with previous models. To test these models, we used the ionophore, ionomycin, to specifically deliver micromolar levels of Ca^{2+}, independently of membrane damage (Figure 3a). Independently, neither ionomycin nor FCCP caused significant cell death. Combined treatment however, led to significant cell death.

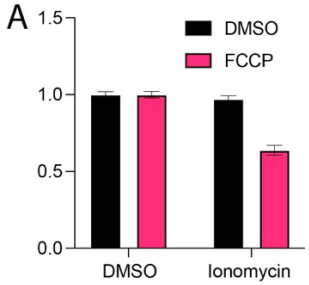

Conclusion

Taken together, our data suggests that mitochondria act as a cellular sink for cytosolic Ca^{2+} during membrane repair. The Ca^{2+} sink model has been previously proposed to dampen Ca^{2+} transients during signaling events like heart muscle contraction. Our data suggests that mitochondrial Ca^{2+} uptake also prevents cell death by cytosolic Ca^{2+} overload.

References

Chapter 1

S. O. Shan, P. Walter, Co-translational protein targeting by the signal recognition particle. *FEBS Lett.* **579**, 921–926 (2005).

E. Park, T. A. Rapoport, Mechanisms of Sec61SecY-mediated protein translocation across membranes. *Annu. Rev. Biophys.* **41**, 21–40 (2012).

G. Zanetti, K. B. Pahuja, S. Studer, S. Shim, R. Schekman, COPII and the regulation of protein sorting in mammals. *Nat. Cell Biol.* **14**, 221 (2012).

V. Malhotra, Unconventional protein secretion: An evolving mechanism. *EMBO J.* **32**, 1660–1664 (2013).

M. Zhang, *et al.*, A Translocation Pathway for Vesicle-Mediated Unconventional Protein Secretion. *Cell* **181**, 637-652.e15 (2020).

M. Colombo, G. Raposo, C. Théry, Biogenesis, secretion, and intercellular interactions of exosomes and other extracellular vesicles. *Annu. Rev. Cell Dev. Biol.* **30**, 255–289 (2014).

K. O'Brien, K. Breyne, S. Ughetto, L. C. Laurent, X. O. Breakefield, RNA delivery by extracellular vesicles in mammalian cells and its applications. *Nat. Rev. Mol. Cell Biol.*, 1–22 (2020).

G. Van Niel, G. D'Angelo, G. Raposo, Shedding light on the cell biology of extracellular vesicles. *Nat. Rev. Mol. Cell Biol.* **19**, 213–228 (2018).

E. Cocucci, G. Racchetti, J. Meldolesi, Shedding microvesicles: artefacts no more. *Trends Cell Biol.* **19**, 43–51 (2009).

C. Tricarico, J. Clancy, C. D'Souza-Schorey, Biology and biogenesis of shed microvesicles. *Small GTPases* **8**, 220–232 (2017).

C. Harding, J. Heuser, P. Stahl, Receptor-mediated endocytosis of transferrin and recycling of the transferrin receptor in rat reticulocytes. *J. Cell Biol.* **97**, 329–339 (1983).

T. A. P. Driedonks, E. N. M. Nolte-T'Hoen, Circulating Y-RNAs in extracellular vesicles and ribonucleoprotein complexes; Implications for the immune system. *Front. Immunol.* **10**, 3164 (2019).

M. J. Shurtleff, *et al.*, Broad role for YBX1 in defining the small noncoding RNA composition of exosomes. *Proc. Natl. Acad. Sci. U. S. A.* **114**, E8987–E8995 (2017).

H. E. Upton, *et al.*, Low-bias ncRNA libraries using ordered two-template relay: Serial template jumping by a modified retroelement reverse transcriptase. *Proc. Natl. Acad. Sci. U. S. A.* **118**, 1–10 (2021).

S. W. Messenger, S. S. Woo, Z. Sun, T. F. J. Martin, A Ca2+-stimulated exosome release pathway in cancer cells is regulated by Munc13-4. *J. Cell Biol.* **217**, 2877–2890 (2018).

A. Savina, M. Furlán, M. Vidal, M. I. Colombo, Exosome release is regulated by a calcium-dependent mechanism in K562 cells. *J. Biol. Chem.* **278**, 20083–20090 (2003).

N. W. Andrews, M. Corrotte, Plasma membrane repair. *Curr. Biol.* **28**, R392–R397 (2018).

J. K. Jaiswal, N. W. Andrews, S. M. Simon, Membrane proximal lysosomes are the major vesicles responsible for calcium-dependent exocytosis in nonsecretory cells. *J. Cell Biol.* **159**, 625–635 (2002).

J. K. Jaiswal, S. Chakrabarti, N. W. Andrews, S. M. Simon, Synaptotagmin VII restricts fusion pore expansion during lysosomal exocytosis. *PLoS Biol.* **2** (2004).

T. Hikita, M. Miyata, R. Watanabe, C. Oneyama, Sensitive and rapid quantification of exosomes by fusing luciferase to exosome marker proteins. *Sci. Rep.* **8**, 1–14 (2018).

J. R. Walker, *et al.*, Highly Potent Cell-Permeable and Impermeable NanoLuc Luciferase Inhibitors. *ACS Chem. Biol.* **12**, 1028–1037 (2017).

D. K. Jeppesen, *et al.*, Reassessment of Exosome Composition. *Cell* **177**, 428-445.e18 (2019).

M. Corrotte, T. Castro-Gomes, A. B. Koushik, N. W. Andrews, *Approaches for plasma membrane wounding and assessment of lysosome-mediated repair responses* (Elsevier Ltd, 2015).

M. Corrotte, T. Castro-Gomes, Lysosomes and plasma membrane repair. *Curr. Top. Membr.* **84**, 1–16 (2019).

A. R. Demonbreun, E. M. McNally, Plasma Membrane Repair in Health and Disease. *Curr. Top. Membr.* **77**, 67–96 (2016).

J. M. Barnes, J. T. Nauseef, M. D. Henry, Resistance to Fluid Shear Stress Is a Conserved Biophysical Property of Malignant Cells. *PLoS One* **7** (2012).

S. Gil-Parrado, *et al.*, Ionomycin-activated calpain triggers apoptosis. A probable role for Bcl-2 family members. *J. Biol. Chem.* **277**, 27217–27226 (2002).

M. Mittelbrunn, M. Vicente-Manzanares, F. Sánchez-Madrid, Organizing polarized delivery of exosomes at synapses. *Traffic* **16**, 327–337 (2015).

J. E. Alouf, Streptococcal toxins (streptolysin O, streptolysin S, erythrogenic toxin). *Pharmacol. Ther.* **11**, 661–717 (1980).

J. L. Martys, T. Shevell, T. E. McGraw, Studies of transferrin recycling reconstituted in streptolysin O permeabilized chinese hamster ovary cells. *J. Biol. Chem.* **270**, 25976–25984 (1995).

G. Apodaca, M. H. Cardone, S. W. Whiteheart, B. R. DasGupta, K. E. Mostov, Reconstitution of transcytosis in SLO-permeabilized MDCK cells: Existence of an NSF-dependent fusion mechanism with the apical surface of MDCK cells. *EMBO J.* **15**, 1471–1481 (1996).

K. Funato, W. Beron, C. Z. Yang, A. Mukhopadhyay, P. D. Stahl, Reconstitution of phagosome-lysosome fusion in streptolysin O- permeabilized cells. *J. Biol. Chem.* **272**, 16147–16151 (1997).

A. R. Demonbreun, *et al.*, An actin-dependent annexin complex mediates plasma membrane repair in muscle. *J. Cell Biol.* **213**, 705–718 (2016).

Q. C. Yu, P. L. McNeil, Transient disruptions of aortic endothelial cell plasma membranes. *Am. J. Pathol.* **141**, 1349–1360 (1992).

P. L. McNeil, R. Khakee, Disruptions of muscle fiber plasma membranes: Role in exercise-induced damage. *Am. J. Pathol.* **140**, 1097–1109 (1992).

F. Bouvet, *et al.*, Defective membrane repair machinery impairs survival of invasive cancer cells. *Sci. Rep.* **10**, 1–16 (2020).

M. Whitham, *et al.*, Extracellular Vesicles Provide a Means for Tissue Crosstalk during Exercise Resource Extracellular Vesicles Provide a Means for Tissue Crosstalk during Exercise. *Cell Metab.* **27**, 237-251.e4 (2018).

J. Meldolesi, Exosomes and Ectosomes in Intercellular Communication. *Curr. Biol.* **28**, R435–R444 (2018).

M. D. Keller, *et al.*, Decoy exosomes provide protection against bacterial toxins. *Nature* **579**, 260–264 (2020).

A. Horn, J. K. Jaiswal, Cellular mechanisms and signals that coordinate plasma membrane repair. *Cell. Mol. Life Sci.* **75**, 3751–3770 (2018).

R. Chambers, Microdissection Studies. I. The Visible Structure of Cell Protoplasm and Death Changes. *Am. J. Physiol.* **43**, 1–12 (1917).

L. V. Heilbrunn, The Surface Precipitation Reaction of Living Cells. *Proc. Am. Philos. Soc.* **69**, 295–301 (1930).

L. V. Heilbrunn, The action of various salts on the first stage of the surface precipitation reaction in Arbacia egg protoplasm. *Protoplasma* **11**, 558–573 (1930).

S. T. Cooper, P. L. McNeil, Membrane Repair: Mechanisms and Pathophysiology. *Physiol. Rev.* **95**, 1205–1240 (2015).

W. H. Humphries, C. J. Szymanski, C. K. Payne, Endo-lysosomal vesicles positive for rab7 and lamp1 are terminal vesicles for the transport of dextran. *PLoS One* **6** (2011).

R. A. Steinhardt, G. Bi, J. M. Alderton, Cell membrane resealing by a vesicular mechanism similar to neurotransmitter release. *Science (80-.).* **263**, 390–393 (1994).

D. Keefe, *et al.*, Perforin triggers a plasma membrane-repair response that facilitates CTL induction of apoptosis. *Immunity* **23**, 249–262 (2005).

A. L. Ingold, S. A. Cohn, J. M. Scholey, Inhibition of kinesin-driven microtubule motility by monoclonal antibodies to kinesin heavy chains. *J. Cell Biol.* **107**, 2657–2667 (1988).

B. Poulain, *et al.*, Neurotransmitter release is blocked intracellularly by botulinum neurotoxin, and this requires uptake of both toxin polypeptides by a process mediated by the larger chain. *Proc. Natl. Acad. Sci. U. S. A.* **85**, 4090–4094 (1988).

G. Schiavo, *et al.*, Tetanus and botulinum-B neurotoxins block neurotransmitter release by proteolytic cleavage of synaptobrevin. *Nature* **359**, 832–835 (1992).

S. N. Koerdt, A. P. K. Ashraf, V. Gerke, *Annexins and plasma membrane repair*, 1st Ed. (Elsevier Inc., 2019).

C. Croissant, R. Carmeille, C. Brévart, A. Bouter, Annexins and Membrane Repair Dysfunctions in Muscular Dystrophies. *Int. J. Mol. Sci.* **22** (2021).

T. L. Boye, J. Nylandsted, Annexins in plasma membrane repair. *Biol. Chem.* **397**, 961–969 (2016).

A. Bouter, *et al.*, Review: Annexin-A5 and cell membrane repair. *Placenta* **36 Suppl 1**, S43–S49 (2015).

A. D. Blazek, B. J. Paleo, N. Weisleder, Plasma Membrane Repair: A Central Process for Maintaining Cellular Homeostasis. *Physiology (Bethesda).* **30**, 438–448 (2015).

V. Gerke, S. E. Moss, Annexins: from structure to function. *Physiol. Rev.* **82**, 331–371 (2002).

C. Croissant, C. Gounou, F. Bouvet, S. Tan, A. Bouter, Annexin-A6 in Membrane Repair of Human Skeletal Muscle Cell: A Role in the Cap Subdomain. *Cells* **9** (2020).

K. A. Swaggart, *et al.*, Annexin A6 modifies muscular dystrophy by mediating sarcolemmal repair. *Proc. Natl. Acad. Sci. U. S. A.* **111**, 6004–6009 (2014).

N. Buzhynskyy, *et al.*, Annexin-A6 presents two modes of association with phospholipid membranes. A combined QCM-D, AFM and cryo-TEM study. *J. Struct. Biol.* **168**, 107–116 (2009).

T. Gerelsaikhan, P. K. Vasa, A. Chander, Annexin A7 and SNAP23 interactions in alveolar type II cells and in vitro: A role for Ca2+ and PKC. *Biochim. Biophys. Acta - Mol. Cell Res.* **1823**, 1796–1806 (2012).

M. Gabel, *et al.*, Annexin A2-dependent actin bundling promotes secretory granule docking to the plasma membrane and exocytosis. *J. Cell Biol.* **210**, 785–800 (2015).

X. Tang, F. Yang, Y. Guo, Cell-free Reconstitution of the Packaging of Cargo Proteins into Vesicles at the trans Golgi Network. *BIO-PROTOCOL* **10** (2020).

Chapter 2

Babiychuk, E.B., Monastyrskaya, K., Potez, S., Draeger, A., 2009. Intracellular Ca(2+) operates a switch between repair and lysis of streptolysin O-perforated cells. Cell Death Differ. 16, 1126–1134. https://doi.org/10.1038/cdd.2009.30

Bharadwaj, A., Bydoun, M., Holloway, R., Waisman, D., 2013. Annexin A2 heterotetramer: structure and function. Int. J. Mol. Sci. 14, 6259–6305. https://doi.org/10.3390/ijms14036259

Bharadwaj, A., Kempster, E., Waisman, D.M., 2021. The Annexin A2/S100A10 Complex: The Mutualistic Symbiosis of Two Distinct Proteins. Biomolecules 11, 1849. https://doi.org/10.3390/biom11121849

Blume, K.E., Soeroes, S., Keppeler, H., Stevanovic, S., Kretschmer, D., Rautenberg, M., Wesselborg, S., Lauber, K., 2012. Cleavage of annexin A1 by ADAM10 during secondary necrosis generates a monocytic “find-me” signal. J. Immunol. Baltim. Md 1950 188, 135–145. https://doi.org/10.4049/jimmunol.1004073

Boye, T.L., Jeppesen, J.C., Maeda, K., Pezeshkian, W., Solovyeva, V., Nylandsted, J., Simonsen, A.C., 2018. Annexins induce curvature on free-edge membranes displaying distinct morphologies. Sci. Rep. 8, 10309. https://doi.org/10.1038/s41598-018-28481-z

Corrotte, M., Castro-Gomes, T., Koushik, A.B., Andrews, N.W., 2015. Approaches for plasma membrane wounding and assessment of lysosome-mediated repair responses. Methods Cell Biol. 126, 139–158. https://doi.org/10.1016/bs.mcb.2014.11.009

Croissant, C., Carmeille, R., Brévart, C., Bouter, A., 2021. Annexins and Membrane Repair Dysfunctions in Muscular Dystrophies. Int. J. Mol. Sci. 22, 5276. https://doi.org/10.3390/ijms22105276

Croissant, C., Gounou, C., Bouvet, F., Tan, S., Bouter, A., 2020. Annexin-A6 in Membrane Repair of Human Skeletal Muscle Cell: A Role in the Cap Subdomain. Cells 9, 1742. https://doi.org/10.3390/cells9071742

Defour, A., Medikayala, S., Van der Meulen, J.H., Hogarth, M.W., Holdreith, N., Malatras, A., Duddy, W., Boehler, J., Nagaraju, K., Jaiswal, J.K., 2017. Annexin A2 links poor myofiber repair with inflammation and adipogenic replacement of the injured muscle. Hum. Mol. Genet. 26, 1979–1991. https://doi.org/10.1093/hmg/ddx065

Demonbreun, A.R., Quattrocelli, M., Barefield, D.Y., Allen, M.V., Swanson, K.E., McNally, E.M., 2016. An actin-dependent annexin complex mediates plasma membrane repair in muscle. J. Cell Biol. 213, 705–718. https://doi.org/10.1083/jcb.201512022

Dourdin, N., Bhatt, A.K., Dutt, P., Greer, P.A., Arthur, J.S., Elce, J.S., Huttenlocher, A., 2001. Reduced cell migration and disruption of the actin cytoskeleton in calpain-deficient embryonic fibroblasts. J. Biol. Chem. 276, 48382–48388. https://doi.org/10.1074/jbc.M108893200

Drücker, P., Pejic, M., Galla, H.-J., Gerke, V., 2013. Lipid segregation and membrane budding induced by the peripheral membrane binding protein annexin A2. J. Biol. Chem. 288, 24764–24776. https://doi.org/10.1074/jbc.M113.474023

Foltz, S.J., Cui, Y.Y., Choo, H.J., Hartzell, H.C., 2021. ANO5 ensures trafficking of annexins in wounded myofibers. J. Cell Biol. 220, e202007059. https://doi.org/10.1083/jcb.202007059

Fox, J.E., Austin, C.D., Reynolds, C.C., Steffen, P.K., 1991. Evidence that agonist-induced activation of calpain causes the shedding of procoagulant-containing microvesicles from the membrane of aggregating platelets. J. Biol. Chem. 266, 13289–13295.

Golia, M.T., Gabrielli, M., Verderio, C., 2023. P2X7 Receptor and Extracellular Vesicle Release. Int. J. Mol. Sci. 24, 9805. https://doi.org/10.3390/ijms24129805

Gounou, C., Rouyer, L., Siegfried, G., Harté, E., Bouvet, F., d'Agata, L., Darbo, E., Lefeuvre, M., Derieppe, M.A., Bouton, L., Mélane, M., Chapeau, D., Martineau, J., Prouzet-Mauleon, V., Tan, S., Souleyreau, W., Saltel, F., Argoul, F., Khatib, A.M., Brisson, A.R., Iggo, R., Bouter,

A., 2023. Inhibition of the membrane repair protein annexin-A2 prevents tumor invasion and metastasis. Cell. Mol. Life Sci. CMLS 81, 7. https://doi.org/10.1007/s00018-023-05049-3

Hanna, R.A., Campbell, R.L., Davies, P.L., 2008. Calcium-bound structure of calpain and its mechanism of inhibition by calpastatin. Nature 456, 409–412. https://doi.org/10.1038/nature07451

Hu, N.-J., Bradshaw, J., Lauter, H., Buckingham, J., Solito, E., Hofmann, A., 2008. Membrane-induced folding and structure of membrane-bound annexin A1 N-terminal peptides: implications for annexin-induced membrane aggregation. Biophys. J. 94, 1773–1781. https://doi.org/10.1529/biophysj.107.119685

Jaiswal, J.K., Lauritzen, S.P., Scheffer, L., Sakaguchi, M., Bunkenborg, J., Simon, S.M., Kallunki, T., Jäättelä, M., Nylandsted, J., 2014. S100A11 is required for efficient plasma membrane repair and survival of invasive cancer cells. Nat. Commun. 5, 3795. https://doi.org/10.1038/ncomms4795

Jeppesen, D.K., Fenix, A.M., Franklin, J.L., Higginbotham, J.N., Zhang, Q., Zimmerman, L.J., Liebler, D.C., Ping, J., Liu, Q., Evans, R., Fissell, W.H., Patton, J.G., Rome, L.H., Burnette, D.T., Coffey, R.J., 2019. Reassessment of Exosome Composition. Cell 177, 428-445.e18. https://doi.org/10.1016/j.cell.2019.02.029

Jimenez, A.J., Maiuri, P., Lafaurie-Janvore, J., Divoux, S., Piel, M., Perez, F., 2014. ESCRT machinery is required for plasma membrane repair. Science 343, 1247136. https://doi.org/10.1126/science.1247136

Jin, H., Zhang, C., Zwahlen, M., von Feilitzen, K., Karlsson, M., Shi, M., Yuan, M., Song, X., Li, X., Yang, H., Turkez, H., Fagerberg, L., Uhlén, M., Mardinoglu, A., 2023. Systematic transcriptional analysis of human cell lines for gene expression landscape and tumor representation. Nat. Commun. 14, 5417. https://doi.org/10.1038/s41467-023-41132-w

Kalluri, R., LeBleu, V.S., 2020. The biology, function, and biomedical applications of exosomes. Science 367, eaau6977. https://doi.org/10.1126/science.aau6977

Kearney, K.J., Ariëns, R.A.S., Macrae, F.L., 2022. The Role of Fibrin(ogen) in Wound Healing and Infection Control. Semin. Thromb. Hemost. 48, 174–187. https://doi.org/10.1055/s-0041-1732467

Koerdt, S.N., Gerke, V., 2017. Annexin A2 is involved in Ca2+-dependent plasma membrane repair in primary human endothelial cells. Biochim. Biophys. Acta Mol. Cell Res. 1864, 1046–1053. https://doi.org/10.1016/j.bbamcr.2016.12.007

Leloup, L., Shao, H., Bae, Y.H., Deasy, B., Stolz, D., Roy, P., Wells, A., 2010. m-Calpain activation is regulated by its membrane localization and by its binding to phosphatidylinositol 4,5-bisphosphate. J. Biol. Chem. 285, 33549–33566. https://doi.org/10.1074/jbc.M110.123604

Lin, Y.-C., Chipot, C., Scheuring, S., 2020. Annexin-V stabilizes membrane defects by inducing lipid phase transition. Nat. Commun. 11, 230. https://doi.org/10.1038/s41467-019-14045-w

McNeil, P.L., Khakee, R., 1992. Disruptions of muscle fiber plasma membranes. Role in exercise-induced damage. Am. J. Pathol. 140, 1097–1109.

Mellgren, R.L., Miyake, K., Kramerova, I., Spencer, M.J., Bourg, N., Bartoli, M., Richard, I., Greer, P.A., McNeil, P.L., 2009. Calcium-dependent plasma membrane repair requires m- or mu-calpain, but not calpain-3, the proteasome, or caspases. Biochim. Biophys. Acta 1793, 1886–1893. https://doi.org/10.1016/j.bbamcr.2009.09.013

Mellgren, R.L., Zhang, W., Miyake, K., McNeil, P.L., 2007. Calpain is required for the rapid, calcium-dependent repair of wounded plasma membrane. J. Biol. Chem. 282, 2567–2575. https://doi.org/10.1074/jbc.M604560200

Muenchbach, M., Dell'Ambrogio, M., Gazzotti, P., 1998. Proteolysis of liver plectin by mu-calpain. Biochem. Biophys. Res. Commun. 249, 304–306. https://doi.org/10.1006/bbrc.1998.9138

Perretti, M., Dalli, J., 2023. Resolution Pharmacology: Focus on Pro-Resolving Annexin A1 and Lipid Mediators for Therapeutic Innovation in Inflammation. Annu. Rev. Pharmacol. Toxicol. 63, 449–469. https://doi.org/10.1146/annurev-pharmtox-051821-042743

Piper, A.-K., Sophocleous, R.A., Ross, S.E., Evesson, F.J., Saleh, O., Bournazos, A., Yasa, J., Reed, C., Woolger, N., Sluyter, R., Greer, P., Biro, M., Lemckert, F.A., Cooper, S.T., 2020. Loss of calpains-1 and -2 prevents repair of plasma membrane scrape injuries, but not small pores, and induces a severe muscular dystrophy. Am. J. Physiol. Cell Physiol. 318, C1226–C1237. https://doi.org/10.1152/ajpcell.00408.2019

Prislusky, M.I., Lam, J.G.T., Contreras, V.R., Ng, M., Chamberlain, M., Pathak-Sharma, S., Fields, M., Zhang, X., Amer, A.O., Seveau, S., 2024. The septin cytoskeleton is required for plasma membrane repair. EMBO Rep. https://doi.org/10.1038/s44319-024-00195-6

Raj, N., Greune, L., Kahms, M., Mildner, K., Franzkoch, R., Psathaki, O.E., Zobel, T., Zeuschner, D., Klingauf, J., Gerke, V., 2023. Early Endosomes Act as Local Exocytosis Hubs to Repair Endothelial Membrane Damage. Adv. Sci. Weinh. Baden-Wurtt. Ger. 10, e2300244. https://doi.org/10.1002/advs.202300244

Reber, S., Mechtersheimer, J., Nasif, S., Benitez, J.A., Colombo, M., Domanski, M., Jutzi, D., Hedlund, E., Ruepp, M.-D., 2018. CRISPR-Trap: a clean approach for the generation of gene knockouts and gene replacements in human cells. Mol. Biol. Cell 29, 75–83. https://doi.org/10.1091/mbc.E17-05-0288

Reddy, A., Caler, E.V., Andrews, N.W., 2001. Plasma membrane repair is mediated by Ca(2+)-regulated exocytosis of lysosomes. Cell 106, 157–169. https://doi.org/10.1016/s0092-8674(01)00421-4

Redpath, G.M.I., Woolger, N., Piper, A.K., Lemckert, F.A., Lek, A., Greer, P.A., North, K.N., Cooper, S.T., 2014. Calpain cleavage within dysferlin exon 40a releases a synaptotagmin-like module for membrane repair. Mol. Biol. Cell 25, 3037–3048. https://doi.org/10.1091/mbc.E14-04-0947

Réty, S., Sopkova, J., Renouard, M., Osterloh, D., Gerke, V., Tabaries, S., Russo-Marie, F., Lewit-Bentley, A., 1999. The crystal structure of a complex of p11 with the annexin II N-terminal peptide. Nat. Struct. Biol. 6, 89–95. https://doi.org/10.1038/4965

Rezvanpour, A., Santamaria-Kisiel, L., Shaw, G.S., 2011. The S100A10-annexin A2 complex provides a novel asymmetric platform for membrane repair. J. Biol. Chem. 286, 40174–40183. https://doi.org/10.1074/jbc.M111.244038

Ritter, A.T., Shtengel, G., Xu, C.S., Weigel, A., Hoffman, D.P., Freeman, M., Iyer, N., Alivodej, N., Ackerman, D., Voskoboinik, I., Trapani, J., Hess, H.F., Mellman, I., 2022. ESCRT-mediated membrane repair protects tumor-derived cells against T cell attack. Science 376, 377–382. https://doi.org/10.1126/science.abl3855

Romero, M., Keyel, M., Shi, G., Bhattacharjee, P., Roth, R., Heuser, J.E., Keyel, P.A., 2017. Intrinsic repair protects cells from pore-forming toxins by microvesicle shedding. Cell Death Differ. 24, 798–808. https://doi.org/10.1038/cdd.2017.11

Shapovalov, I., Harper, D., Greer, P.A., 2022. Calpain as a therapeutic target in cancer. Expert Opin. Ther. Targets 26, 217–231. https://doi.org/10.1080/14728222.2022.2047178

Shurtleff, M.J., Temoche-Diaz, M.M., Schekman, R., 2018. Extracellular Vesicles and Cancer: Caveat Lector. Annu. Rev. Cancer Biol. 2, 395–411. https://doi.org/10.1146/annurev-cancerbio-030617-050519

Sønder, S.L., Boye, T.L., Tölle, R., Dengjel, J., Maeda, K., Jäättelä, M., Simonsen, A.C., Jaiswal, J.K., Nylandsted, J., 2019. Annexin A7 is required for ESCRT III-mediated plasma membrane repair. Sci. Rep. 9, 6726. https://doi.org/10.1038/s41598-019-43143-4

Sorimachi, H., Mamitsuka, H., Ono, Y., 2012. Understanding the substrate specificity of conventional calpains. Biol. Chem. 393, 853–871. https://doi.org/10.1515/hsz-2012-0143

Stefani, C., Bruchez, A.M., Rosasco, M.G., Yoshida, A.E., Fasano, K.J., Levan, P.F., Lorant, A., Hubbard, N.W., Oberst, A., Stuart, L.M., Lacy-Hulbert, A., 2024. LITAF protects against pore-forming protein-induced cell death by promoting membrane repair. Sci. Immunol. 9, eabq6541. https://doi.org/10.1126/sciimmunol.abq6541

Swaggart, K.A., Demonbreun, A.R., Vo, A.H., Swanson, K.E., Kim, E.Y., Fahrenbach, J.P., Holley-Cuthrell, J., Eskin, A., Chen, Z., Squire, K., Heydemann, A., Palmer, A.A., Nelson, S.F., McNally, E.M., 2014. Annexin A6 modifies muscular dystrophy by mediating sarcolemmal repair. Proc. Natl. Acad. Sci. U. S. A. 111, 6004–6009. https://doi.org/10.1073/pnas.1324242111

Teng, K.W., Ren, P., Selvin, P.R., 2018. Delivery of Fluorescent Probes Using Streptolysin O for Fluorescence Microscopy of Living Cells. Curr. Protoc. Protein Sci. 93, e60. https://doi.org/10.1002/cpps.60

Triglia, R.P., Linscott, W.D., 1980. Titers of nine complement components, conglutinin and C3b-inactivator in adult and fetal bovine sera. Mol. Immunol. 17, 741–748. https://doi.org/10.1016/0161-5890(80)90144-3

Walev, I., Bhakdi, S.C., Hofmann, F., Djonder, N., Valeva, A., Aktories, K., Bhakdi, S., 2001. Delivery of proteins into living cells by reversible membrane permeabilization with streptolysin-O. Proc. Natl. Acad. Sci. U. S. A. 98, 3185–3190. https://doi.org/10.1073/pnas.051429498

Williams, J.K., Ngo, J.M., Lehman, I.M., Schekman, R., 2023. Annexin A6 mediates calcium-dependent exosome secretion during plasma membrane repair. eLife 12, e86556. https://doi.org/10.7554/eLife.86556

Williams, S.L., Milne, I.R., Bagley, C.J., Gamble, J.R., Vadas, M.A., Pitson, S.M., Khew-Goodall, Y., 2010. A proinflammatory role for proteolytically cleaved annexin A1 in neutrophil transendothelial migration. J. Immunol. Baltim. Md 1950 185, 3057–3063. https://doi.org/10.4049/jimmunol.1000119

Wu, N., Cernysiov, V., Davidson, D., Song, H., Tang, J., Luo, S., Lu, Y., Qian, J., Gyurova, I.E., Waggoner, S.N., Trinh, V.Q.-H., Cayrol, R., Sugiura, A., McBride, H.M., Daudelin, J.-F., Labrecque, N., Veillette, A., 2020. Critical Role of Lipid Scramblase TMEM16F in Phosphatidylserine Exposure and Repair of Plasma Membrane after Pore Formation. Cell Rep. 30, 1129-1140.e5. https://doi.org/10.1016/j.celrep.2019.12.066

Zhen, Y., Radulovic, M., Vietri, M., Stenmark, H., 2021. Sealing holes in cellular membranes. EMBO J. 40, e106922. https://doi.org/10.15252/embj.2020106922

Chapter 3

Bulthuis, E.P., Adjobo-Hermans, M.J.W., de Potter, B., Hoogstraten, S., Wezendonk, L.H.T., Tutakhel, O.A.Z., Wintjes, L.T., van den Heuvel, B., Willems, P.H.G.M., Kamsteeg, E.-J., Gozalbo, M.E.R., Sallevelt, S.C.E.H., Koudijs, S.M., Nicolai, J., de Bie, C.I., Hoogendijk, J.E., Koopman, W.J.H., Rodenburg, R.J., 2023. SMDT1 variants impair EMRE-mediated mitochondrial calcium uptake in patients with muscle involvement. Biochim. Biophys. Acta Mol. Basis Dis. 1869, 166808. https://doi.org/10.1016/j.bbadis.2023.166808

Horn, A., Van der Meulen, J.H., Defour, A., Hogarth, M., Sreetama, S.C., Reed, A., Scheffer, L., Chandel, N.S., Jaiswal, J.K., 2017. Mitochondrial redox signaling enables repair of injured skeletal muscle cells. Sci. Signal. 10, eaaj1978. https://doi.org/10.1126/scisignal.aaj1978

Liu, J., Zuo, Z., Sastalla, I., Liu, C., Jang, J.Y., Sekine, Y., Li, Y., Pirooznia, M., Leppla, S.H., Finkel, T., Liu, S., 2020. Sequential CRISPR-Based Screens Identify LITAF and CDIP1 as the Bacillus cereus Hemolysin BL Toxin Host Receptors. Cell Host Microbe 28, 402-410.e5. https://doi.org/10.1016/j.chom.2020.05.012

Virreira Winter, S., Zychlinsky, A., Bardoel, B.W., 2016. Genome-wide CRISPR screen reveals novel host factors required for Staphylococcus aureus α-hemolysin-mediated toxicity. Sci. Rep. 6, 24242. https://doi.org/10.1038/srep24242